HARVARD UNIVERSITY
Graduate School of Arts and Sciences

DISSERTATION ACCEPTANCE CERTIFICATE

The undersigned, appointed by the

Department of Physics

have examined a dissertation entitled

Scanning Tunneling Microscopy Study on Strongly Correlated Materials

presented by Yang He

candidate for the degree of Doctor of Philosophy and hereby certify that it is worthy of acceptance.

Signature ______________________________

Typed name: Professor Jennifer Hoffman, Chair

Signature ______________________________

Typed name: Professor Philip Kim

Signature ______________________________

Typed name: Professor Subir Sachdev

Date: June 8, 2015

Scanning Tunneling Microscopy Study on Strongly Correlated Materials

A DISSERTATION PRESENTED
BY
YANG HE
TO
THE DEPARTMENT OF PHYSICS

IN PARTIAL FULFILLMENT OF THE REQUIREMENTS
FOR THE DEGREE OF
DOCTOR OF PHILOSOPHY
IN THE SUBJECT OF
PHYSICS

HARVARD UNIVERSITY
CAMBRIDGE, MASSACHUSETTS
NOVEMBER 2015

Thesis advisor: Professor Jennifer E. Hoffman Yang He

Scanning Tunneling Microscopy Study on Strongly Correlated Materials

ABSTRACT

Strongly correlated electrons and spin-orbit interaction have been the two major research directions of condensed matter physics in recent years. The discovery of high temperature superconductors in 1986 not only brought excitement into the field but also challenged our theory on quantum materials. After almost three decades of extensive study, the underlying mechanism of high temperature superconductivity is still not fully understood, the reason for which is mainly a poor understanding of strongly correlated systems. The phase diagram of cuprate superconductors has become more complicated throughout the years as multiple novel electronic phases have been discovered, while few of them are fully understood. Topological insulators are a newly discovered family of materials bearing topological non-trivial quantum states as a result of spin-orbit coupling. The theoretically predicted topological Kondo insulators as strongly correlated systems with strong spin-orbital coupling make an ideal playground to test our theory of quantum materials.

Scanning tunneling microscopy (STM) is a powerful technique to explore new phenomena in materials with exotic electronic states due to its high spacial resolution and high sensitivity to low energy electronic structures. Moreover, as a surface-sensitive technique, STM is an ideal tool to investigate the electronic properties of topological and non-topological surface states. In this thesis, I will describe experiments we performed on high temperature superconductors and topological Kondo insulators using STM.

First, I will describe our experiments on a Bi-based high temperature superconductor $\mathrm{Bi_2Sr_2CuO_{6+\delta}}$. The quasiparticle interference technique uncovers a Fermi surface reconstruction. We also discov-

ered the coexistence of Bogoliubov quasiparticle and pseudogap state at the antinodes. Afterwards, I will discuss our discovery of d-form factor density wave in the same material, showing the omnipresence of d form factor density wave above and below the Fermi surface reconstruction. The relation between the d-form factor density wave and the pseudogap state is discussed.

Second, I will describe our experiments on topological Kondo insulator SmB_6 where spin-orbit coupling plays an important role in the strongly correlated electron system. I will present the spectroscopic evidence of Kondo hybridization based on a spectral decomposition technique. I will introduce a dimension reduction method in the fitting procedure to reduce the computation time by two order of magnitude. I will also discuss the possible quasiparticle interference patterns we discovered in SmB_6.

Contents

Listing of figures

Dedicated to my parents and Cindy Zhizhi Xin

Acknowledgments

It would not be possible for this thesis to be written without the help of many people.

I would like to express my sincere appreciation to my advisor Prof. Jennifer Hoffman for her guidance. Jenny has been supportive financially and academically of my research over the past five years. Through my graduate school, I had the chance to choose the directions of my research, and Jenny was always supportive of my proposals. I also learned from her that being detail-oriented and persistent can always make a difference.

I am grateful in particular to Prof. Eric Hudson; he shared with me not only his valuable data and research ideas on BSCCO, but also his passion for physics and scientific research. I am fortunate to have Prof. Subir Sachdev and Prof. Eugene Demler as my committee members. Their insight has shaped my understanding of the field. The valuable discussions with them have been a vital part of my graduate education. Thank you to Prof. Philip Kim, for valuable feedback on my thesis and insightful advice on future projects.

I would like to thank my teammates on STM1, both personally and professionally. To Anjan Soumyanarayanan and Michael Yee, for being my mentors in my junior years of graduate study, teaching me everything I needed to know to survive my graduate education. I will always miss the late nights we spent together in the lab. To Jason Zhihuai Zhu, for tremendous help on the experiment and for sharing his wisdom of life. To our new teammates Oliver Yau Chuen Yam, Pengcheng Chen and Mohammad Hamidian for a lot of help on our experiment. I wish them all the best in their future endeavors.

I am grateful to have had Ilija Zeljkovic as my desk-mate, who shared with me his experience in data analysis and was always supportive of my new ideas on cuprate research. I am fortunate to have had Can-li Song as my roommate in my early years as a graduate student. I benefited a great deal from our discussions on different fields of condensed matter research. Special thanks to Cun Ye, a lot of ideas in my thesis came up naturally in our discussions, which I still remember vividly. To Emanule Dalla Torr, for insightful discussion of cuprates. To Dennis Huang, for his assistance on my experiments, useful discussion and feedback on my research ideas, and most importantly, teaching me how to think positively. To Tatiana Webb, for proofreading my thesis in detail and for useful discussion on image processing. I would also like to thank Mike Boyer, Kamalesh Chatterjee and Doug Wise from the Hudson Lab for sharing their data.

I would also like to thank my friends outside of physics research. To Hao Pei, Jia Liu, Xiaochuan Dai and Teng Gao, for being excellent roommates and make me feel at home in Boston. To Jiannan Lu, for sharing his passion for and knowledge of statistics.

Last but not the least, I am always indebted to my parents for their support and unconditional love, and to my girlfriend Zhizhi Xin, who has spent countless weekends in our lab, for her patience and support through my graduate education.

Thank you all!

1

Introduction

In this chapter, we will give a brief introduction to the materials that we are going to cover in this thesis. We will start with a summary of the research on high transition temperature (T_c) superconductors focusing on the topics that have been heatedly discussed in recent years such as charge order and Fermi surface reconstruction. Afterwards, we will give an introduction to topological insulators with emphasis on topological Kondo insulator, the new member of the topological insulator family in which strong electron correlations and the spin oribit interaction are highly interwined.

1.1 CUPRATE SUPERCONDUCTORS

Ever since the discovery of high T_c superconductiviy (HTSC) in cuprate $\mathrm{La_{2-x}Ba_xCuO_4}$[16] three decades ago, the research on HTSC has been one of the hottest topic in the field of condensed matter physics. Over the years, much has been learned about the HTSC and a qualitative consensus has been reached on the superconducting state itself. However, there are many other novel electronic states that have been discovered adjacent to the superconducting region of the cuprate phase diagram, such as the intriguing and mysterious pseudogap state, symmetry breaking charge order and charge density wave states, and the strange metal state lacking quasiparticles. While the nature and the origin of most of these exotic state remain unknown at this point, experiments suggest that they are highly interwined with HTSC. Research on these exotic states serves to (1) test our quantum theory of the electronic properties of solids by understanding the mechanism behind these exotic state; (2) understanding of the pairing mechanism can lead us to a predictive model which will guide us to engineer superconductors with higher critical temperature and critical current.

The Bardeen-Cooper-Schrieffer (BSC) theory[14] laid the foundation of theory physicists use to understand the mechanism underlying superconductors. The BCS ground state consists of Cooper pairs, where fermions such as electrons are bound into pairs and thus can condense in a way similar to bosons at low temperature. The quantized excitation in the BCS system is called a Bogoliubov quasiparticle, which can be measured by STM via density of states mapping. An attractive interaction is needed to bind the electrons in a superconductor into Cooper pairs. In conventional superconductors, electron-phonon coupling is widely believed to be the binding force of Cooper pairs. The critical temperature T_c based on the electron-phonon coupling mechanism is believed to be lower than 30K[63].

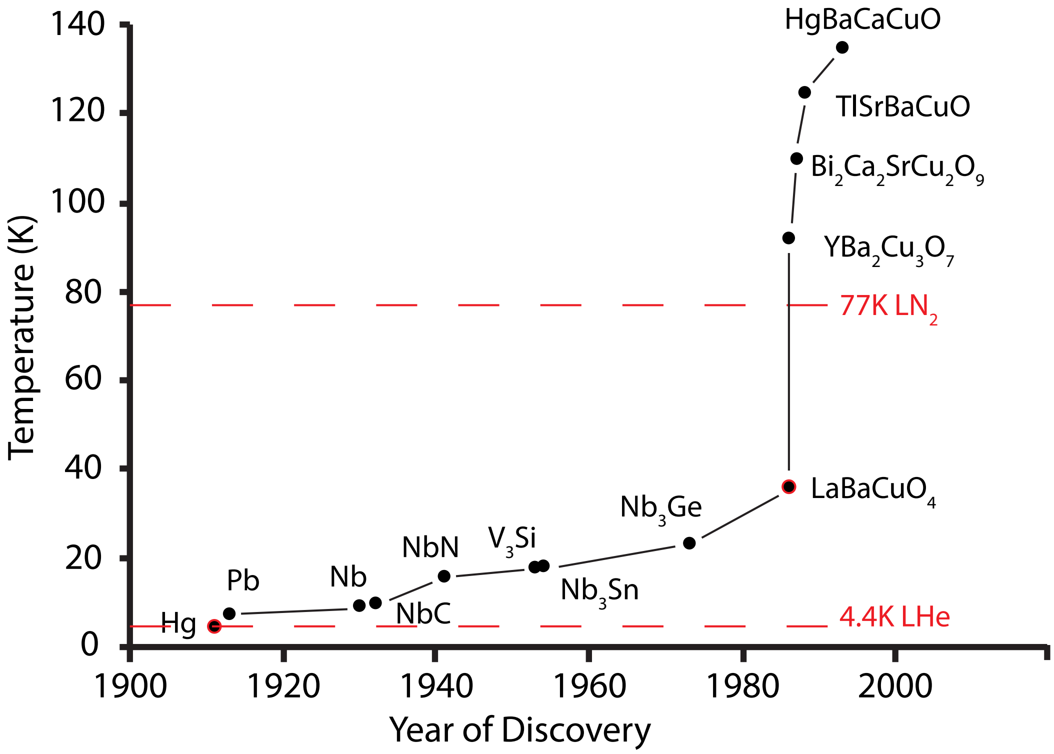

Figure 1.1: Superconducting transition temperatures versus year of discovery for both conventional and cuprate superconductors. Liquid helium and liquid nitrogen temperatures are highlighted with red dashed lines.

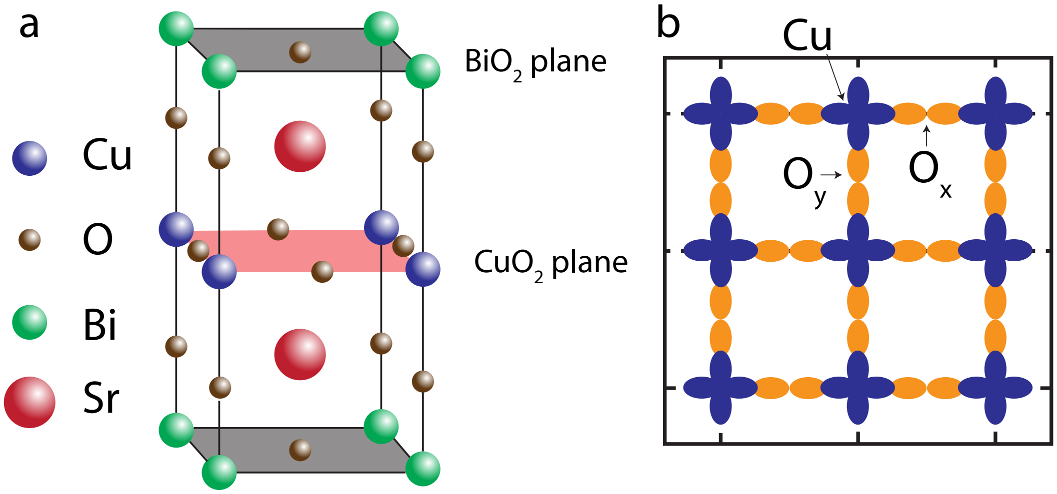

Figure 1.2: **a** A unit cell of Bi2201 with copper oxide and bismuth oxide planes highlighted. The bismuth oxide plane is the natural cleavage plane of the material. **b** Top view of the copper oxide plane. The electronic structure of these planes invovles hybridization of copper $3d_{x^2-y^2}$ and oxygen $2p$ orbitals shown in blue and orange respectively.

As shown in the figure above, the transition temperatures of copper oxide or cuprate superconductors can be much higher than 30K. Even though the conventional BSC theory fails to explain a lot of novel electronic properties of cuprate superconductors such as the high transition temperatures, the mysterious pseudogap state and the strange metal phase, there is still wide consensus that the superconductivity arises from Cooper pair condensation. The pairing and the condensation mechanism in cuprate superconductor might be different from its conventional cousins.

1.1.1 CRYSTAL STRUCTURE

The crystal structure of a typical Bi-based cuprate superconductor $Bi_2Sr_2CuO_{6+\delta}$ (Bi2201) is shown in Figure 1.2. The experiments described in Charpter 3-4 have been performed on Bi2201 with different doping levels and under different conditions.

The family of Bi-based cuprate (BSCCO) was discovered in 1988[79]. There are three different compounds in this family, namely Bi2201, $Bi_2Sr_2CaCu_2O_{8+\delta}$ (Bi2212) and $Bi_2Sr_2Ca_2Cu_3O_{10+\delta}$ (Bi2223) with optimal T_c being 35K, 95K and 108K respectively. BSCCO are hole-doped cuprate superconductors with optimum doping $p \sim 0.16$. Bi2212 is the most commonly studied compound in this family. Bi2201 has only one CuO_2 plane in a unit cell, while Bi2212 and Bi2223 have two and three repectively. Despite its comparativley low T_c, the simple crystal stucture of Bi2201 might help to simplify the electronic structure in the compound thus offer a clearer picture of high T_c superconductivity.

The adjacent BiO_2 layers are weakly bonded by van der Waals force. As a result, BSCCO typically cleave on a charge neutral plane between two BiO_2 layers, highlighted in Figure 1.2. Such charge neutral planes are favorable to surface sensitive measurement such as STM and angle resloved photoemission spectroscopy (ARPES).

1.1.2 PHASE DIAGRAM

Cuprate superconductors contain planes of copper oxide, where the high T_c superconductivity takes place. The crystal structure of the copper oxide plane amplifies the Coulomb repulsions between electrons. The two dimensional copper oxide planes (Figure 1.2ḃ) are seperated by electronically inert buffer layers. Without doping, a single electron occupies each site on the copper oxide plane, forming a Mott insulator. Superconductivity is achieved by doping the Mott insulator with electrons or holes, as illustrated in Figure 1.3. The doping level below and above the optimum doping are called underdoped and overdoped.

The electronic properties of underdoped and overdoped cuprates are different. The origin of of the difference is one of central issues in the study of high temperature cuprate superconductors. In the overdoped regime, electrons are described by Fermi liquid theory similar to conventional metals. A full Fermi surface is observed in overdoped cuprates as illustrated in Figure 1.3c. In the

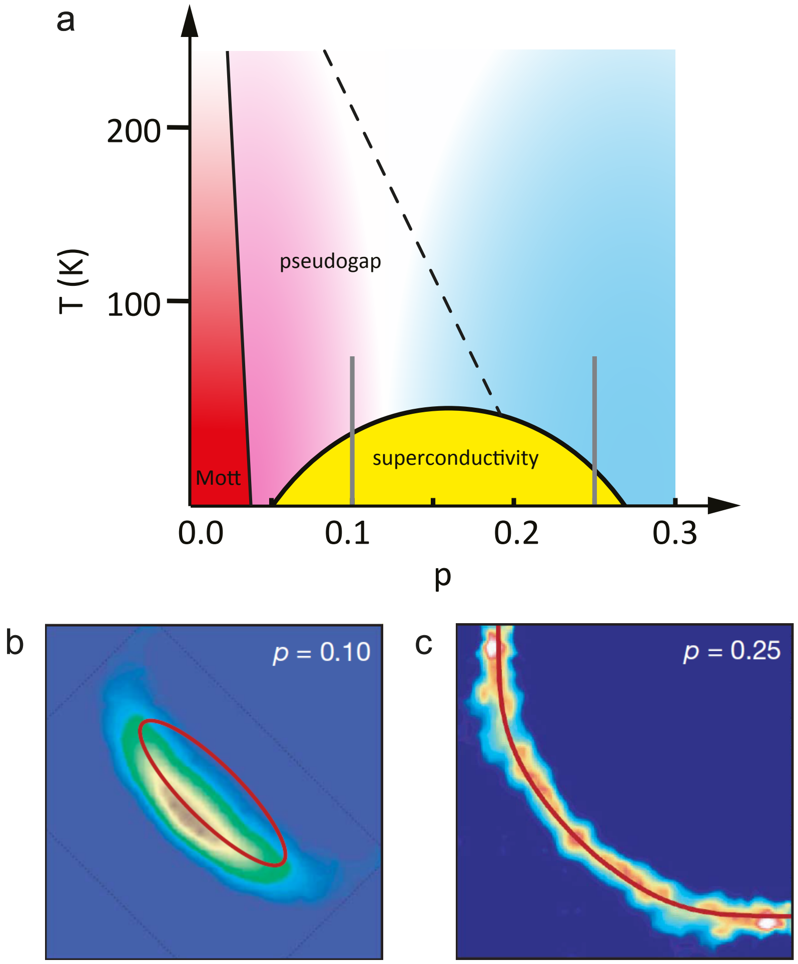

Figure 1.3: **a** Schematic doping dependence of hole doped cuprate superconductors. Mott insulator around zero doping is highlighted in red. When doped with holes, the compound enters the dome shape superconducting region. Pseudogap crossover temperature is illustrated as a dashed line. Two typical dopings $p = 0.1$ and $p = 0.25$ are marked with vertical grey lines. **b** Fermi surface measured by photoemission in underdoped cuprate Na-CCOC at $p = 0.1$[112]. The truncated Fermi surface is usually referred to as "Fermi arc". **c** Fermi surface measured by photoemission in overdoped cuprate Tl-2201 at $p = 0.25$[101]. A full Fermi surface is observed.

underdoped region, however, the Fermi surface is truncated. Only disconnected "Fermi arcs" are observed. Prior to this work, the doping of the small to large Fermi surface reconstruction had never been observed within the same compound. The other fundamental question is what is the relation between this Fermi surface reconstruction and superconductivity. Our understanding of high transition temperature superconductivity and even other strongly correlated systems will depend on our understanding of the Fermi surface reconstruction.

1.2 Topological insulators

The concept of topology and topological transition have been introduced to condensed matter physics long time ago. The concept has become popular after the discovery of a new class of "topological materials" especially 3D topological insulators in 2009[58]. A topological insulator is a material that has band inversion due to the spin-orbit interaction. The spin-orbit interaction stems from the physics of relativity where electric and magnetic field are interchangable depending on the movement of the object. To have a strong spin-orbit interaction, heavy elements such as Bi or Sb are required in the materials. The typical 3D topological insulators are Bi_2Se_3, Bi_2Te_3 and $Bi_{1-x}Sb_x$ alloy[51]. The electronic states at the surface of these materials have different properties compared to normal surface states, such as spin momentum locking illustrated in Figure 1.4. With spin naturally separated in both momentum and real space, topological insulators open the door of developing novel spintronic devices without involving magnetic field or magnetic materials.

1.2.1 TOPOLOGICAL SURFACE STATE

Topological insulators are materials with bulk insulating gap and a pair of topological surface states protected by time reversal symmetry. The origin of the topological surface state stems from band inversion in the material caused by spin orbit interaction.

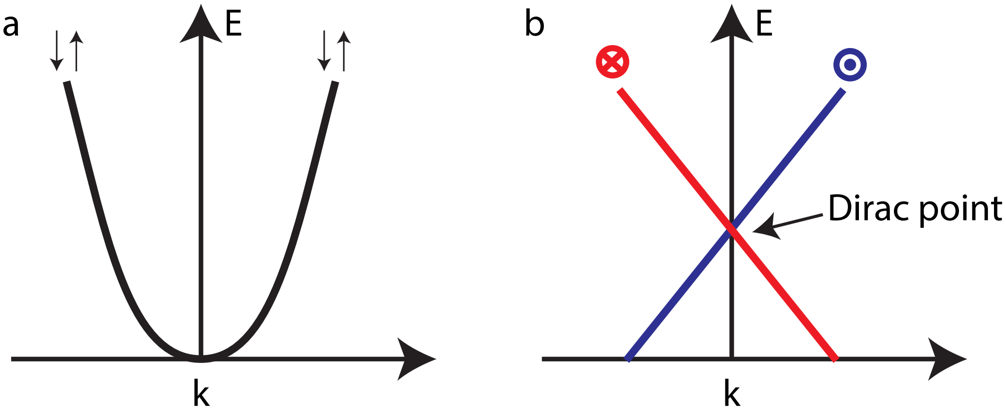

Figure 1.4: **a** Dispersion relation of a normal surface state. The dispersion relation is parabolic with both spin up and spin down in the same band. **b** Band structure of a topological surface state. The dispersion relation is linear with only one spin orientation in each band.

In conventional band theory of solid, an insulator has an energy gap that separates the occupied valence band states from the empty conduction band states. In other words, the chemical potential or the Fermi level lies within the insulating gap of the material. This type of insulator is equivalent to the vacuum where an energy gap separates the occupied valence band (positrons) and the excitation band(electrons) based on Dirac's theory. A quantum Hall insulator in two dimension, however, is different from the conventional insulator. When electrons are confined in a two dimensional plane with strong magnetic field, the ground state of these electrons becomes a series of quantized circular orbits called Landau levels. In this system, Landau levels are viewed as a band structure of a quantum Hall insulator.

The difference between a quantum Hall insulator and a conventional band insulator can be explained by the TKNN invariant[119] or Chern number in terms of topology. Once the Bloch wave function of a system is acquired, one can calculate the Berry phase at each point of the k-space. The Berry phase can be expressed as a surface integral of the Berry flux similar to magnetic flux and magnetic vector potential. The Chern number is the total Berry flux in the occupied bands. In mathe-

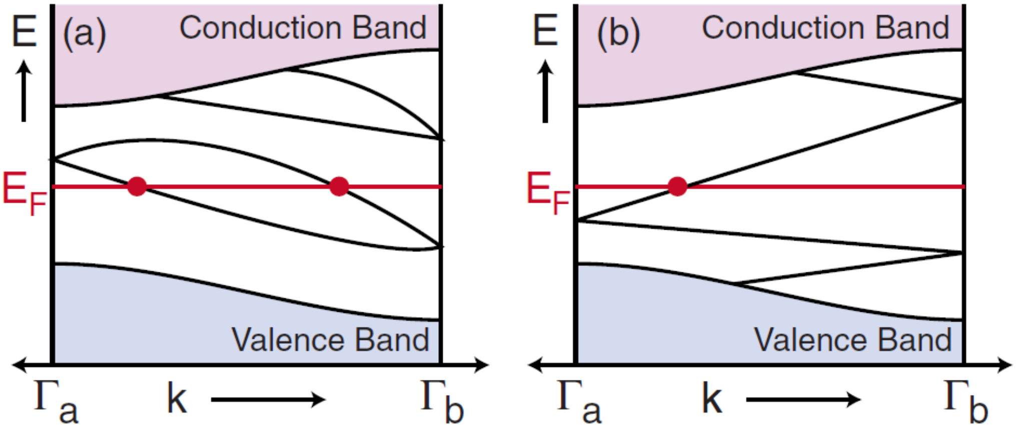

Figure 1.5: Two classes of insulators. Electronic dispersion between two boundary Kramers degenerate points Γ_a and Γ_b. Γ_a and Γ_b are high symmetry points thus guarantee the double degeneracy. In (a) the number of surface states crossing the Fermi energy E_F is even, whereas in (b) it is odd. This figure is adapted from Hasan *et al.*[51].

matics, the integral of the Gaussian curvature over a closed surface is a quantized invariant. This is known as the Gauss Bonnet theorem. The Chern number is an integral that characterizes the topology of the quantum states of a material.

In a quantum Hall insulator, the existence of gapless conducting states at the interfaces between the bulk and the outside vacuum is a fundamental consequence of the topological classification by Chern number. Such gapless conducting states are usually referred to as edge states in a 2D quantum Hall insulator. The electrons in the edge state propagate in a single direction along the edge and are insensitive to disorder because no states are available for backscattering. The existence of the edge state is a result of different topology between the quantum Hall insulator and the vacuum (normal insulator). This phenomenon is called bulk-surface correspondence.

A high magnetic field is needed to realize a quantum Hall insulator. How to create a topological non-trivial state in a material without applied magnetic field was a challenging problem. Kane and Mele pointed out that the spin-orbit interaction allows a different topological class of insulating

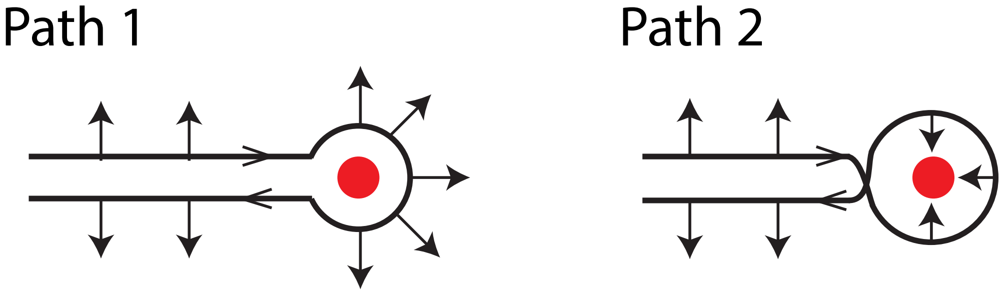

Figure 1.6: Two possible paths of scattering of topological surface state There are two paths an electron can take when encounter an impurity, namely clockwise (path 1) and counter-clockwise (path 2). A geometrical phase factor associated with two different paths leads to destructive interference. As a result, backscattering is suppressed in the topological surface state.

band structures even when time reversal symmetry is unbroken in their 2005 paper[62]. Though the TKNN invariant is $n = 0$ when time reversal symmetry is preserved, there is an additional invariant with two possible values, $\nu = 0$ or $\nu = 1$. This proposal led to the discovery of Z_2 topological insulator. These two classes of insulators can be understood by the bulk-boundary correspondence highlighted in Figure 1.5. The insulators with $\nu = 1$ are called topological insulators.

Similar to the edge states in a quantum Hall insulator, topologically protected surface states exist on the boundary between topological insulators and vacuum. The surface states are helical with spin locked by momentum and propagate in both directions. This is different from quantum Hall effect and quantum Hall insulator. Time reversal symmetry prevents the helical edge states from backscattering. A semiclassical argument is highlighted in Figure 1.6

1.2.2 TOPOLOGICAL KONDO INSULATORS

Kondo insulators are heavy fermion materials with hybridization gaps spanning the Fermi level. The first Kondo insulator was discovered over forty years ago[84]. While these materials are strongly correlated in nature, their band structure and ground states are similar to conventional non-interacting band insulators. As a result, Kondo insulators can also be topologically classified. Moreover, Kondo insulators usually have strong spin orbit interaction, which is necessary for topological insulators. The spin-orbit coupling associated with the hybridization between conduction and f-electrons can produce topological non-trivial states.

In a Kondo insulator, the insulating gap arises from the hybridization between the conduction and f electrons. This type of insulating gap is typically several meV in size. Once the chemical potential of the material lies inside the hybridization gap, the material becomes a Kondo insulator. The process of hybridization can be described by an Anderson lattice model and is illustrated in Figure 1.7. At high temperature, thermal excitations dominate the heavy fermion system. The interaction between the conduction and f electrons is negligible. When the system is cooled down below a characteristic temperature noted as Kondo temperature (T_K), the conduction electrons are localized by the periodic array of magnetic moments similar to the single impurity Kondo effect. The localization of conduction electrons results in a hybridization gap in a Kondo insulator as shown in Figure 1.7.

In the Kondo insulating phase, one can calculate the Z_2 invariants from the parity of the occupied bands. Some materials are predicted to be topological Kondo insulators based on the Z_2 classification similar to topological insulators. The predicted topological Kondo insulator most studied is SmB_6, which will be discussed in more detail in Chapter 5.

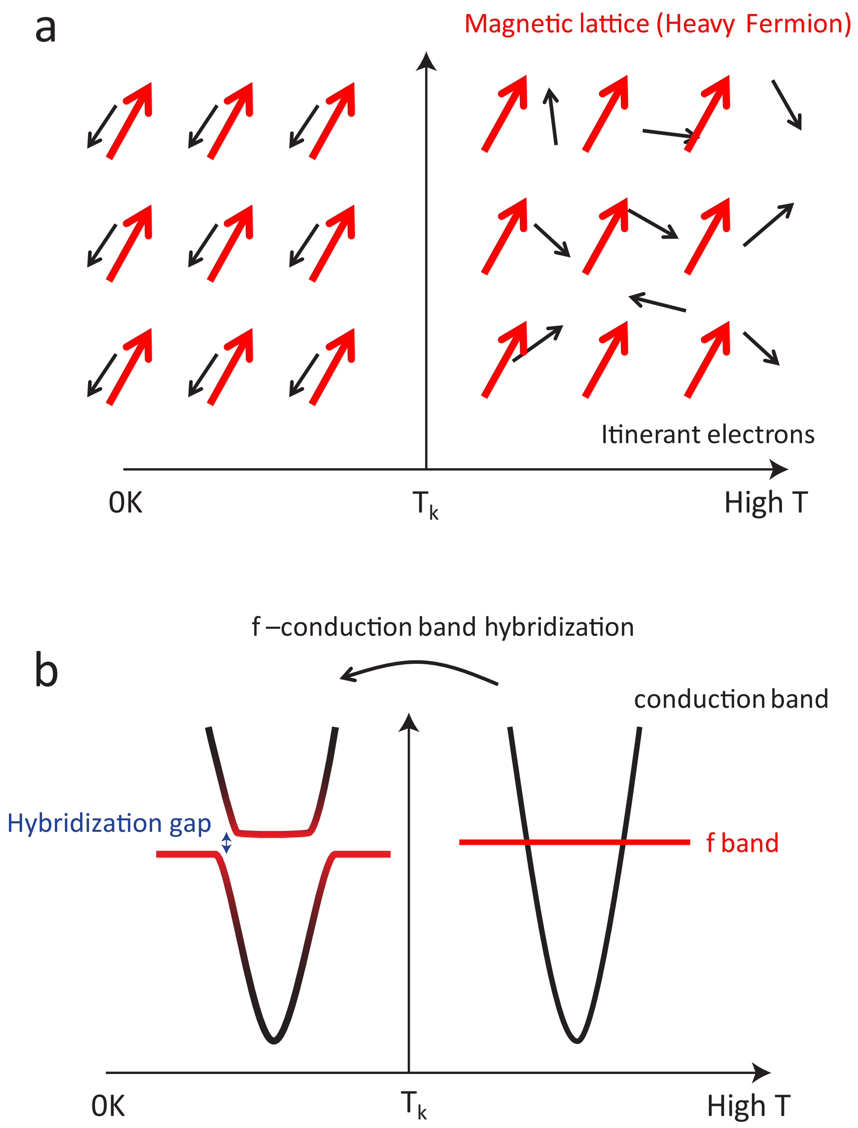

Figure 1.7: Hybridization in a Kondo insulator. **a** Schematic representation of the Kondo screening effect in a Kondo lattice. Magnetic atoms are shown in red and conduction electrons are shown in black. At temperature lower than T_K, conduction electrons screen the magnetic local moments resulting in Kondo localization. **b** Schematic plot of Kondo hybridization in k space. The conduction band is shown in black while the f-band is in red. At high temperature, when there is no interaction, the two band cross each other without opening a gap. At temperature lower than T_K, a Kondo hybridization gap opens when hybridization turns on. The conduction electrons become localized.

2

Scanning Tunneling Microscopy

IN THIS CHAPTER we will focus on the basic principle of scanning tunneling microscopy (STM). Tunneling measurements provide remarkable insight in the electronic properties of materials. Differential conductance gives a good approximation to the density of states (DOS) in sample materials. By adding spatial degrees of freedom to the conventional tunneling experiment, STM provides direct DOS information with sub-Angstrom resolution on a material. Here we will start by introducing the working principle of a tunneling experiment. We will follow up with different operating modes of STM in the final section. We will also describe the momentum resolved quasi-particle interference (QPI) technique.

2.1 WORKING PRINCIPLE OF STM

Electron tunneling descibes the phenomenon in which an electron can tunnel between two electrodes that are separated by a potential barriers. In conventional tunneling experiments, a thin insulating layer is used to form the potential barrier[44]. In the case of STM, the insulating layer is given by the vacuum spacing between a tip and a sample. The distance between an STM tip and a sample is estimated to be on the order of several angstroms, the actual value of which is difficult to measure directly by an STM. The high spatial resolution of an STM is provided by an exponential dependence of the tunneling current on the distance between tip and sample, which will be explained in more detail in the next paragraph using WKB approximation.

In vacuum tunneling, the potential in the vacuum region acts as a barrier to electrons between the two metal electrodes. The transmission probability for a wave incident on a barrier in one dimension can be easily calculated. The solutions of Schrodinger's equation inside a barrier in one dimension have the form

$$\phi = e^{\pm \kappa z} \tag{2.1}$$

$$\kappa^2 = 2m(V_B - E)/\hbar^2 \tag{2.2}$$

Here E is the energy of the state and V_B is the barrier potential. Thus, $V_B - E$ is the work function. The transmission probability, or the tunneling current can be fomulated as

$$I \propto e^{-2\kappa d} \tag{2.3}$$

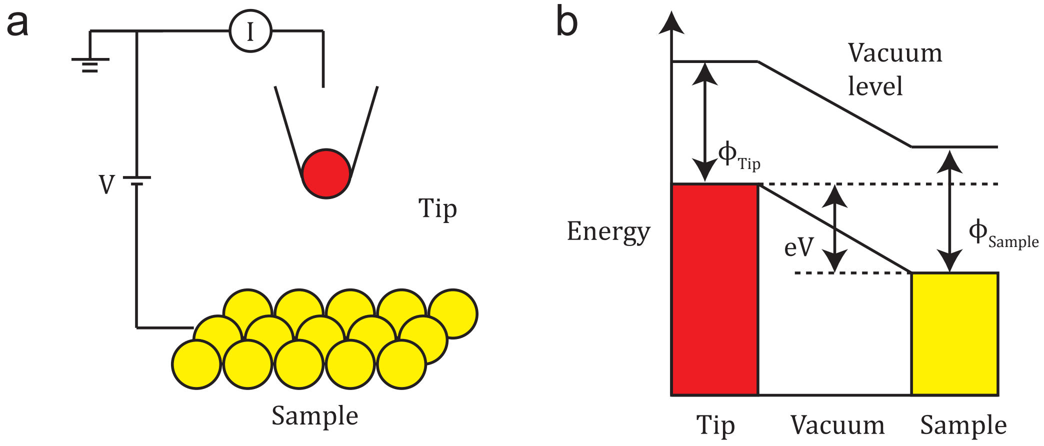

Figure 2.1: a Schematic of a tunneling experiment between an STM tip and a sample. A DC voltage V is applied between the tip and the sample while tunneling current is measured. **b** Illustration of tunneling process between the tip and the sample. A bias V is applied between the tip and the sample. Electrons are tunneling between the sample and the tip while current is flowing in the opposite direction. Φ_{Sample} and Φ_{Tip} represent the work function of the sample and the tip respectively.

Typical material work function is around 4-5 eV. So κ is typically around 2Å^{-1}. κ can be measured by an STM.

In the tunneling Hamiltonian approach, the tunneling current can be calculated using the first-order perturbation theory. Based on Fermi's golden rule, the current or transmission rate is

$$I = \frac{2\pi e}{\hbar} \sum_{\mu,\nu} [f(E_\mu)[1 - f(E_\nu)] - f(E_\nu)[1 - f(E_\mu)]] |M_{\mu\nu}|^2 \delta(E_\nu + V - E_\mu) \tag{2.4}$$

where $f(E)$ is the Fermi function , V is the applied voltage, $M_{\mu,\nu}$ is the tunneling matrix element between states ϕ_μ and ϕ_ν on each side of the tunneling barrier. E_ν is the energy of state ϕ_ν. We are going to simplify the calculation by assuming zero temperature. In this scenario, the Fermi function is simply a step funtion. The tunneling current can be written as

$$I = \frac{2\pi}{\hbar} e^2 V \sum_{\mu,\nu} |M_{\mu,\nu}|^2 \delta(E_\nu - E_F) \tag{2.5}$$

Under the assumptions that $M_{\mu,\nu}$ and density of states of the tip are energy independent, one can simplify the tunneling current at small voltage into

$$I \propto \sum_{\nu} |\phi_\nu(\mathbf{r}_t)|^2 \, \delta(E_\nu - E_F) = \rho((\mathbf{r}), E_F) \tag{2.6}$$

At larger voltages, one can easily generalize the previous equation into a simple expression

$$I \sim \int_{E_F}^{E_F+V} \rho(\mathbf{r}, E) dE \tag{2.7}$$

However, this equation is not strictly correct for three reasons. First, we made the assumption that the matrix element and the tip density of states are energy independent. Second, the finite voltage changes the potential and hence the wave functions outside the surface. Third, the tip-sample interaction is not included in the model. These factors are important when measuring exotic states on the sample surface, such as image potential states.

2.2 OPERATION MODES OF AN STM

There are three major operation modes using an STM, namely topography, dI/dV spectrum and dI/dV mapping. In this section, we will describe the application of each mode with some experimental detail included. The advantages and disadvantages of each mode are also discussed.

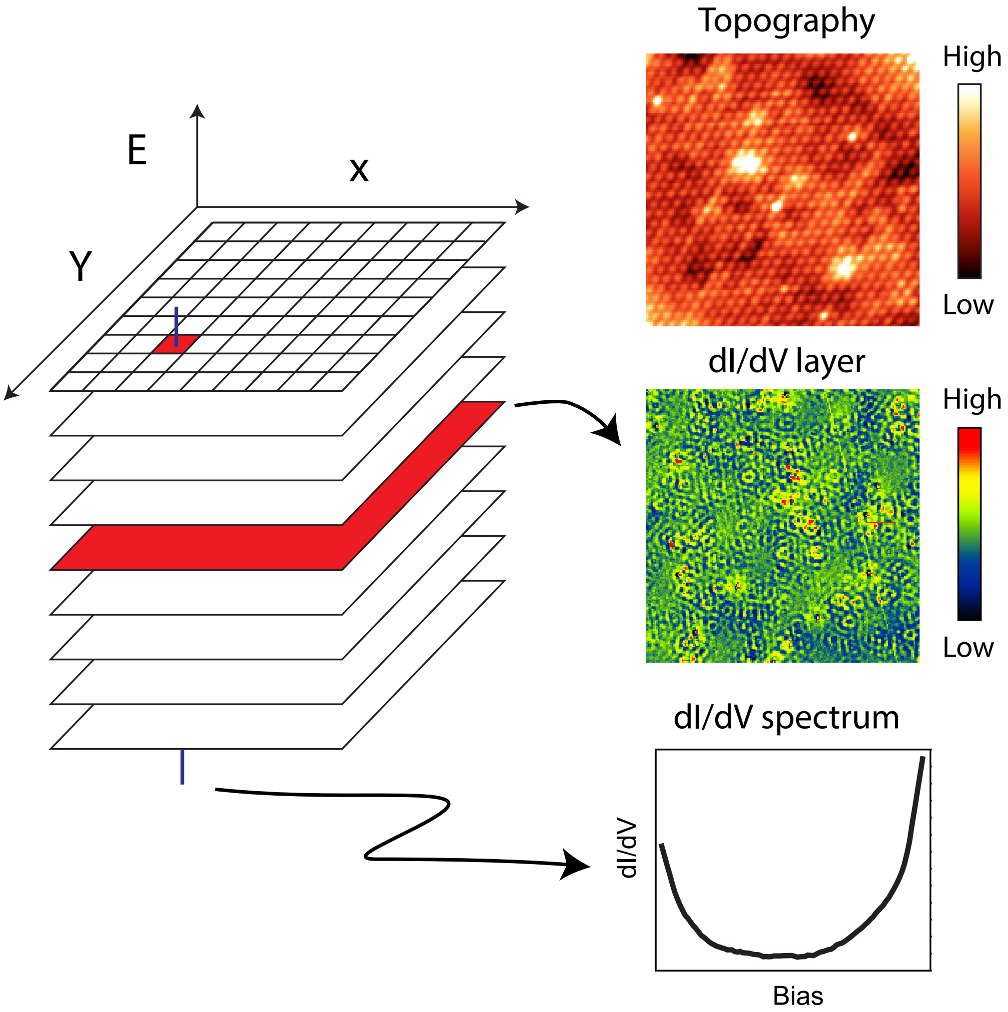

Figure 2.2: Different operation modes of an STM a Schematic of three dimensional data sets obtained on a grid. Each layers represents a DOS mapping at a single energy. The blue line denotes a single dI/dV spectrum. **b** Topography with atomic resolution taken on the Te termination of BiTeI sample. **c** An example of dI/dV layer at 1.4V of Te termination of BiTeI. **d** Single spectrum obtained on the Te termination of BiTeI sample.

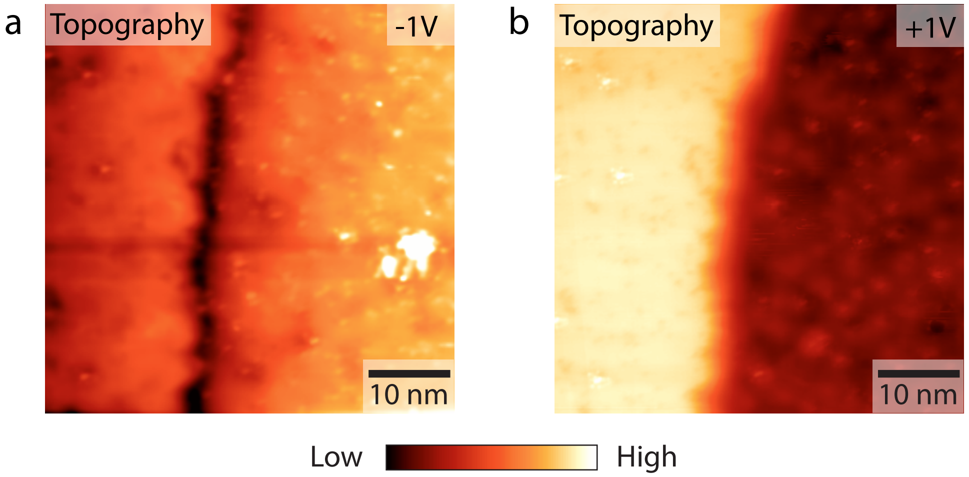

Figure 2.3: Topography on BiTeI with different setup conditions a Topograph taken on BiTeI at the boundary of Te and I terminated surface at -1V. **b** Topograph taken in the same field of view as **a** using +1V. One can see that the "height" on each side of the surface depends on the setup condition. This is because the Te and I terminated surfaces have different density of states due to surface band bending.

2.2.1 Topography

The most common usage of STM is to measure the sample topography. The high spatial resolution of STM is based on the exponential dependence of the tunneling current on the distance between tip and the sample as described in the previous section. The most commonly used scanning mode is the constant-current mode, where we set the voltage between the tip and the sample and the tunneling current to be constants. The distance between the tip and the sample is adjusted by the feedback loop provided by the STM controller when the tip is scanning across the sample. By recording the position of the tip, we can obtain the height of the sample. An example of an STM topography measured in our lab is shown in Figure 2.2.

The underlying assumption made in this measurement is that the tip-sample barrier does not change from one position to the other on the sample surface, which is a valid assumption in most of the cases. However, one should also be aware that the tunneling current is a function of the tip-sample barrier as well as the integral of the density of states of the sample. As a result, the inhomogeneity of density of states in the sample will affect the measurement of topography of the sample. An example of such kind of effect is shown in Figure 2.3, where the "height" of the topography is strongly affected by the sample density of states. Having said that, in most of the samples where the density of states is homogeneous, STM topography is still an important surface characterization technique.

2.2.2 dI/dV SPECTRUM

As mentioned before the STM tunneling current depends on the integral of density of states of the sample. Therefore, STM can obtain the density of states information by taking the first order derivative of current over the applied voltage.

$$\frac{dI}{dV} \propto \rho_s(eV) \tag{2.8}$$

This measurement is usually done by switching off the STM feedback control loop and fixing the tip-sample seperation, and then sweeping the applied voltage V. The first derivative can be obtained by doing a numerical derivative or using the lock-in technique. An example of an STM dI/dV spectrum measured in our lab is shown in Figure 2.2.

It is important to note that STM can obtain the DOS information both in occupied and unoccupied states. This is one of the major advantages of STM over other DOS sensitive techniques such as photoemission where DOS can only be measured in the occupied states. Recent development of inverse photoemission and two-photon photoelectron photoemission can overcome this limitation, but the low resolution and complicated experiment setup of these techniques are still hindering wider usage.

2.2.3 dI/dV MAPPING

What makes STM a powerful surface characterization technique is the ability to obtain both topographic and DOS information simultaneously. There are two ways to obtain the DOS mapping. The more commonly used method is simply turning on the lock-in amplifier when taking a topograph and recording the signal from the lock-in amplifier. In this case, we can obtain a single energy layer DOS map, sometimes referred to as LIY (lock-in Y) layer. Using this technique, we keep the feedback loop on throughout the measurement which prevents the tip from being damaged by external vibration. The other method of obtaining a DOS map is to take a spectrum at each point on the surface. This is a more intuitive way of measuring a DOS map but requires better vibration isolation as the feedback loop is off when taking point spectra. The advantage of using this technique is that one can obtain multiple energy layers in one shot. It is important to note that the setup condition in these two methods are different requiring proper normalization to compare the data between these two methods. Finally, one could also combine these two techniques and take a point spectrum at each point on the surface without turning the feedback loop off. In this method, one can obtain DOS map with multiple energy layers without going out of feedback. The setup condition in this method would be the same as the first method we introduce. The disadvantage of this technique is we can only obtain data on one side of the Fermi level since we can not go across the Fermi level without turning off the feedback loop. A LIY layer we have obtained on BiTeI is shown in Figure 2.2.

2.3 QUASIPARTICLE INTERFERENCE

The quasiparticle interference (QPI) imaging technique is based on STM dI/dV mapping.

The basic idea behind quasiparticle interference imaging is to use the spatial resolution of STM to capture the standing wave created when quasiparticles scatter off defects or other structures within the crystal. The resulting interference patterns in the quasiparticle DOS can be analyzed by Fourier transform. The real space frequency of the QPI is related to the k space band structure of the crystal. By making some material specific assumptions, one can reverse engineer the k-space band structure based on the QPI patterns. The QPI imaging technique makes STM a k-space sensitive tool with high energy resolution. More importantly, STM can measure both occupied and unoccupied states.

The simulation of QPI patterns is a challenging task as the scattering process is usually complicated. To the first order, one can simulate the QPI pattern by calculating the so-called joint DOS (JDOS). JDOS is defined as the autocorrelation of the imaginary part of the quasipartice Green's function $\mathrm{Im}(G_k)$. The underlying assumption of this approach is that elastic scattering dominates the scattering process and the T matrix is equal to the identity. While the second assumption can rarely be met, JDOS serves as a good approach when we are only interested in the wave vector of the standing wave. Detailed comparisons have been made between QPI imaging and APRES results, especially autocorrelation ARPES results (AC-ARPES)[82,81].

It is important to note that FT-STM measures the scattering wave vector between the initial state and final state of a scattering process.

$$q = k_i - k_f \tag{2.9}$$

Using the scattering wave vector as a k-space momentum could lead to misleading results. The fact that a scattering process is involved in this technique actually provides us with some extra information about the quasiparticles besides the dispersion relation. One example would be the measurement of coherence factor in d-wave superconductors. We will discuss this in more detail in Chapter 3.

3

The fate of quasi-particle at the antinode

The unclear relationship between cuprate superconductivity and the pseudogap state at the antinode remains an impediment to understanding the high transition temperature (T_c) superconducting mechanism. In this chapter we employ magnetic-field-dependent scanning tunneling microscopy to provide phase-sensitive proof that d-wave Bogoliubov quasi-particles coexist with the pseudogap state on the antinodal Fermi surface of an overdoped cuprate. Furthermore, by track-

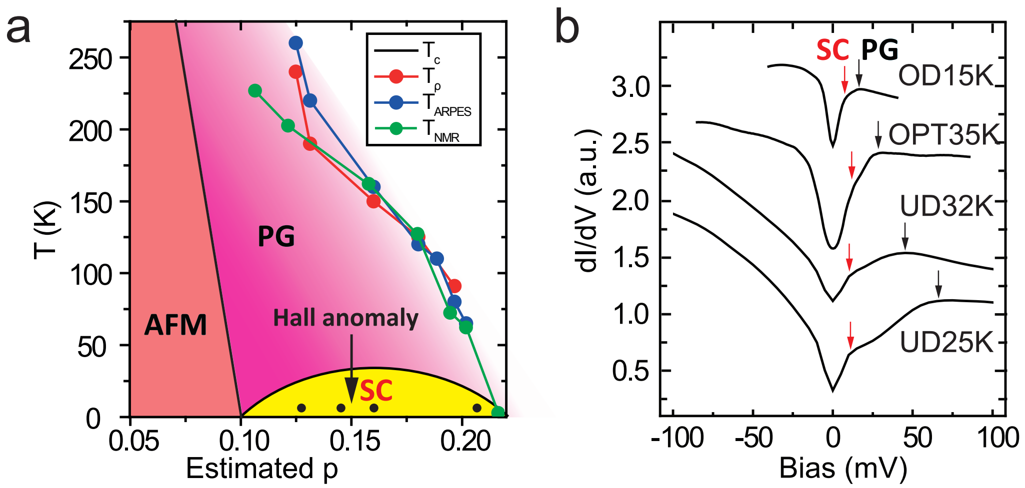

Figure 3.1: Phase diagram and spectra of Bi2201. a Schematic temperature-doping phase diagram of Bi2201, showing antiferromagnetic insulator (AFM), superconductor (SC) and pseudogap (PG) phases. Four black points represent the sample batches of this study, namely underdoped UD25K and UD32K, optimal OPT35K, and overdoped OD15K. The pseudogap transition line is plotted as measured by ARPES,[68] resistivity[68] and NMR[141]. Anomaly in the Hall coefficient[9] is marked by the black arrow. **b** The spatially averaged differential conductance g(E) for each sample. The pseudogap edge is marked with black arrows, while the low energy kink in each spectrum, generally considered to be related to the superconducting gap[18,54], is marked with red arrows.

ing the hole doping (p) dependence of the quasiparticle interference (QPI) pattern within a single Bi-based cuprate family Bi2201, we observe a Fermi surface reconstruction slightly below optimal doping, indicating a zero-field quantum phase transition in notable proximity to the maximum superconducting T_c. Surprisingly, this major reorganization of the system's underlying electronic structure has no effect on the smoothly evolving pseudogap. Some of the results from this chapter can be found in Yang He *et al.* Science 344, 608 (2014).

Superconductivity is one of several phenomena, including the pseudogap, that arises from interactions of electrons near the Fermi surface (FS) in hole-doped cuprates. The FS topology is therefore crucial to understanding these phenomena and their relationships. High-field quantum oscillation (QO) measurements[30,92,111] revealed a surprisingly small FS in underdoped $YBa_2Cu_3O_{6.5}$ (YBCO), in contrast to the conventional, large FS of overdoped cuprates like $Tl_2Ba_2CuO_{6+x}$[124].

Further high-field investigations led to the discovery of a quantum phase transition (QPT) at the low doping edge of this small FS regime, perhaps associated with a metal-insulator transition[110] or the formation of density-wave order[73]. However, the large to small FS transition presumed to occur at higher doping has thus far not been observed by QO within a single hole-doped material system. Furthermore, it is unclear whether the small FS is merely revealed by QO or possibly created by the necessarily high magnetic fields.

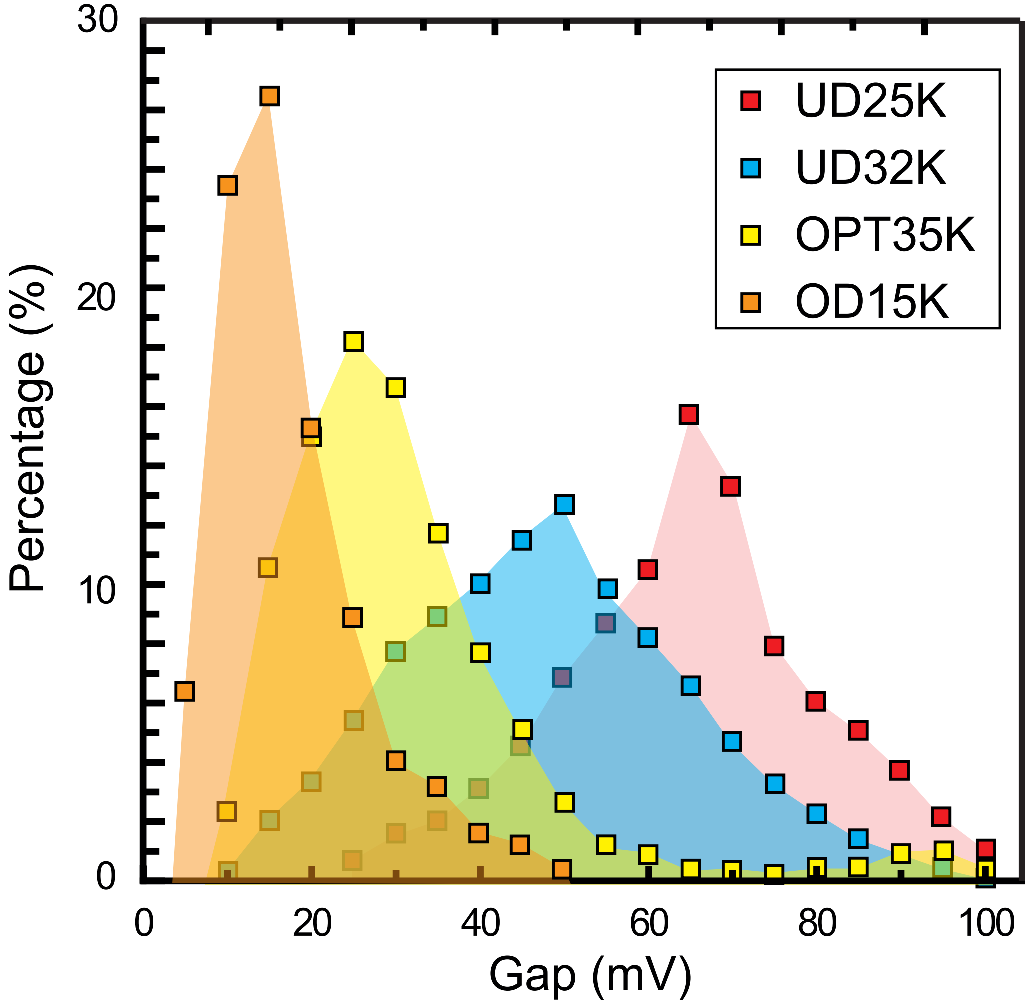

Figure 3.2: Pseudogap distribution of Bi2201. Histograms of the Δ_{PG} distributions observed in the four samples studied. Note that each histogram may have an artificial low-energy cutoff, as we are unable to distinguish Δ_{PG} when it becomes less than Δ_{SC}.

A zero field alternative to QO, angle resolved photoemission spectroscopy (ARPES), has a long history of mapping the FS in $\mathrm{Bi_2Sr_2CaCu_2O_{8+x}}$ (Bi2212)[92,34,117,127,135,125]. Here the onset of the pseudogap is defined by the opening of an anti-nodal gap and the reduction of the large FS to a "Fermi arc," which may actually be one side of a Fermi pocket, consistent with QO results[135]. The pseudogap onset may be associated with a QPT just above optimal doping at $p = 0.19$[125]. A second QPT to another competing phase is suggested to occur at lower doping ($p = 0.076$), similar perhaps to that found by QO[110,73]. However, if the transition near optimal doping is a FS reconstruction to pockets, as suggested in Yang *et al*[135], why are sharp antinodal quasiparticles seen below this doping, all the way down to p = 0.08? Further, if the antinodal FS persists down to p = 0.08[126], what impact does the QPT associated with the onset of the pseudogap at p = 0.19 have on the Fermi surface?

3.1 FERMI SURFACE RECONSTRUCTION IN BI2201

To address these outstanding questions we use scanning tunneling microscopy (STM) to study $\mathrm{(Bi,Pb)_2(Sr,La)_2CuO_{6+\delta}}$ (Bi2201). In this hole-doped cuprate, the absence of bilayer splitting and the suppression of the supermodulation by Pb doping both simplify momentum space measurements. Additionally, the separation between the expected QPT near optimal doping and the well-characterized pseudogap onset at much higher doping[68,141] allows clear investigation of the relationship between these two phenomena. We thus carry out a systematic investigation of Bi2201 at four different dopings (Figure 3.1), all of which display signatures of both the pseudogap and superconducting gap[18,54] in their low temperature spectra (Figure 3.1). The pseudogap distribution is shown in Figure 3.2.

To extract FS information, we map their differential conductance $g(r, E)$, proportional to the local density of states (DOS) of the sample, as a function of position $\mathbf{r}$ and energy E. We use ratio

---

Figure 3.3 ***(following page)*****: QPI analysis steps.** **a** 66 nm × 66 nm topography of UD32K sample with atomic resolution. **b** $g(r, 15\ mV)$ of the same FOV as in **a**. **c**, $Z(r, 15\ mV) = \frac{g(r,15\ mV)}{g(r,-15\ mV)}$. **d**, $Z(q, 15\ mV)$ is the Fourier transform of $Z(r, 15\ mV)$. Bragg peaks are highlighted with black circles. **e**, $Z(q, 15\ mV)$ is symmetrized (four-fold rotation and mirror), taking advantage of crystal symmetry to enhance signal to noise. **f**, $Z(q, 15\ mV)$ is smoothed to remove the salt-and-pepper noise and to enhance the main features.

Figure 3.3: (continued)

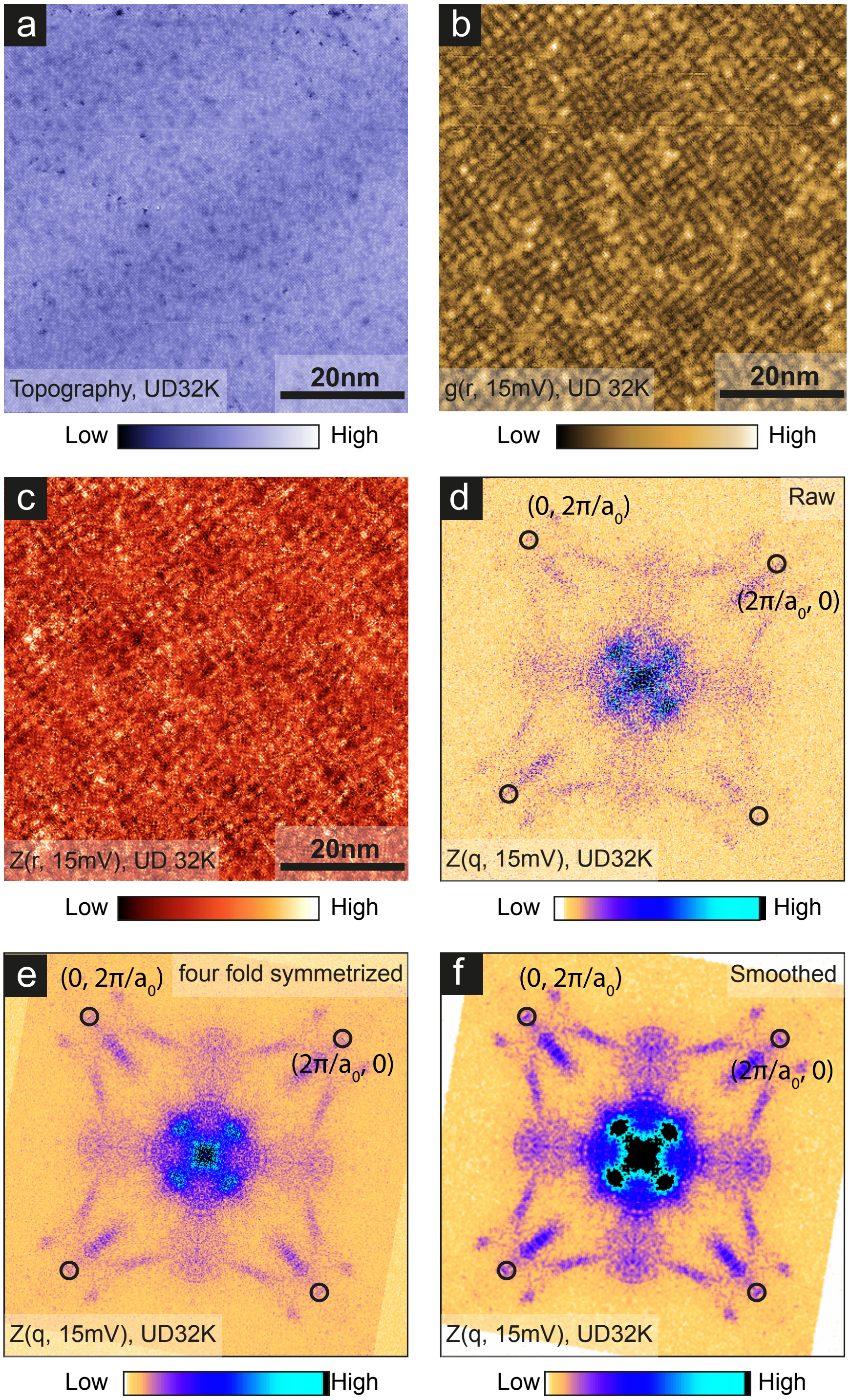

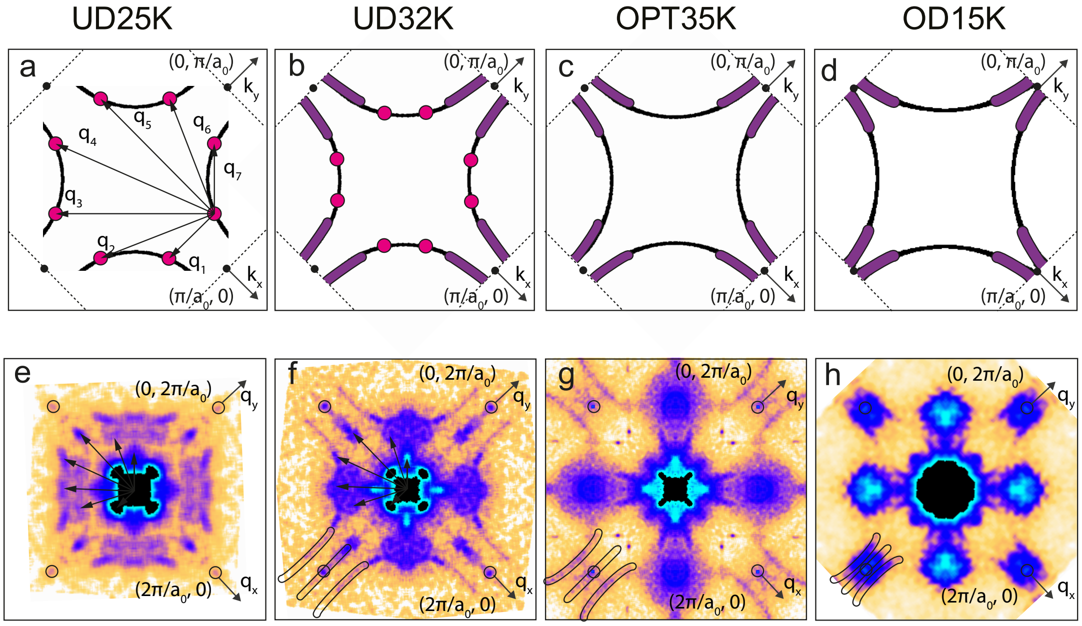

Figure 3.4: Quasiparticle interference in Bi2201. a-d Schematic of the high DOS regions which contribute to QPI, superimposed on the calculated tight-binding FS[54] for each doping. Pink circles represent regions contributing to octet QPI. Purple rectangles represent the Fermi surface sections contributing to antinodal QPI. **e-h**) Low energy $Z(q, E)$ on four samples: UD25K at E = 9 mV (**e**), UD32K at E = 5 mV (**f**), OPT35K at E = 5 mV (**g**), and OD15K at E = 3 mV (**h**). In UD25K (**e**) and UD32K (**f**) samples conventional octet QPI is observed, dispersing with energy. In UD32K (**f**), OPT35K (**g**) and OD15K (**h**) samples, novel antinodal QPI appears. The evolution from octet to antinodal QPI shows the transition from small to large Fermi surface.

maps, $Z(\mathbf{r}, E) = \frac{g(\mathbf{r},+E)}{g(\mathbf{r},-E)}$, to enhance the QPI signal and cancel the setpoint effect[47], then we Fourier transform the data. This technique can highlight dominant wavevectors which arise from elastic scattering quasiparticle interference (QPI)[82,83] between momentum space regions of high joint density of states (JDOS), thus enabling a probe of the FS. The steps of QPI analysis are shown in Figure 3.3. The QPI pattern of our samples are shown in Figure 3.4. In our most underdoped samples (UD25K and UD32K) we find a set of energy-dependent wavevectors q_i following the "octet model"[82] (Figure 3.4 a and b).

Energy dependence of QPI is shown for all four samples in Figure 3.5. In the most underdoped

UD25K sample, we observe only conventional octet QPI with clear dispersion, while in the optimal and overdoped OPT35K and OD15K samples, we observe only antinodal QPI. In the lightly underdoped UD32K sample we observe both. The absence of octet QPI in the OPT35K and OD15K samples is not yet understood. One possibility is that the octet QPI at these doping levels merges into the antinodal QPI, so that we are unable to distinguish between the two patterns. A second possibility is that increased broadening in these samples makes the effective Fermi arc long enough to connect to the antinodal region where pseudogap-induced decoherence prevents the observation of octet dispersion. A third possibility is that low-energy (near-unitary) scatterers necessary to observe octet QPI are present only in the underdoped samples.

We illustrate the octet QPI and its extinction at the antiferromagnetic Brillouin zone (AFBZ) boundary in Figure 3.6. In a superconductor, Bogoliubov quasiparticles (BQPs) disperse as $E(k) = \sqrt{(\varepsilon(k)^2 + \Delta(k)^2)}$ where $\varepsilon(k)$ is the normal state dispersion relation and $\Delta(k)$ is the superconducting order parameter. In cuprates, the gap $\Delta(k) = \Delta_0 \cos{(2\theta_k)}$ follows $d_{x^2-y^2}$ symmetry, i.e. it vanishes in the $(\pm\pi, \pm\pi)$ (nodal) directions and is maximized in the $(\pm\pi, 0)$ and $(0, \pm\pi)$ (antinodal) directions. The quasiparticle dispersion $E(k)$ thus gives rise to four "banana"-shaped contours of constant energy, depicted in Figure 3.6. At each energy, the BQP density of states (DOS) is maximized at the eight "banana" tips, due to the large value of $1/\nabla_k(E)$ in those regions. Elastic scattering between these eight high-DOS regions gives rise to the dominant QPI vectors shown. Figure 3.6 emphasizes q_1 and q_5 which lie along Bragg directions, and their relation to the AFBZ. Within the octet model, q_5 would be expected to disperse all the way to $2\pi/a_0$ at energy Δ_0. However, we show in Figure 3.6 that in both the UD25K and UD32K samples, q_5 disperses according to the octet model at low energies, then saturates at a static value $q_5^* < 2\pi/a_0$ at larger energies. The doping dependence of q_1^* and q_5^* have been previously reported and discussed[72].

From these q_is, we extract points on the Fermi surface, but we find that they extend only to the antiferromagnetic Brillouin zone (AFBZ) boundary (Figure 3.7), similar to the behavior previously

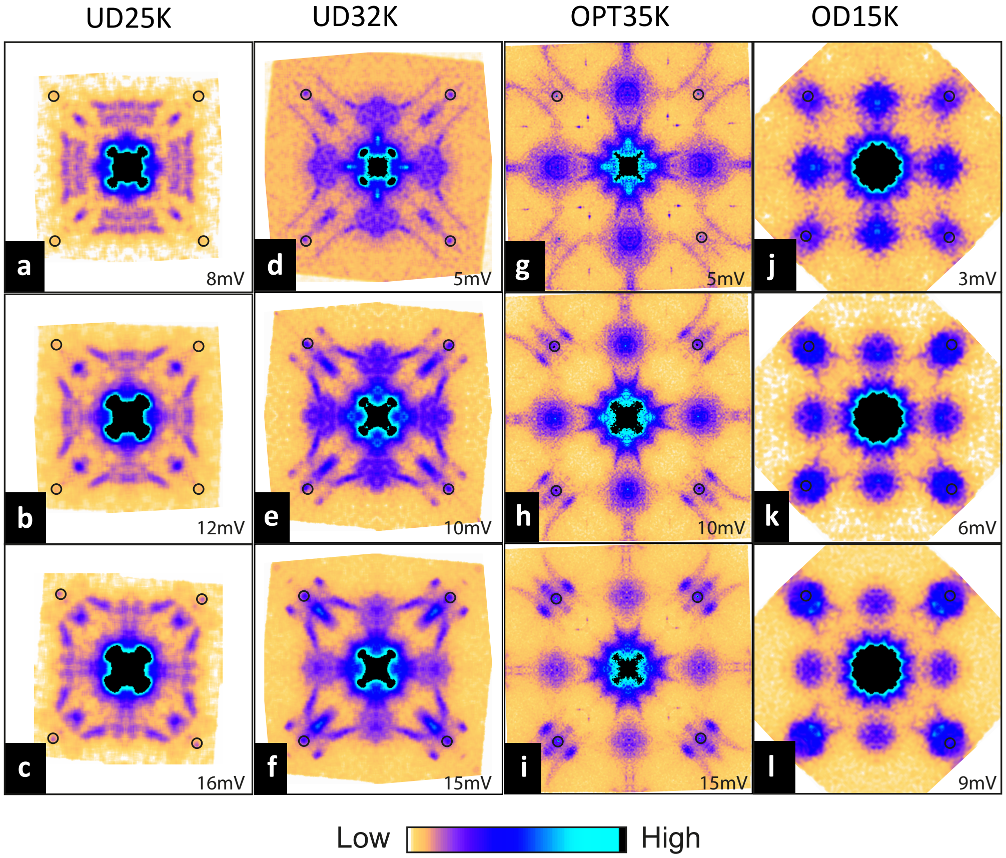

Figure 3.5: QPI energy dependence. $\mathrm{Z}(\mathbf{q}, \mathrm{E})$ is shown for three representative energies in each sample. Black circles show the Bragg peaks.

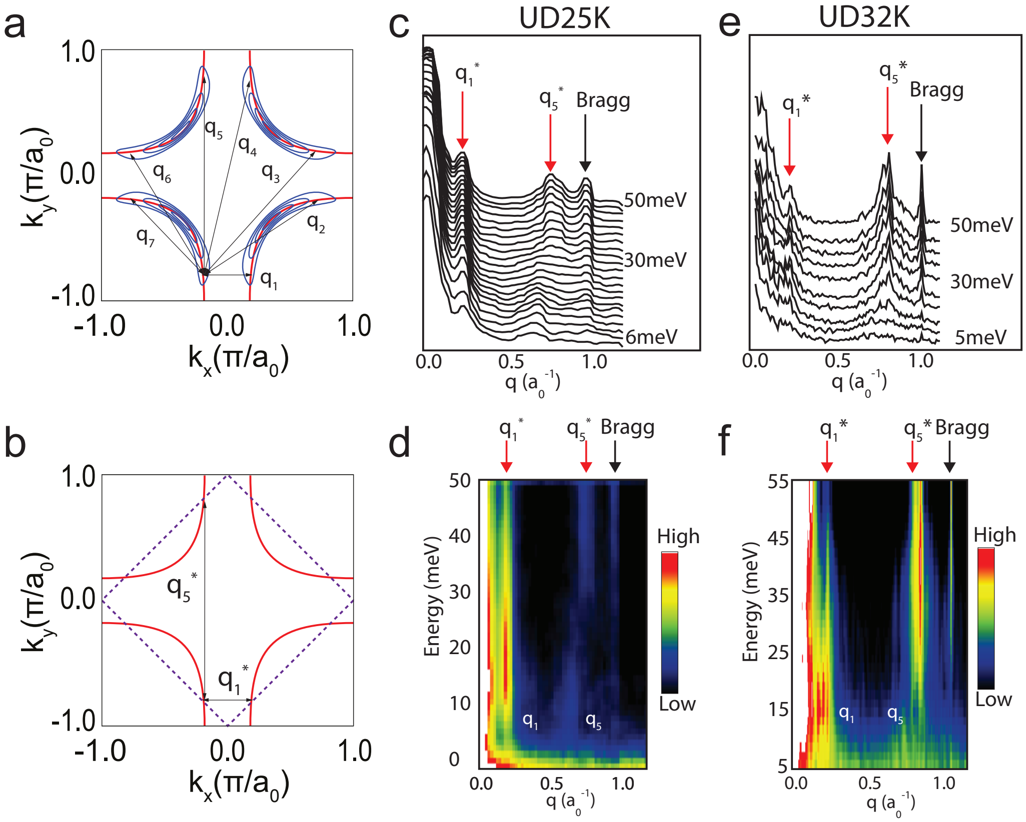

Figure 3.6: Octet QPI extinction. **a** Cartoon showing the seven dominant scattering wavevectors between the octet of high-DOS regions which disperse at energies within the superconducting gap. Schematized Fermi surface is shown in red, and schematized contours of constant energy are shown as thin blue lines. Both q_1 and q_5 appear along both the q_x and q_y axes. **b** Cartoon showing the AFBZ (purple dashed line) where q_1 and q_5 stop dispersing and merge into the static high-energy wavevectors q_1^* and q_5^*. **c,d** Two views of the same linecut of $Z(q, E)$ from $(0, 0)$ to $(2\pi, 0)$ as a function of energy in UD25K. **e,f** Two views of the linecut of $Z(q, E)$ from $(0, 0)$ to $(2\pi, 0)$ as a function of energy in UD32K. Dispersion of the octet QPI vectors q_1 and q_5 is observed. The octet vectors q_1 and q_5 disperse according to the octet model at low energies, then saturate at the static wavevectors q_1^* and q_5^* at energies above the superconducting gap.

observed in Bi2212[83].

At higher doping (in UD32K, OPT35K, and OD15K samples) we find a "triplet" feature (outlined in black in Fig. 3.4). This feature exists at multiple sub-pseudogap energies without apparent dispersion shown in Figure 3.5. However, its relative prominence at large q and low energies distinguishes it from the static checkerboard[56,57], CDW[128], smectic[72], or fluctuating stripe[98] states which appear near $q \sim (0, \frac{1}{4}\frac{2\pi}{a_0})$ at low energies or near $q \sim (0, \frac{3}{4}\frac{2}{a_0})$ around the pseudogap energy.

To understand the momentum space origin of this "triplet" QPI we follow Refs.[22,81], and, taking into account reported spectral broadening[127,5], particularly acute in the antinode, compute the autocorrelation of all antinodal states within a small energy window of the high temperature FS. This autocorrelation corresponds to the low energy antinodal JDOS in the presence of pair breaking, and matches well with the data (Figure 3.8). The "triplet" feature thus arises from states near the antinodal FS. It could be considered as a continuation of "octet" QPI and we refer to it hereafter as "antinodal QPI". We conclude that the extinction of octet QPI at the AFBZ boundary in underdoped Bi2201 (Figure 3.7), followed by the appearance of antinodal QPI at higher doping, reveals the FS reconstruction[30,92,111,124] shown schematically in Figure 3.9.

Our UD32K sample shows both octet and antinodal QPI (Fig. 3.4F), suggesting that the QPT occurs near $p \sim 0.15$ doping. We support this point by using a modified Luttinger count to compute the hole concentration p in both the large and small FS scenarios according to

$$p_{\text{large}} = \frac{2A_{\text{blue}}}{A_{\text{BZ}}} - 1 \tag{3.1}$$

$$p_{\text{small}} = \frac{A_{\text{pink}}}{A_{\text{AFBZ}}} = \frac{2A_{\text{pink}}}{A_{\text{BZ}}} \tag{3.2}$$

where A_{blue} and A_{pink} are the areas schematically indicated in the insets to Fig. 3.9. The x-axis hole concentration is independently estimated from the measured T$_c$[9]. In either small or large FS sce-

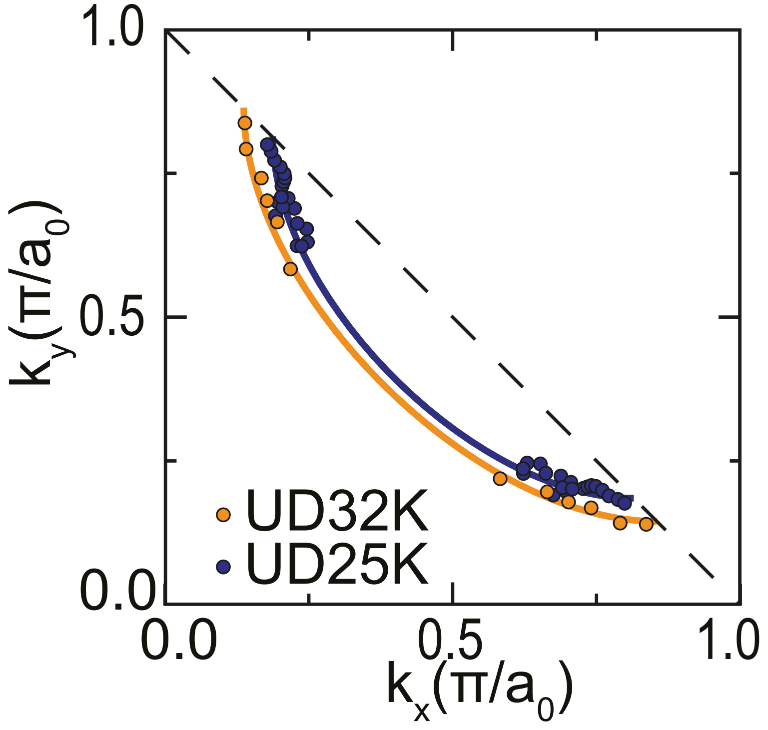

Figure 3.7: Fermi Arc in underdoped Bi2201. Locus of maximum DOS in the Bogoliubov band, from fitting octet QPI peaks. Lines show tight-binding fits. The BQP interference pattern vanishes around the AFBZ boundary (dashed line).

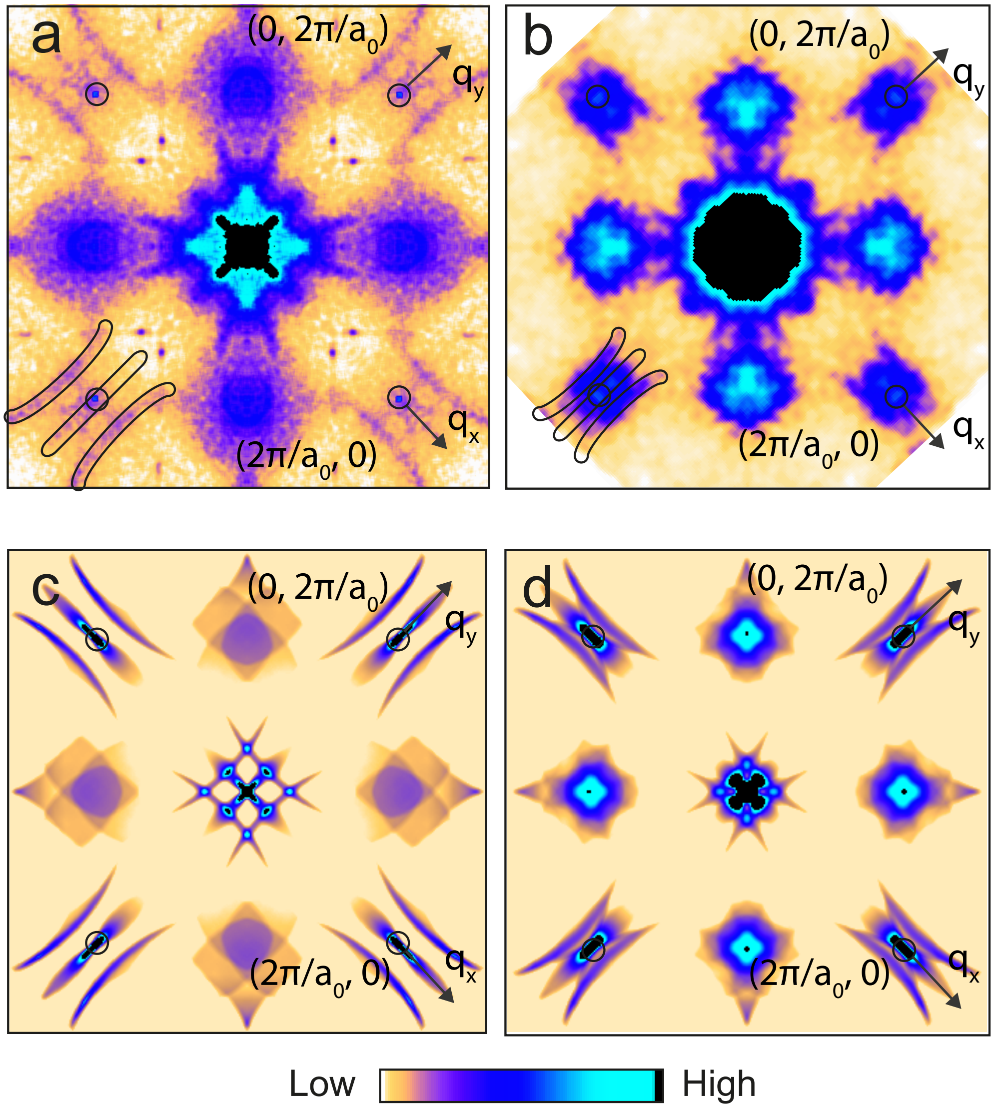

Figure 3.8: QPI simulation. a,b QPI patterns from Figure 3.4. **c,d** Autocorrelation of broadened antinodal Fermi surface sections. The autocorrelation matches well with the antinodal QPI pattern observed by experiment.

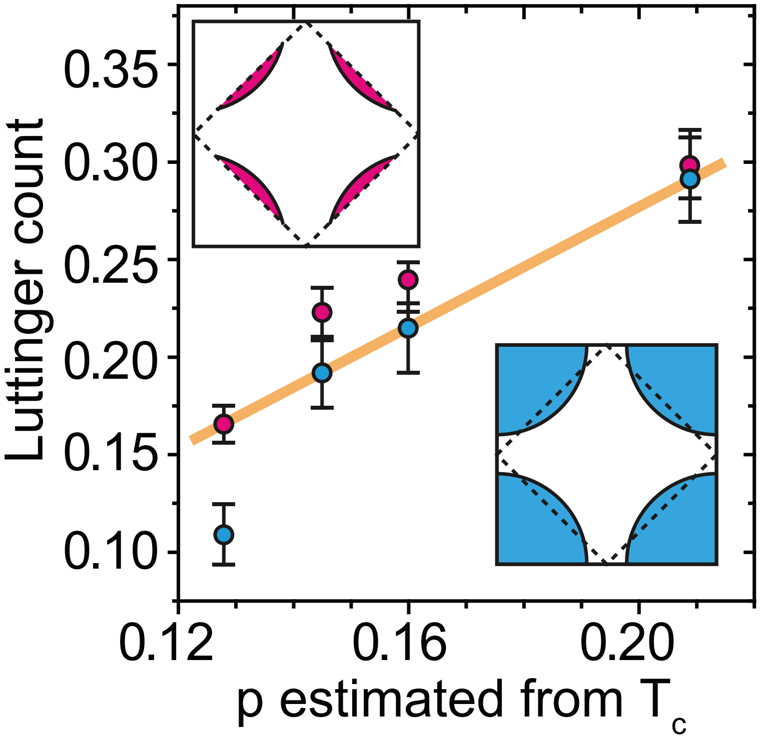

Figure 3.9: Luttinger count in Bi2201. Luttinger hole counts from small FS (pink dots and upper inset) and large FS (blue dots and lower inset) scenarios vs. hole doping estimated from T_c. Error bar on the y axis comes from the 0.01 eV chemical potential uncertainty in the tight-binding parameterization.

nario alone, we observe a sudden drop in Luttinger hole count from UD32K to UD25K. However, using p_{small} in the UD25K sample and p_{large} in the other samples, we find the expected linear relationship between the Luttinger count and the estimated hole concentration, providing further evidence of a small to large FS reconstruction upon increasing doping. Interestingly, these results agree well with high field Hall measurements of similar Bi2201 samples[12], suggesting that high field measurements in general, are revealing rather than creating small Fermi arcs.

Surprisingly, the pseudogap appears to be unaffected by this QPT, with a spectral signature that evolves smoothly through the transition. The pseudogap in Bi2201 is known[68,141,18] to exist well into the overdoped region of the phase diagram (as shown in Fig.3.1) rather than terminating near optimal doping, as in some other cuprates[116]. Thus, the FS reconstruction we observe is distinct from the onset of the pseudogap.

3.2 COHERENCE FACTOR AND HANAGURI EFFECT IN BI2201

We now face the question of how complete the coexistence of superconductivity and the pseudogap is, both in momentum- and real-space. To address the former we employ the phase-sensitive technique of magnetic-field-dependent QPI imaging (Figure 3.10). In a superconductor, the QPI participants are Bogoliubov quasiparticles (BQPs), quantum-coherent mixtures of particles and holes. The scattering intensity of BQPs depends on the relative sign of the superconducting order parameter across the scattering wavevector. Furthermore, it is known empirically[48] and theoretically[100] that sign-preserving scattering will be enhanced by a magnetic field, while sign-reversing scattering will appear relatively suppressed. A d-wave superconducting order parameter changes sign in k-space Figure 3.10a; in our OD15K sample, the two branches of the Fermi surface around the antinode are close to each other Figure 3.4, and are shown for simplicity in Figure 3.10a as a single merged region at each antinode. Thus for a d-wave superconductor with antinodal BQPs, the simplified scattering process q_A would be sign-preserving while q_B would be sign-reversing. We observe that the sign-preserving q_A scattering is enhanced in a magnetic field, while the sign-reversing q_B scattering appears relatively suppressed (Figure 3.10). This field-dependent QPI is thus fully consistent with the existence of d-wave BQPs in the antinodal FS.

For completeness, we consider several other possible causes of our field dependent antinodal QPI. First, we rule out a field-enhanced charge order, such as has been observed in vortex cores in Bi2212[56], as it would not explain the existence of both enhanced and suppressed scattering. Second,

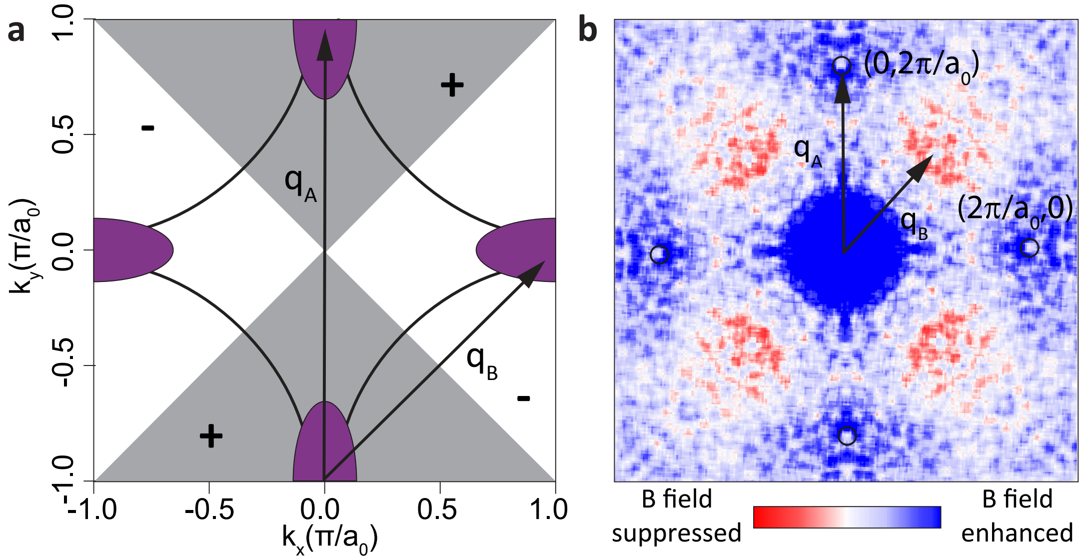

Figure 3.10: Hanaguri effect in Bi2201. **a** First Brillouin zone of the OD15K sample, with calculated tight-binding FS. White and gray areas represent opposite signs of the d-wave superconducting order parameter. The antinodal bands approach each other in overdoped materials, and are represented by merged purple half ellipses around M points for simplicity. The simplified scattering vectors q_A and q_B are shown as black arrows. **b** $Z(\mathrm{q}, 6\ \mathrm{mV}, 9\ \mathrm{T}) - Z(\mathrm{q}, 6\ \mathrm{mV}, 0\ \mathrm{T})$ showing B-suppressed (red) and B-enhanced (blue) weights, demonstrating the presence of superconducting Bogoliubov quasiparticles in the FS antinode where they coexist with the pseudogap.

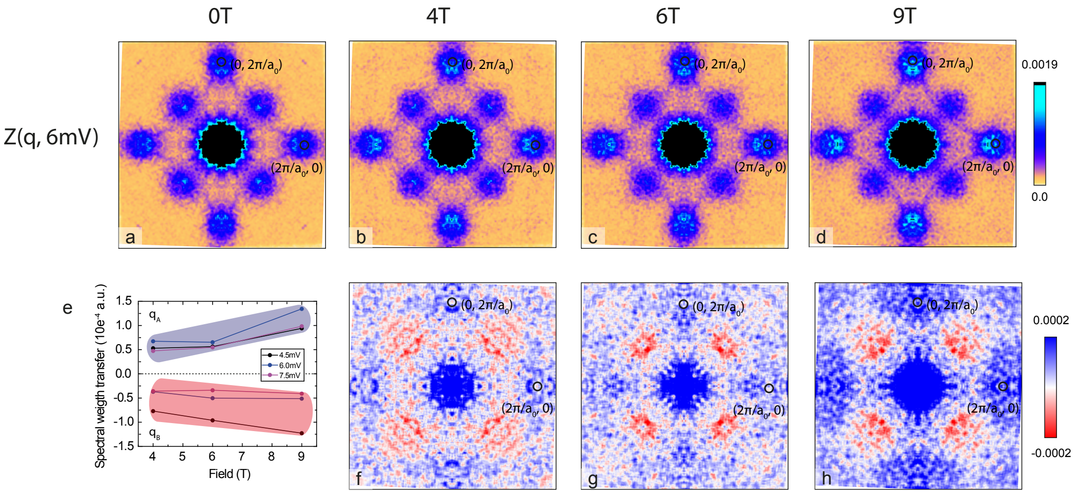

Figure 3.11: Field Dependence of QPI in Bi2201. **a-d** Symmetrized and lightly smoothed Z(q,6 mV) for all 4 fields, showing the antinodal QPI. **f**, Z(q,6 mV,4 T)-Z(q,6 mV,0 T); **g**, Z(q,6 mV,6 T)-Z(q,6 mV,0 T); **h**, $Z(q, 6mV, 9\ T) - Z(q, 6mV, 0\ T)$; **e**, Trends showing the B-dependence of low-energy scattering. Sign-preserving scattering (q_A) is enhanced while sign-changing scattering (q_B) appears relatively suppressed as B is increased.

we rule out (π, π) and incommensurate orders such as antiferromagnetism, spin density waves, stripes, or d-density waves, which would not explain the features around both (π, π) and $(2\pi, 0)$. Thus, we note that although non-phase-sensitive ARPES and STM[68,77] postulated a similar scenario, our field-dependent phase-sensitive QPI directly demonstrates the coexistence of d-wave BQPs and the pseudogap at the antinode.

Further evidence of the Hanaguri effect comes from temperature dependent data. Sign-preserving q_A scattering should be preserved unchanged with increasing temperature and upon passing above T_c. The sign-reversing q_B scattering should diminish when the temperature approaches T_c. Indeed that is what we observe in the temperature dependent data shown in Figure 3.12.

3.3 Competing between pseudogap state and superconducting coherence

Given that the pseudogap (PG) and superconductivity (SC) coexist in momentum space at the antinode, we next examine the nature of their spatial coexistence. We turn to a real space study of OD15K, where, amongst our samples, the pseudogap magnitude (Δ_{PG}) is most comparable to the superconducting gap (Δ_{SC}). To focus on the superconducting component, we suppress superconductivity with a 9 T field, and then remove the field-independent (PG) density of states by computing $S(r, E) = g(r, E, 0\,T) - g(r, E, 9\,T)$. Compared to Figure 3.13a, where spatially disparate spectra show that Δ_{PG} varies by more than a factor of five across the field of view, $S(r, E)$ shows a relatively homogeneous gap of 6 mV (Figure 3.13b), consistent with the homogeneous superconducting gap reported by a previous temperature dependent STM measurement on samples from the same batch[18]. Our results thus support the two gap scenario[117,18,77,69] and suggest that $S(r, E)$ is indicative of the local superconducting spectrum.

Dynes noted that the superconducting density of states, $\rho_s(E) = |E| / \sqrt{(E^2 - \Delta^2)}$, could be

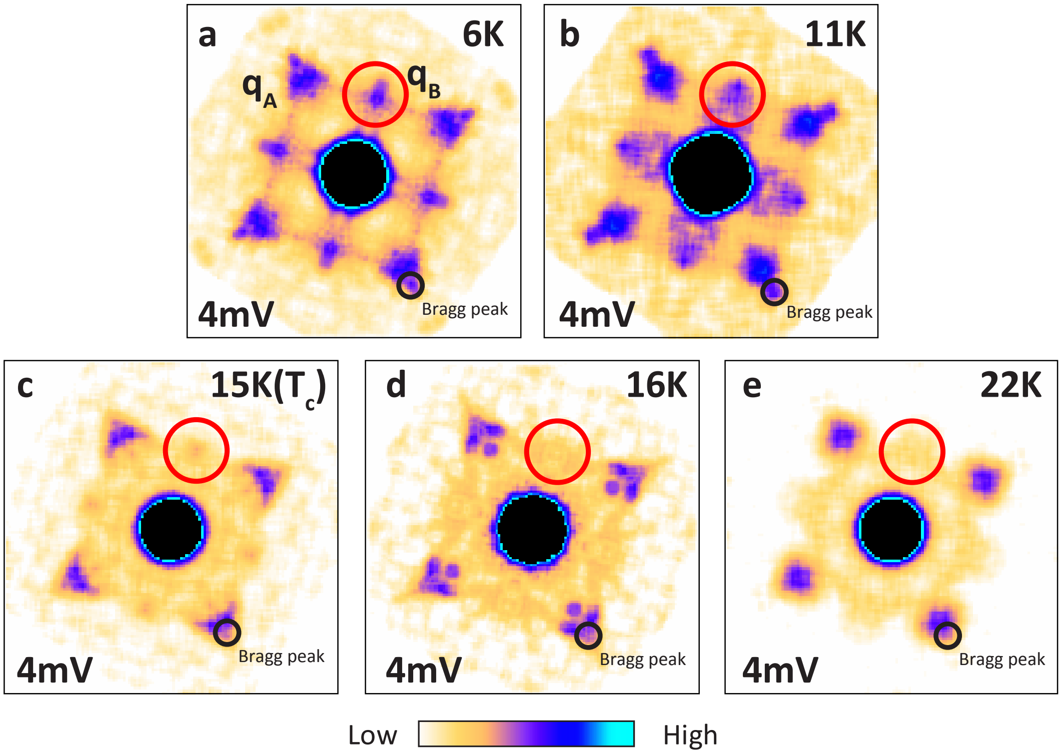

Figure 3.12: Temperature Dependence of QPI in Bi2201. a-e Symmetrized and smoothed $Z(q, 4mV)$ for all 5 temperatures, showing the antinodal QPI. The critical temperature of the sample is 15K. The Bragg peaks are highlighted with black circles. The intensity of q_A does not change when temperature goes above T_c while q_B, highlighted with red circles, diminishes gradually with increasing temperature.

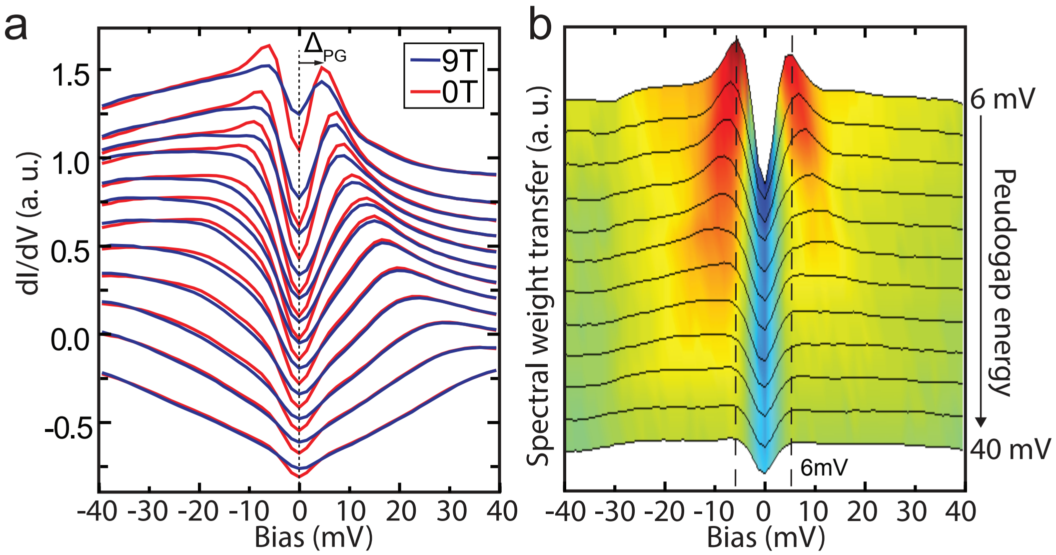

Figure 3.13: Pseudogap dependence of coherence peak in OD15K. a OD15K spectra binned by pseudogap energy (at 0T), and spatially averaged within each bin at 0T (red) and 9T (blue). Pairs of spectra are offset for clarity. **b** Magnetic field induced spectral weight transfer, $S(r, E) = g(r, E, 0\ T) - g(r, E, 9\ T)$, for these same pairs. Because the PG is B-independent, $S(r, E)$ is attributed to superconductivity. Although the $\sim 6mV$ superconducting gap shows no trend as the PG increases more than five-fold, the superconducting coherence peak decreases monotonically with increasing Δ_{PG}.

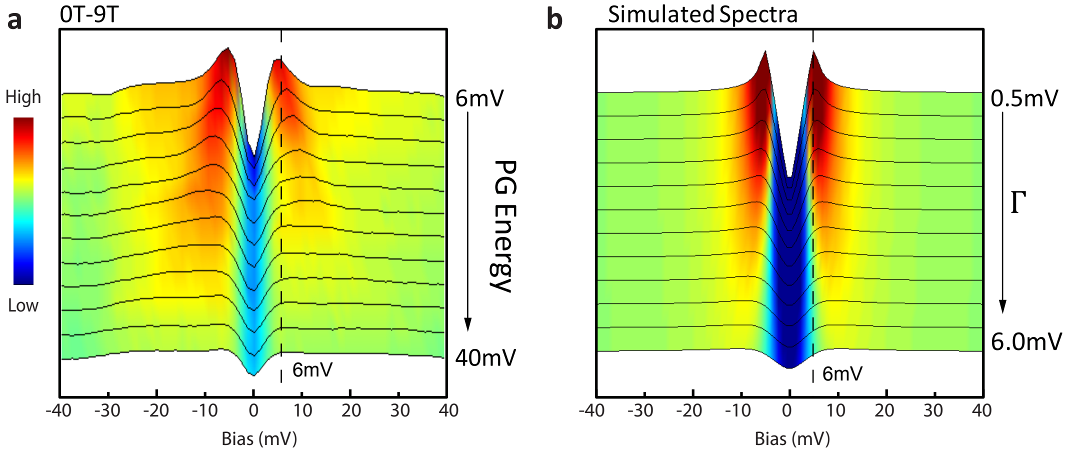

Figure 3.14: Simulated spectral broadening. **a**, A set of average spectra $\langle S(E)\rangle|_{\Delta_{PG}}$ for values of Δ_{PG} ranging from 6 mV to 40 mV, offset for clarity. The pseudogap behaves like a broadening factor: increased local Δ_{PG} has the effect of increasing Γ. **b**, Simulated superconducting density of states with 6 mV d-wave gap, broadened by the Dynes formula within increasing Γ. Note that in both the data and the simulated spectra, Δ_{SC} appears to widen with increasing Δ_{PG} and Γ respectively, although the actual energy of Δ_{SC} is constant. This can be simply understood as the effect of smoothing a sharp peak with different background on both sides: as the peak is smoothed, it will appear to move towards the side with higher background.

generalized to take into account a finite quasiparticle lifetime by writing

$$\rho_s(E,\Gamma) = Re\frac{E - i\Gamma}{\sqrt{(E - i\Gamma)^2 - \Delta^2}} \tag{3.3}$$

where Γ is the inverse quasiparticle lifetime. In Figure 3.14, we simulate the effect of increasing Γ on a d-wave superconducting spectrum with a fixed gap $\Delta_{\mathrm{SC}} = 6$ meV. We note that the broadening increases the apparent gap width (defined by the coherence peak maxima), despite the fixed $\Delta_{\mathrm{SC}} = 6$ meV. This simulation matches well with the data in Figure 3.14.

Although the inhomogeneous pseudogap does not appear to relate to the magnitude Δ_{SC} of the superconducting order parameter (vertical dashed lines in Figure 3.13b), the coherence peak amplitude and gap depth, which have been shown to scale with superfluid density[34,69,106], decay markedly in regions of large Δ_{PG} (Figure 3.15). Similar to the ARPES analysis (33), we quantify the real space decoherence effect of the pseudogap by defining a local coherent spectral weight, $C_{\pm}(r) = S(r, \pm 6\,mV) - S(r, 0\,mV)$, which increases with the height of the coherence peaks and depth of the gap. Visual comparison between maps of $\Delta_{\mathrm{PG}}(\mathrm{r})$ and $C_{+}(r)$ (Figure 3.15c,d), and their cross-correlation in Figure 3.15d, demonstrate that stronger pseudogap (largerΔ_{PG}) correlates with local suppression of superconducting coherence on a very short ($\sim 2\,nm$) length scale.

Thus, our phase-sensitive momentum-space and normalized real-space measurements demonstrate that at high doping the pseudogap coexists with superconductivity in the antinode but correlates with suppressed superconducting coherence, suggesting a competitive relationship. We also find that the pseudogap transition is well separated from a zero field FS reconstruction that occurs near optimal doping – where superconductivity is strongest. The existence of a QPT near optimal doping has been long expected and suggested by a variety of other measurements[116]. However, its differentiation from the pseudogap onset is surprising, and requires explanations of two phenomena rather than one. A number of theories have been proposed to explain the FS QPT. We can rule out the effect of crystal structure, based on its observed doping-independence[139]. Our observed FS evolution is partly consistent with the phenomenological Yang-Rice-Zhang model[136], but does not show the completion of the arc to a pocket found in the closely related microscopic FL* model[102]. Other orders such as antiferromagnetic fluctuations, charge order[50], d-density wave[59], quadrupole density wave[32,107] and vestigial nematicity[90] are all consistent with our observation of the FS QPT. With respect to the PG onset, we observe that charge modulations are similarly unaffected by the FS QPT (Figure 3.1), suggesting that the PG is associated with fluctuating charge order[98], which is pinned in all of our samples. Such charge order has recently been reported to compete with superconductivity in YBCO[20], while non-superconducting $\mathrm{La}_{1.6-\mathrm{x}}\mathrm{Nd}_{0.4}\mathrm{SrxCuO}_{4}$ shows static charge order ("stripes")[122], suggesting that such order (or its fluctuations) may be a universal competitor to superconductivity in the cuprates.

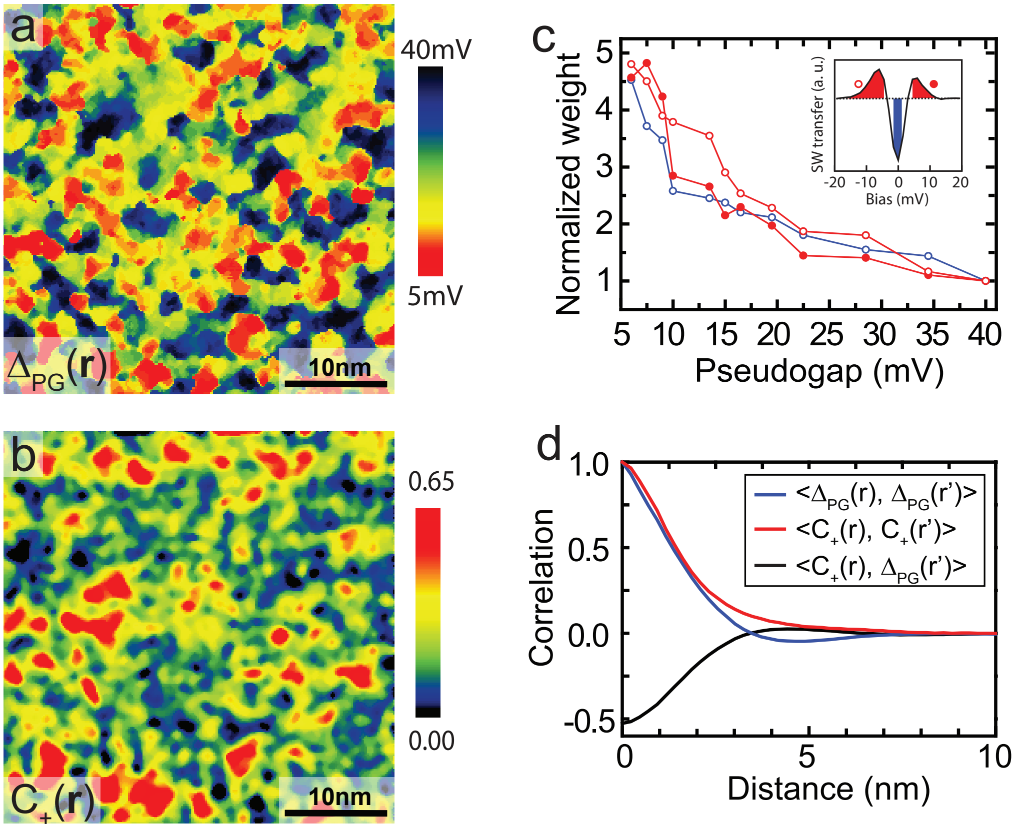

Figure 3.15: Local pseudogap-induced decoherence. **a**$\Delta_{PG}(r)$ in the same FOV from which Figure 3.4 **h** were calculated. **b** $C_+(r)$ map, defined as the difference between coherence peak amplitude and zero bias conductance: $S(r, 6\ mV) - S(r, 0\ mV)$, of the same area as **a**. The color bar is reversed for better comparison to $\Delta_{PG}(r)$. **c** Dependence of coherence peak amplitude and gap depth on Δ_{PG}. Coherence peak amplitude is integrated from $\pm 6\ mV$ to $\pm 12\ mV$ while gap depth is integrated from $-1.5\ mV$ to $1.5\ mV$. Red solid and hollow dots stand for the positive and negative coherence peak weight respectively. Blue hollow dots stand for gap depth. All data shown are normalized to their values at $\Delta_{PG} = 40\ mV$ for better comparison. **d** Angle-averaged autocorrelations of $\Delta_{PG}(r)$ (blue) and $C_+(r)$ (red) and cross-correlation of $\Delta_{PG}(r)$ with $C_+(r)$ (black).

4

d form factor charge density wave in Bi2201

In the study of cuprate superconductors, three major sets of phenomena are widely discussed, 1. electronic broken symmetry states ($\vec{Q} = 0$ and $\vec{Q} \neq 0$)[71,41,70,43,21,24,27], 2. pseudogap state above superconducting transition temperature that suppresses the density of states (DOS) at the Fermi level[120] and 3. Fermi surface reconstruction that separates the cuprate phase diagram into "small" and "large" Fermi surface regimes[93]. These three different phenomena are highly intertwined[28,37],

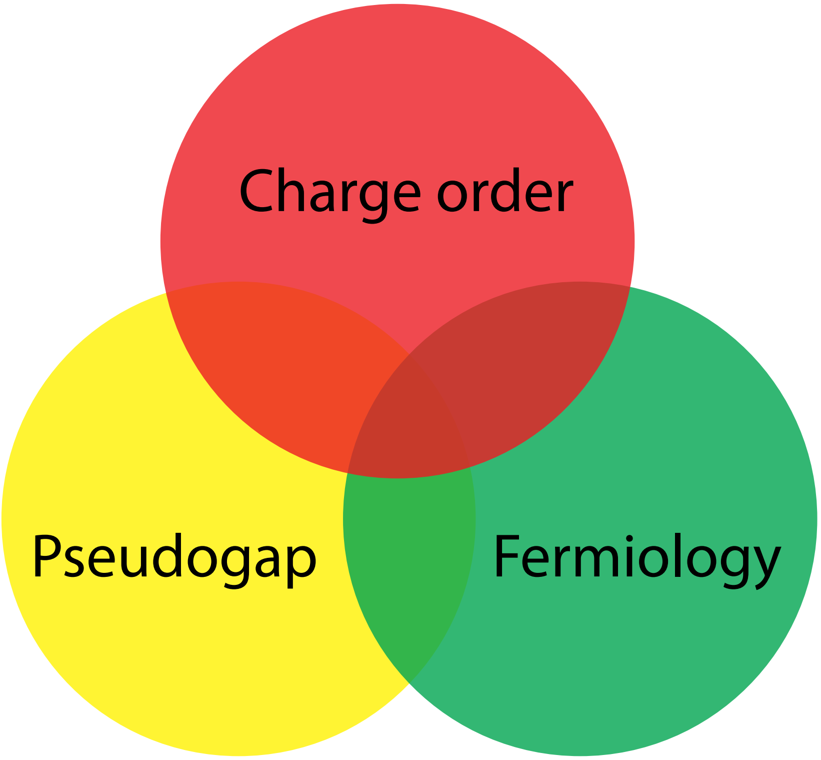

Figure 4.1: Topics of cuprate superconductor research The major topics in the research of cuprate superconductors includes charge order (both $\vec{Q} = 0$ and $\vec{Q} \neq 0$), Fermiology and pseudogap phase.

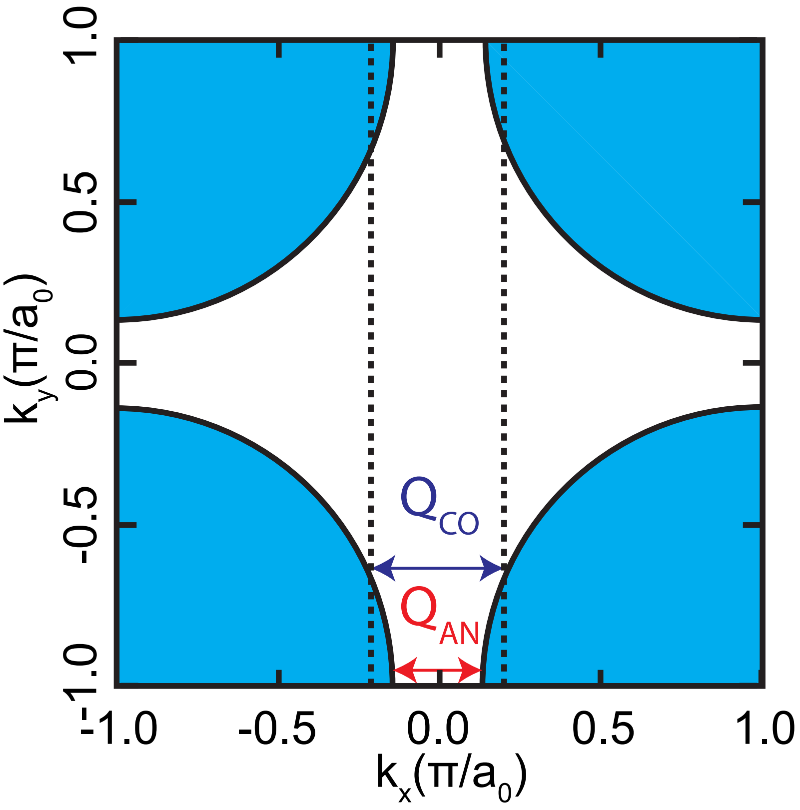

Figure 4.2: Fermi surface of Bi2201. Schematic of Bi2201 Fermi surface showing the comparison between $\vec{Q}_{\mathrm{AN}}$ and $\vec{Q}_{\mathrm{CO}}$, highlighted in red and blue arrows respectively.

and as a result, obscure the final understanding of the superconducting mechanism in high transition temperature superconductors (Figure 4.1). The existence of these phenomena in various types of cuprate superconductors is widely accepted, but the relationships between them are unclear.

Electronic broken symmetry states have been widely reported and discussed in various types of cuprate superconductors. Charge order with $\vec{Q} \neq 0$, breaking translational symmetry, has been observed in $\mathrm{La_{2-x-y}Nd_ySr_xCuO_4}$[121], $\mathrm{YBa_2Cu_3O_{6+\delta}}$(YBCO)[43,21] and more recently in B2201[24] and $\mathrm{Bi_2Sr_2CuO_{6+\delta}}$ (B2212)[27]. Intra-unit-cell (IUC) ($\vec{Q} = 0$) electronic orders breaking rotational (C4) symmetry, is reported in YBCO, B2212 and $\mathrm{HgBa_2CuO_{4+x}}$[61,75,133]. Multiple experiments also suggest a close relation between $\vec{Q} = 0$ and $\vec{Q} \neq 0$ states[41,85]. It is generally believed that broken symmetry states, such as $\vec{Q} \neq 0$ charge order that breaks the translational symmetry, would be a major perturbation to the wave function around the Fermi surface, resulting in a Fermi surface reconstruction[49,94,4]. Indeed, the evidence for such a connection is reported in Fujita *et al*[41] in double layer Bi2212, where the onset of charge order coincides with the Fermi surface reconstruction at $p \sim 0.19$. The relation between the spectroscopic pseudogap and the IUC rotational symmetry breaking states has been examined in Bi2212 as well by Lawler *et al*[71], providing strong evidence that the two phenomena are related.

Some of the major questions remaining in the discussion of density waves in cuprates are: Does the charge density wave lead to the Fermi surface reconstruction[24,114]? What are the wave vector and internal symmetry of the charge density wave[108,40,25]? To address these questions, we carry out a systematic scanning tunneling microscopy (STM) study on Bi2201, the single layer Bi-based cuprate superconductor. The "small" to "large" Fermi surface reconstruction was recently reported at $p \sim 0.15$ in this material[55]. Here we show the coexistence of a "large" Fermi surface and a d-symmetry density wave in optimal and overdoped Bi2201, highlighting the universality of d-symmetry density waves in cuprate superconductors. We also find a discrepancy between wave vectors of antinodal nesting and the charge density wave[24]. The energy dependence of the form factor indicates a close relation between d-symmetry IUC modulation and the pseudogap state.

4.1 Coexistence of charge order and "large" Fermi surface

The schematic cuprate Fermi surface is illustrated in Figure 4.2. To investigate the charge order, we map the standard differential conductance ($dI/dV = g(\vec{r}, E)$) which is typically proportional to the local density of states (LDOS). Then we perform a discrete Fourier transform of $g(\vec{r}, E)$ to acquire the Fourier components of different momenta, noted as $g(\vec{q}, E)$. The charge modulation patterns in the overdoped sample (OD15K, $p = 0.22$) and optimally doped sample (OPT35K, $p = 0.16$) are shown in Figure 4.3 c and d respectively. The clover-shaped patterns around the Bragg peaks are discussed in STM studies on Bi2212 and considered a hallmark of charge modulation in the CuO_2 plane[40]. In double layer cuprate Bi2212, charge order and the spectroscopic pseudogap diminish with increasing p and eventually disappear at around $p = 0.19$ where the compound undergoes a Fermi surface reconstruction[41,126,53]. In single layer cuprate Bi2201, the Fermi surface reconstruction happens at $p \sim 0.15$ while the spectroscopic pseudogap persists deep into the overdoped regime[55,142].

The wave vector of the charge order is the key to understand the origin of the charge order. The similarity between the antinodal FS nesting wave vector ($\vec{Q}_{\mathrm{AN}}$, highlighted as red arrow in Figure 4.2) and the observed charge order wave vector ($\vec{Q}_{\mathrm{CO}}$, blue arrow in Figure 4.2) in different kinds of cuprate superconductors indicates the two might be closely related[112]. However, most of the experiments that have been performed are in the underdoped region where the antinodal FS section is gapped out by the pseudogap. As a result, direct comparison between $\vec{Q}_{\mathrm{AN}}$ and $\vec{Q}_{\mathrm{CO}}$ has proved to be challenging. The coexistence of charge order and large Fermi surface in optimally doped and overdoped Bi2201 gives us the first chance to measure $\vec{Q}_{\mathrm{AN}}$ and $\vec{Q}_{\mathrm{CO}}$ simultaneously within the same sample. The k-space topology of the Fermi surface can be measured by mapping one of the

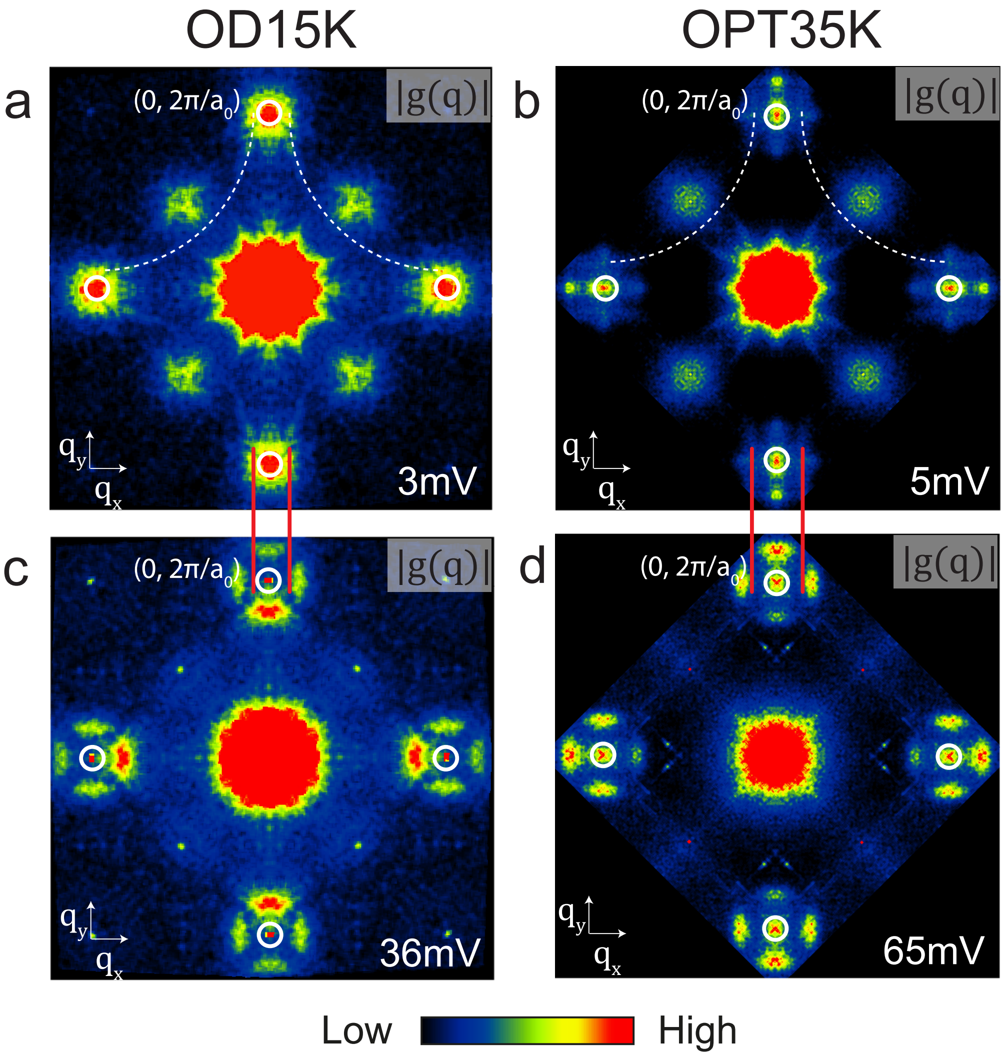

Figure 4.3: Fermi surface and charge order in Bi2201. a and b $g(\vec{q}, E)$ at low energies in OD15K and OPT35K samples. $\vec{Q}_4$, which follows the trace of Fermi surface is highlighted with white dashed lines[55,41]. The antinodal nesting vector can be measured using antinodal QPI. **c and d** $g(q, E)$ at energies larger than the pseudogap, where the charge order features are prominent around the Bragg peaks, while the same feature is missing around the central peaks. The vertical red lines spread across the figures shows the difference between $\vec{Q}_{\mathrm{CO}}$ and $\vec{Q}_{\mathrm{AN}}$. $g(q, E)$ are four fold symmetrized in **a**-**d**. Note that in this plot, we are comparing $2\vec{Q}_{\mathrm{CO}}$ and $2\vec{Q}_{\mathrm{AN}} = 4\,k_{\mathrm{AN}}$, which is twice the expected nesting wave vector.

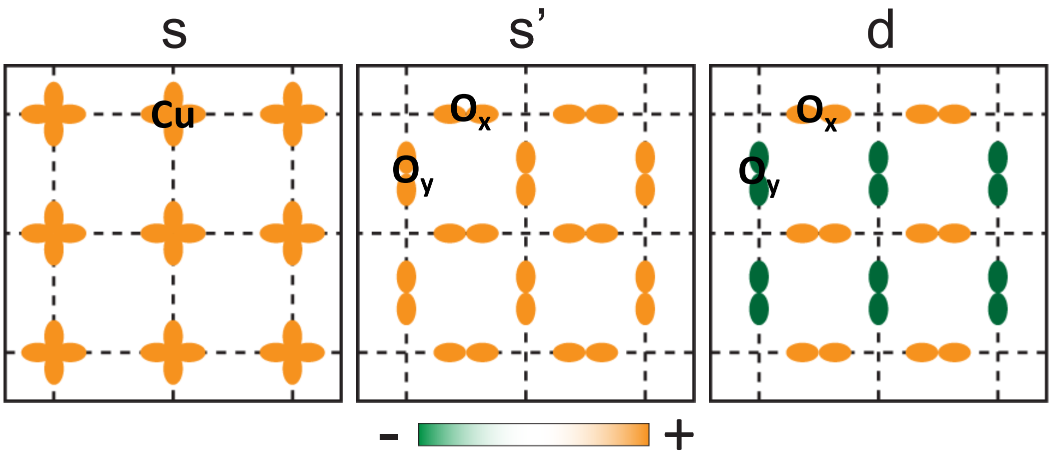

Figure 4.4: Intra-unit cell form factor on the copper oxide plane. **a** The real space modulation of the s form factor $S(r)$. Density of state is uniformly distributed on the copper atoms with zero density on oxygen atoms. **b** The real space modulation of the s form factor $S'(r)$. Density of state is uniformly distributed on the oxygen atoms with zero density on copper atoms. **c** The real space modulation of the s form factor $d(r)$. No density is distributed on copper atoms. Opposite-sign densities are distributed on O_x and O_y atoms.

QPI vectors $\vec{Q}_4$ due to the simple relation between $\vec{Q}_4$ and k_F ($Q_4 = 2k_F$)[55,41]. The white dashed lines in Figure 4.3 a and b highlight the trajectory of $\vec{Q}_4$, which shares the same shape with the Fermi surface. Figure 4.3c and d are the $g(\vec{q}, E)$ patterns at energies larger than the PG, where the charge order patterns around the Bragg peaks are prominent. The comparison between the charge order wave vector $\vec{Q}_{\rm CO}$ and the antinodal nesting wave vector $\vec{Q}_{\rm AN}$ can be visualized by the vertical red lines connecting each pair of figures. The obvious difference between $\vec{Q}_{\rm CO}$ and $\vec{Q}_{\rm AN}$ suggests that the density wave in Bi2201 does not likely originate from the antinodal section of FS, which agrees with previous results from underdoped cuprate superconductors measured by resonant X-ray scattering[24,114].

4.2 HIGH MOMENTA ANALYSIS

To identify the underlying symmetry of the density wave observed in OD15K sample, we consider a simple model where a periodic charge modulation with wave vector $\vec{Q}$ couple to intra-unit cell (IUC) states. Following Fujita *et al*[40], we formulate the charge modulation to be

$$\rho(\vec{r}) = (S(\vec{r}) + S'(\vec{r}) + D(\vec{r}))\cos(\vec{Q}\cdot\vec{r} + \phi(r)) \tag{4.1}$$

where $S(r)$ represents a uniform density on the copper atoms with zero density on oxygen atoms, $S'(r)$ represents a uniform density on oxygen atoms with zero density on copper atoms. $D(r)$ represents a form factor with opposite-sign density at the O_x and O_y sites and zero density on the copper sites. The real space modulation of different form factors are illustrated in the panels of Figure 4.4. $\phi(r)$ is the overall spatial phase of the density wave. From now on, we set phase $\phi = 0$ to be the copper sites. The schematic of Fourier transform intensity patterns of $\rho(r)$ under different intra-unit cell symmetries are shown in Figure 4.5 b-d. We want to emphasize the importance of structural peaks at $(2\pi, 2\pi)$ and the associated CO patterns around them, which serve as a major distinction between d-symmetry form factor and S, S' symmetry form factors. To gain an accurate measure of the underlying symmetry of charge modulation in our sample, we obtain high resolution data to cover the high momentum $(2\pi, 2\pi)$ peaks (45° off from the Bragg peaks). As observed in Figure 4.5a, our STM data capture sharp $(2\pi, 2\pi)$ structural peaks, demonstrating the high data quality. The similarity between our high momentum Fourier transform pattern and the modeled Fourier transform pattern suggests a d-symmetry form factor in the charge modulation observed in the OD15K sample.

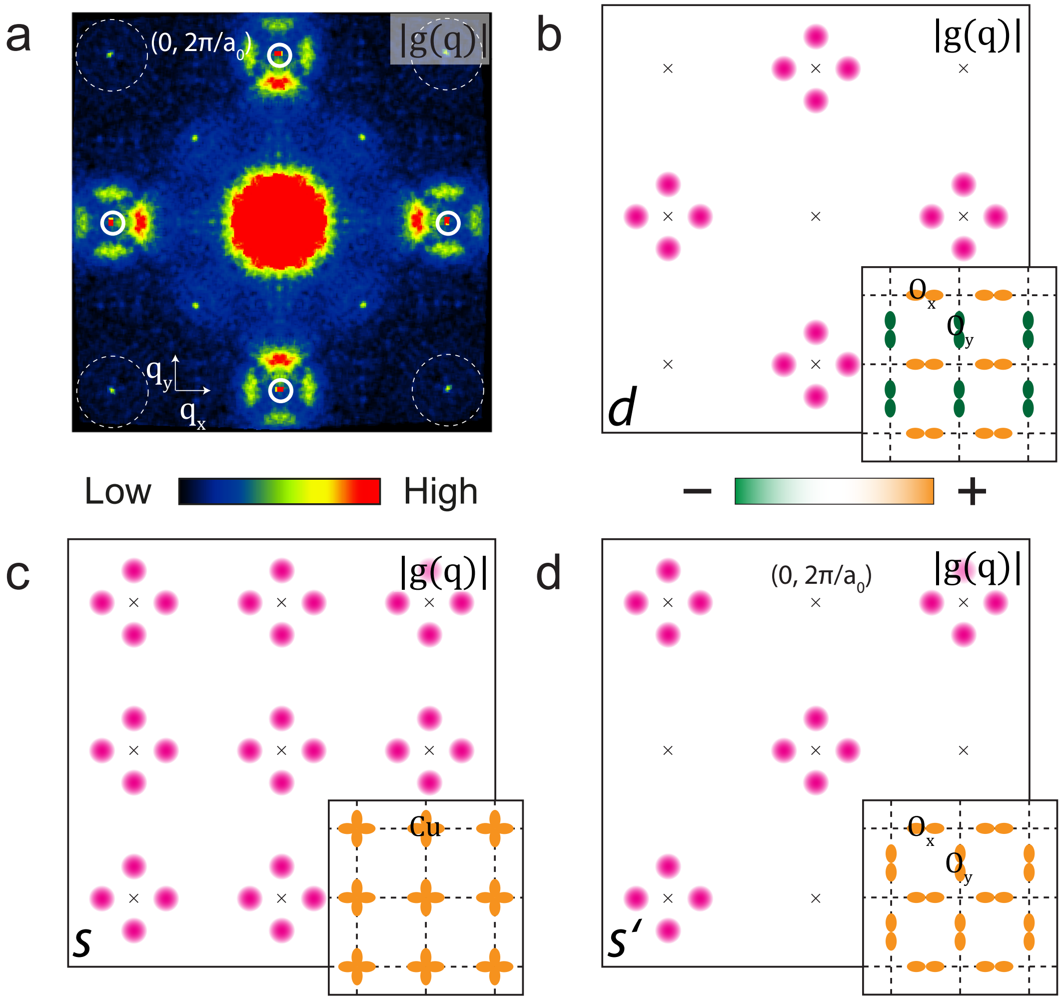

Figure 4.5: **d-symmetric density wave in OD15K shown by high momentum analysis a** Typical pattern of charge order of OD15K in energy larger than PG, same as Figure 4.3 c. Note that charge order modulation does not exist around the $(2\pi, 2\pi)$ points. **b-d** Fourier transform amplitude of charge order with d, S and S' symmetry IUC modulations respectively. The Fourier transform amplitude of the d-symmetry IUC agrees with what we observe in a.

4.3 Phase sensitive interference analysis

Phase-resolved Fourier analysis is employed to further prove that the CO pattern is indeed d-symmetric. We use interference to examine the phase coherence and phase difference between the charge modulation in the x and y directions. To begin with, we shift the CO patterns in the x and y directions back to the central peak by multiplying $g(\vec{r})$ by $\cos{(\vec{Q}_x \cdot \vec{r})}$ and $\cos{(\vec{Q}_y \cdot \vec{r})}$ respectively, where $\vec{Q}_x = \frac{2\pi}{a_0}\hat{x}, \vec{Q}_y = \frac{2\pi}{a_0}\hat{y}$ are the two Bragg vectors. We define

$$I_x(\vec{r}) = g(\vec{r}) \cos{(\vec{Q}_x \cdot \vec{r})} \tag{4.2}$$

$$I_y(\vec{r}) = g(\vec{r}) \cos{(\vec{Q}_y \cdot \vec{r})} \tag{4.3}$$

The amplitude of the Fourier transform of $I_x(\vec{r})$ and $I_y(\vec{r})$ are shown in Figure 4.6g and h. To compare the phase difference between the clovers, we calculate the Fourier transform amplitude of $I_x(\vec{r}) + I_y(\vec{r})$ and $I_x(\vec{r}) - I_y(\vec{r})$. In the d-symmetry scenario, the CO patterns in x and y direction would have a phase difference of π. As a result, the charge order component in $I_x(\vec{r}) + I_y(\vec{r})$ would be canceled out as illustrated in Figure 4.6d. On the other hand, $I_x(\vec{r}) - I_y(\vec{r})$ would have an enhanced CO pattern due to the π phase difference. As expected in the d-symmetry scenario, the calculated amplitude of the Fourier transform of $I_x(\vec{r}) + I_y(\vec{r})$ shows perfect cancellation of the CO pattern from the two different directions, which is highlighted in Figure 4.6i. Figure 4.6j shows the Fourier transform of $I_x(\vec{r}) - I_y(\vec{r})$, where the charge order peaks are prominent. Our high momentum Fourier transform pattern, as well as the phase sensitive analysis, strongly suggests the existence of a d-form factor density wave in overdoped Bi2201.

4.4 D-FORM FACTOR AND THE PSEUDOGAP STATE

To understand the connection between the charge density wave and the pseudogap, we study the energy dependence of charge order in Bi2201. The charge order of Bi2201 in low energy layers has previously been reported in Wise *et al*[129] in underdoped and optimally doped Bi2201. Here we extend the study to energies higher than the spectroscopic pseudogap and to the overdoped region. A doping dependent survey has been carried out in using four different dopings of Bi2201, namely UD25K, UD32K, OPT35K and OD15K. Shown in Figure 4.10a and b are the comparisons between charge order at low energy and at energy above the pseudogap in UD32K. In the energy range substantially smaller than the pseudogap energy, the charge order pattern is located around the central peak (noted as Q^*) in Fourier space, and shifts to the Bragg peaks at higher energy (noted as Q^{**})[67,99]. As discussed previously in this study, the CO patterns around the Bragg peaks are the signature of coupling between underlying d-symmetry IUC modulation and $\vec{Q} \neq 0$ density wave. The CO pattern around the central peak could be a result of an S-symmetry IUC modulation. The energy dependence of Q^* and Q^{**} peak intensities for four different doping of Bi2201 are shown in Figure 4.10 c-f. The vertical dashed lines represent the average pseudogap energies in each sample respectively. Q^* and Q^{**} in all four different samples share similar energy dependence, despite the difference in doping levels and Fermi surface topology[55]. The intensity of Q^* peaks at energies substantially lower than the pseudogap energy while the intensity of Q^{**} peaks at the pseudogap energies.

4.5 DISCUSSION

In this study, we provide the first observation of the coexistence of "large" Fermi surface and charge order in overdoped Bi2201. Our results on single layer Bi2201 differ from those on Bi2212 where the CO vanishes at the same doping where FSR takes place. Though the observed periodic patterns

---

Figure 4.6 *(following page)*: d-symmetric density wave in OD15K shown by phase-resolved Fourier analysis. **a-c** Schematics of real part of Fourier transform of $g(\vec{r},E)$,$I_x(\vec{r})$ and $I_y(\vec{r})$. Note that the charge order patterns in $I_x(\vec{q})$ and $I_y(\vec{q})$ have different sign due to the d-symmetry IUC modulation. **d-e** Schematic plots of $I_x(\vec{r}) + I_y(\vec{r})$ and $I_x(\vec{r}) - I_y(\vec{r})$. Due to the π phase difference between $I_x(\vec{r})$ and $I_y(\vec{r})$, the CO pattern is canceled out in $I_x(\vec{r}) + I_y(\vec{r})$. The CO pattern is enhanced in $I_x(\vec{r}) - I_y(\vec{r})$. **f-h** Fourier amplitude of $g(\vec{r},E)$,$I_x(\vec{r})$ and $I_y(\vec{r})$ of OD15K sample. **i-j** Fourier amplitude of $I_x(\vec{r})+I_y(\vec{r})$ and $I_x(\vec{r})-I_y(\vec{r})$. We can clearly see the cancellation of CO pattern in i, while CO pattern in j is enhanced.

Figure 4.6: (continued)

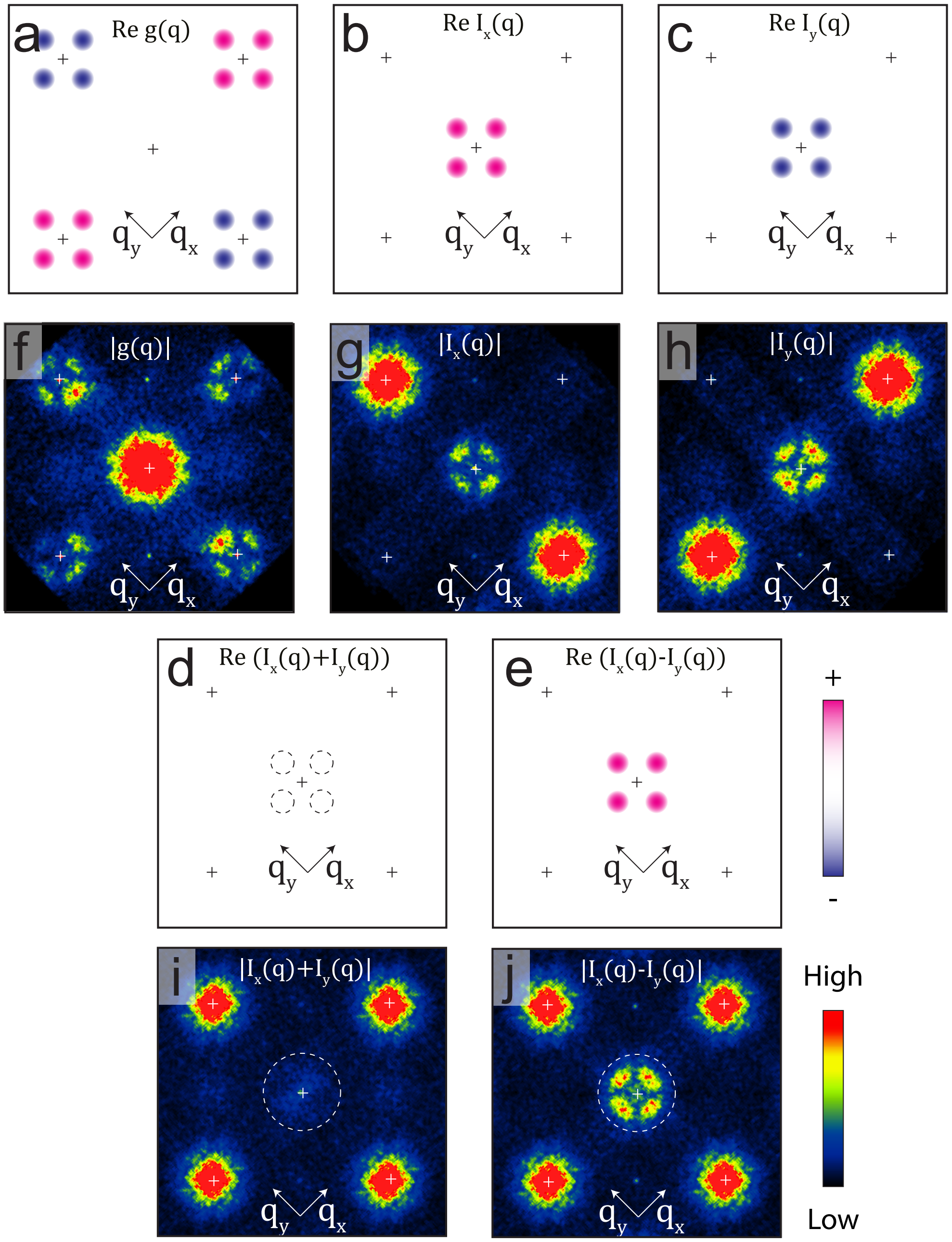

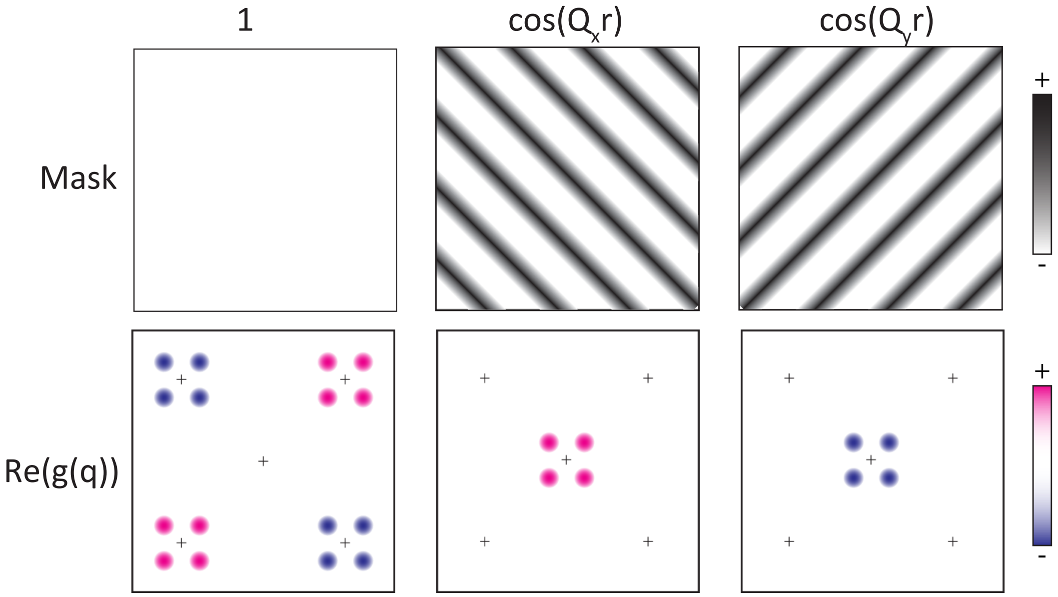

Figure 4.7: Masking procedure with cosine function. **a-c** Schematics of real space map of the masks with value 1, $\cos(\vec{Q}_x \cdot \vec{r})$ and $\cos(\vec{Q}_y \cdot \vec{r})$. Note that in the cosine mask, there are positive and negative values. **d-f** Real part of the Fourier transform of the masked maps in with d symmetry density wave.

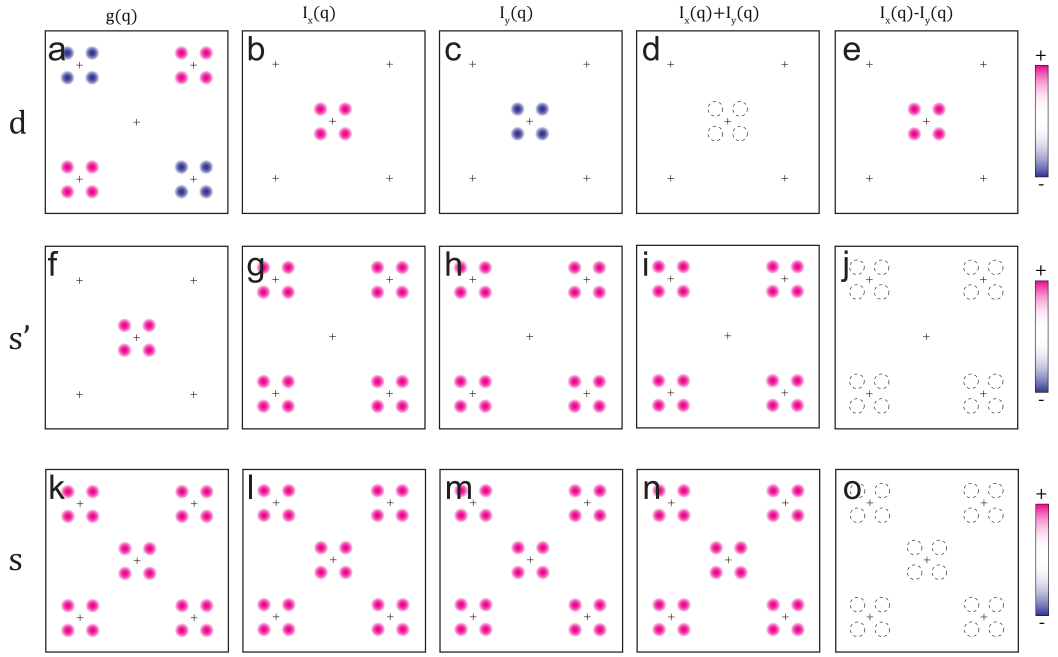

Figure 4.8: Phase-resolved Fourier analysis for different symmetries. a-c Schematics of the real part of the Fourier transform of $g(\vec{r},E)$,$I_x(\vec{r})$ and $I_y(\vec{r})$ for d symmetric charge order. **d-e** Schematic plots of $I_x(\vec{r})+I_y(\vec{r})$ and $I_x(\vec{r})-I_y(\vec{r})$. **f-j** Fourier amplitude of $g(\vec{r},E)$,$I_x(\vec{r})$, $I_y(\vec{r})$ and $I_x(\vec{r})+I_y(\vec{r})$ and $I_x(\vec{r})-I_y(\vec{r})$ in s' symmetry charge order. **k-o** Fourier amplitude of $g(\vec{r},E)$,$I_x(\vec{r})$, $I_y(\vec{r})$ and $I_x(\vec{r})+I_y(\vec{r})$ and $I_x(\vec{r})-I_y(\vec{r})$ in s symmetry charge order.

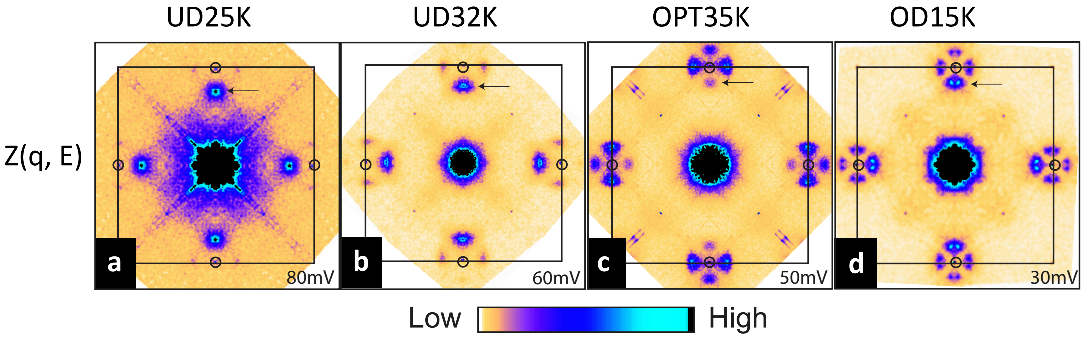

Figure 4.9: Ubiquitous d-form density wave in Bi2201. $Z(q,E)$ maps of the four samples at energies near the pseudogap energy. The charge order peak $\sim (\frac{3}{4}\frac{2\pi}{a_0},0)$ exists in all doping levels below and above the Fermi surface reconstruction reported in this work. Combining this result with the spectroscopic pseudogap shows good agreement with the phase diagram proposed by[72,128,83,98] where the charge order is related to the pseudogap phase.

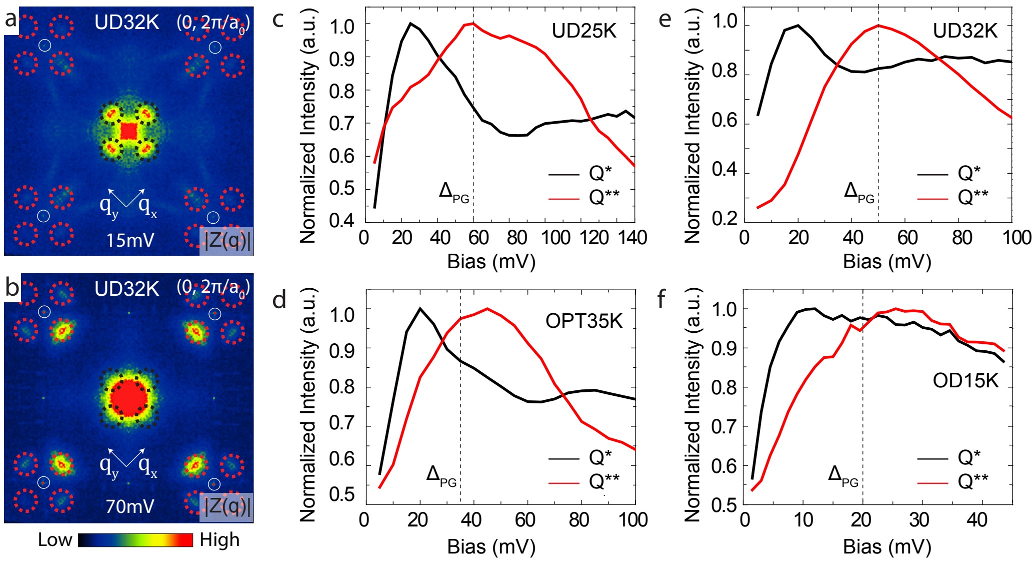

Figure 4.10: Energy dependence of d-form factor. a $Z(\vec{q}, 15\ mV)$ of UD32K sample. The charge modulation peaks are prominent around the central peak (noted as Q^*)[129]. $Z(\vec{r}, E) = \frac{g(\vec{r},+E)}{g(\vec{r},-E)}$,$Z(\vec{q}, E) = FFT(Z(\vec{r}, E))$. **b** $Z(\vec{q}, 70\ mV)$ of the same sample as a, where the charge order modulation is located around the Bragg peaks (noted as Q^{**}). No charge order peaks are observed around the central peak. **c** Energy dependence of intensities of Q^* and Q^{**} of UD25K, UD32K, OPT35K, and OD15K. Vertical black dashed lines show the average pseudogap value (Δ_{PG}) for each sample respectively. Q^{**} intensity peaks around pseudogap energy in all four of our samples from the underdoped to the overdoped region. All spectra are normalized to the maximal values. Due to the surface inhomogeneity, broadened central peaks are observed in $g(\vec{q}, E)$. As a result, the intensity of Q^* plateaus at a non-zero value when energy increase above the pseudogap energy. This effect is more significant when Q^* is closer to the central peak, which is the case in OD15K sample. Note that this type of Q^* intensity should not be taken into account in the discussion of charge order.

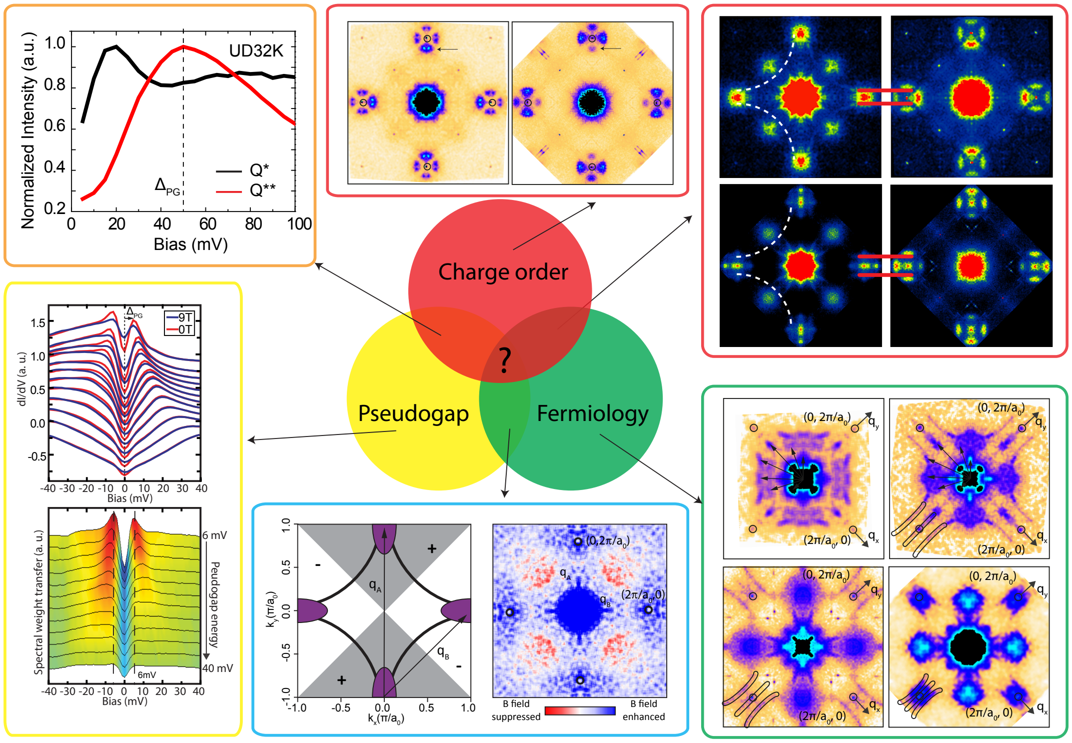

Figure 4.11: Summary of our study on Bi2201. In this work, we covered most of the topics related to cuprate superconductors. We observed d-form factor density wave in Bi2201 in both underdoped and overdoped regimes. We discovered the correlation between d-form factor density wave and the pseudogap energy. In the pseudogap regime, we discovered the competition between pseudogap and superconductivity coherence. In our study of cuprate Fermiology, we discovered a Fermi surface reconstruction around optimal doping of Bi2201. This Fermi surface reconstruction does not coincide with the onset of the pseudogap. We show the existence of BQP at the antinode using Hanaguri effect. Finally, we discover the charge order does not share the same wave vector as the antinodal FS nesting.

may be merely pinned fragments of a fluctuating charge order, this result provides new information about where charge order reside in the cuprate phase diagram. It is worth noting that the pseudogap phase persists deeply into the overdoped region of Bi2201[142,55], which coincides with the existence of a d-symmetry charge density wave in the overdoped regime. Combining the results from Bi2212[41] and Bi2201, the pseudogap state is universally accompanied by the charge density wave at low temperature in the Bi based family. Moreover, our energy dependence analysis suggests a strong correlation between the d-symmetry form factor and the spectroscopic pseudogap. Though PG and CDW show a compelling correlation, the causality between the two is still unclear.

The coexistence of the charge density wave and the "large" Fermi surface complicates the relation between the Fermi surface reconstruction and charge density wave. The driving force behind the Fermi surface reconstruction is still a heatedly debated topic in the field[4,24]. One of the possibilities would be: the charge density wave in overdoped regime is fluctuating in nature, thus failing to reconstruct the entire Fermi surface[132]. Note that STM is sensitive to fluctuating charge density waves which are short range. Further analysis is needed to identify the role that charge order plays in reconstructing the Fermi surface, especially in the presence of quenched disorder[91].

Due to the coexistence of CDW and ’’large” Fermi surface, we measure $\vec{Q}_{\text{AN}}$ and $\vec{Q}_{\text{CO}}$ in the same sample simultaneously via Fourier transform STS, providing a direct comparison between $\vec{Q}_{\text{AN}}$ and $\vec{Q}_{\text{CO}}$. Our experiment suggests that the charge density wave is not likely to originate at the antinodal section of the Fermi surface[24]. More sophisticated model, such as bond density wave[4,108], is needed to explain the existence of the density wave in cuprate superconductors.

Our high momentum Fourier analysis and phase sensitive Fourier analysis unveil the predominant d-symmetry form factor of the CDW in overdoped Bi2201, which strongly supports the universality of the d-wave CDW in cuprates, as suggested by recent REXS[25] and STM experiments on three different families (Bi2201, Bi2212, YBCO and Na-CCOC)[40]. It is also worth noting that CDW order and superconductivity not only coexist in the low temperature regime of the cuprate phase diagram, but also share the same d symmetry, indicating the particle-particle (SC) and particle-hole (CDW) channels might share the same or similar underlying interactions, thus sheding light on the origin of the unconventional superconductivity in the cuprates.

5

Topological Kondo Insulators

Recent predictions suggested that topological surface states might exist in some heavy fermion materials, particularly SmB_6. However, the hybridization of the localized and itinerant electrons in SmB_6 and its relationship to the low temperature transport anomaly is still unclear. The correspondence between spectroscopic studies and transport measurements is missing in this system. Here we use scanning tunneling microscopy to conduct a systematic atomic resolution spectroscopic study of the non-polar cleaved surface of SmB_6, and to reveal a robust hybridization gap that universally spans the Fermi level at low temperature. Employing a cotunneling model, we measure the hybridization amplitude between the conduction band and the f band. Our temperature dependent spectroscopy results provide a simple connection between spectroscopic studies and the low temperature transport anomaly at $\sim$ 50 K in SmB_6. Some of the results from this chapter can be found in Yee, He *et al.*, arXiv: 1308:1085(2013).

The classification of solids based on topological invariants has led to the recognition of new electronic phases of matter. The existence of non-trivial topology in band insulators, combined with time reversal or crystal symmetries, gives rise to topologically protected metallic surface states[39]. Potential applications ranging from spintronics to quantum computing have directed intense research efforts toward the surface states of topological band insulators such as Bi- and Sn-based chalcogenides[8,52,103]. Recently, it was suggested that similar topological arguments could apply to more strongly correlated insulators in which a filled band of heavy quasiparticles hybridizes with the conduction band to open an insulating gap[31]. In these heavy fermion compounds, itinerant electrons screen the local magnetic moments of the lattice in a process known as the Kondo effect[23]. At temperatures below the Kondo coherence temperature (T^*) the conduction electrons hybridize with the magnetic moments to open up an energy gap in the density of states (DOS). In a Kondo insulator, the hybridization gap spans the Fermi level E_F, causing a metal to insulator transition upon cooling through T^*. In a topological Kondo insulator (TKI), protected chiral surface states span the Kondo hybridization gap.

Recently, there has been tremendous interest in the heavy fermion material SmB_6 as a possible TKI[31,115,76]. SmB_6 undergoes a metal to insulator transition around 50 K[84,6,26], which was attributed to hybridization between the $4f$ localized moments and the $5d$ conduction band. However, multiple experiments[60,89,38] have suggested that the hybridization gap in SmB_6 exists at much higher temperature than the metal-insulator transition. The onset of the metal-insulator transition is also accompanied by a sign change of the Hall coefficient[6] and a peak in the magnetic susceptibility[19], which cannot be fully explained by Kondo transition.

Below ∼3 K, a saturation of the resistivity[84,26] indicates a residual conducting channel, which could be explained by the existence of topologically protected surface states[31,115]. This hypothesis has been investigated by a number of recent point contact spectroscopy[140], transport[64,131,65,118], quantum oscillation[74], and angle-resolved photoemission spectroscopy (ARPES)[87,134,60,143,113,89,38] experiments. The dispersion and orbital chirality of some surface states[60], the half integer Berry phase from Landau levels[74], and the transport response to magnetic impurities[65] are strongly suggestive of nontrivial topology in SmB_6.

Although evidence is accumulating for topological surface states on SmB_6, precise understanding of their properties is presently limited by poor understanding of the hybridization gap within which they emerge. DC transport[84,26,36] and optical reflectivity[123] studies typically report a gap of $\Delta \sim$ 5-10 meV, but both the activation energy fits and the Kramers-Kronig transformations necessary to extract these gap energies may be affected by residual states in the gap[26,36,45]. Larger gaps of 19 meV and 36 meV have also been observed by optical transmissivity[45] and Raman spectroscopy[95], respectively. However, transport and optical techniques cannot determine the gap center with respect to E_F. Most angle-resolved photoemission spectroscopy (ARPES) experiments, which measure filled states only, loosely identify the magnitude of the hybridization gap as the binding energy of the sharp f band just below E_F, typically E_B ∼14-20 meV[87,134,60,89,143,113]. However the lack of information on the empty state side makes even the simple question of whether the gap spans the Fermi level elusive[38,89].

Planar tunneling and point contact spectroscopy (PTS/PCS) purport to measure the complete DOS, showing the T-dependent opening of a gap ranging from ∼3 to 22 meV[46,7,36,140]. However, PCS lineshapes in SmB_6-SmB_6 junctions vary dramatically with junction size,[36] while PTS and PCS heterojunction experiments have shown an asymmetric peak on the positive energy side of the gap[7,140], in contrast to the preponderance of theoretical and experimental evidence for an electron-like conduction band[76,3,87,134,60,89,38,143,113]. It remains crucial to access the bare DOS and full hybridization gap.

Single crystals of SmB_6 were grown using an Al flux method[64], glued to a copper sample holder using conducting epoxy Epotek H20E, cleaved in cryogenic ultrahigh vacuum around 30 K, and immediately inserted into our homebuilt STM. STM tips were cut from PtIr wire and cleaned via field emission on polycrystalline Au foil. The tip was held at virtual ground, while a bias voltage was applied to the copper sample holder in electrical contact with the back side of the sample, opposite the cleaved face where the tunneling current into the PtIr tip was measured. The sample and tip remained in a cryogenic UHV environment, allowing the cleaved surface to stay clean for months. We imaged four samples, with multiple tip-sample approaches on each cleaved surface, in regions separated by many microns. Topographies were acquired by moving the tip across the sample and using a feedback loop to vary the tip-sample separation to maintain a constant tunneling current. Spectroscopic measurements were carried out at fixed tip-sample separation, at temperatures between 2 and 50 K, in fields up to 9 T, using a standard lock-in technique with bias modulation at 1115 Hz. We conducted experimental tests to ensure our spectral features are not caused by tip induced band bending.

Previous studies[87,46,7,36,140] on SmB_6 averaged over at least several microns of surface area. Spatial averaging over large regions of SmB_6 is problematic because, unlike the first generation of Bi-based topological insulators, which are layered materials with natural cleavage planes, SmB_6 is a fully three dimensional material whose cleavage properties are unknown. SmB_6 has a CsCl-type cubic crystal structure with alternating Sm^{2+} ions and ${B_6}^{2-}$ octahedra, shown in Fig. 5.1a. It is therefore expected that complete $Sm^{2+}(001)$ or ${B_6}^{2-}(001)$ terminations would be polar, resulting in surface band bending. On the other hand, a partial Sm surface may suffer from structural reconstructions as seen by low energy electron diffraction (LEED)[10,87]. Although the topologically protected surface states are expected to exist on all surface morphologies, their manifestation may be influenced by the differing electronic environments in which they live. Furthermore, the possible shifts of the hybridization gap and/or coexistence of topologically trivial states on some surfaces may short out the fundamental chiral states of interest for transport devices. It remains crucial to quantify the hybridization gap itself, and to understand its variation with surface morphology. Here we use atomically resolved scanning tunneling microscopy and spectroscopy (STM/STS) to probe variations in differential tunneling conductance (dI/dV) across multiple $\mathrm{SmB_6}$ surface morphologies. We demonstrate that vacuum tunneling conductance is dominated by the bare DOS, and shows a robust hybridization gap that universally spans the Fermi level on all surfaces at low temperature. Temperature dependence of tunneling spectra unveils a possible mechanism of the metal-insulator transition at $\sim 50\,\mathrm{K}$.

5.1 SURFACE CHARACTERIZATION OF $\mathrm{SmB_6}$

The topographic image in Figure 5.1 c shows the cleaved surface of $\mathrm{SmB_6}$ with atomically flat terraces of typical ∼10 nm extent. These terraces are separated by steps of height equal to the cubic lattice constant $a_0 = 4.13$ Å, which identifies the cleaved surface as the (001) plane. After the conclusion of the STM experiment, we performed electron back scatter diffraction (EBSD) and x-ray photoelectron spectroscopy (XPS) measurements, which confirmed the (001) orientation and showed a B-rich surface, consistent with previous measurements[10].

Figure 5.2 shows high resolution topographies of the two distinct surface morphologies we observed. Figure 5.2 a shows a rarely observed 1×1 square lattice, which we identify as a complete Sm layer, similar to the complete La layer of (001) cleaved $\mathrm{LaB_6}$ previously imaged by STM[96]. Because the Sm atoms have a valence of ∼2+, this polar surface may be energetically unfavorable[42], explaining its typical limitation to small regions approximately 10 nm × 10 nm on the cleaved surface. The polar instability of the 1×1 surface could be resolved by removing half of the Sm atoms from the

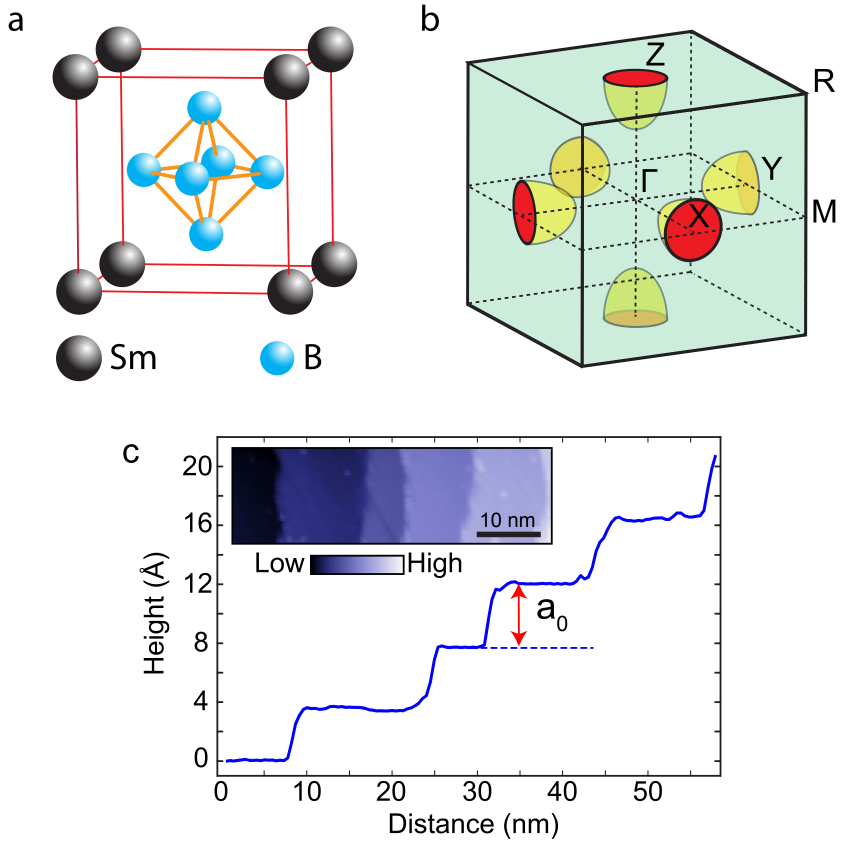

Figure 5.1: Crystal structure of SmB$_6$. **a** Schematic crystal structure of SmB$_6$ with cubic lattice constant $a_0 = 4.13$ Å. **b** Schematic 1st Brillouin zone of SmB$_6$. High symmetry points are marked. **c** Topographic linecut across five atomically flat terraces. The difference in the vertical height between adjacent terraces is a$_0$. Inset shows a 50 nm by 15 nm topography of these terraces.

topmost layer, consistent with the 2×1 striped surface in Figure 5.2b. This surface is consistent with LEED observations of a 2×1 reconstruction[87] and ARPES observations of band-folding[134,60] on the cleaved SmB_6 surface.

5.2 HYBRIDIZATION AND KONDO GAP

Having assigned chemical identities to these surface morphologies, we image their differential tunneling conductance dI/dV. The tunneling dI/dV is typically proportional to the local DOS[13] (although we will discuss later an additional interference contribution that can manifest in Kondo systems). Figure 5.2c-d show spatially averaged spectra representative of each of the surfaces, emphasizing some ubiquitous features, as well as dramatic differences between the morphologies. The dominant features common to all surfaces are the spectral minimum located near the Fermi energy, and the relative prominence of the peak on the filled state side, compared to the empty state side. Both observations are consistent with the bare DOS for a hybridized electron-like conduction band[35].

Spectra on the 1×1 surface show a peak at -165 mV (Figure 5.2), which we identify as the hybridized Sm^{2+} $^6H_{7/2}$ multiplet typically seen by ARPES at E_B ~150-160 mV[134,60,89,143,113], and a peak at -28 mV, which we identify as the hybridized $^6H_{5/2}$ multiplet typically seen by ARPES at E_B ~14-20 meV[87,134,60,89,143,113]. The downward energy shift of both these STM-observed $^6H_{7/2}$ and $^6H_{5/2}$ multiplets compared to the average ARPES observations could arise from the polar catastrophe at the 1×1 surface[88,143]. The polar catastrophe would cause the movement of electrons towards the surface to decrease the charge of the surface Sm layer, and would shift the Fermi level up, causing the hybridized f bands to appear lower in comparison. Indeed, one ARPES experiment[38] that boasted no evidence of surface reconstruction from LEED[87] or band-folding[134,60], showed similarly higher binding energies of -170 mV and -40 mV, consistent with a chemical potential shift at a

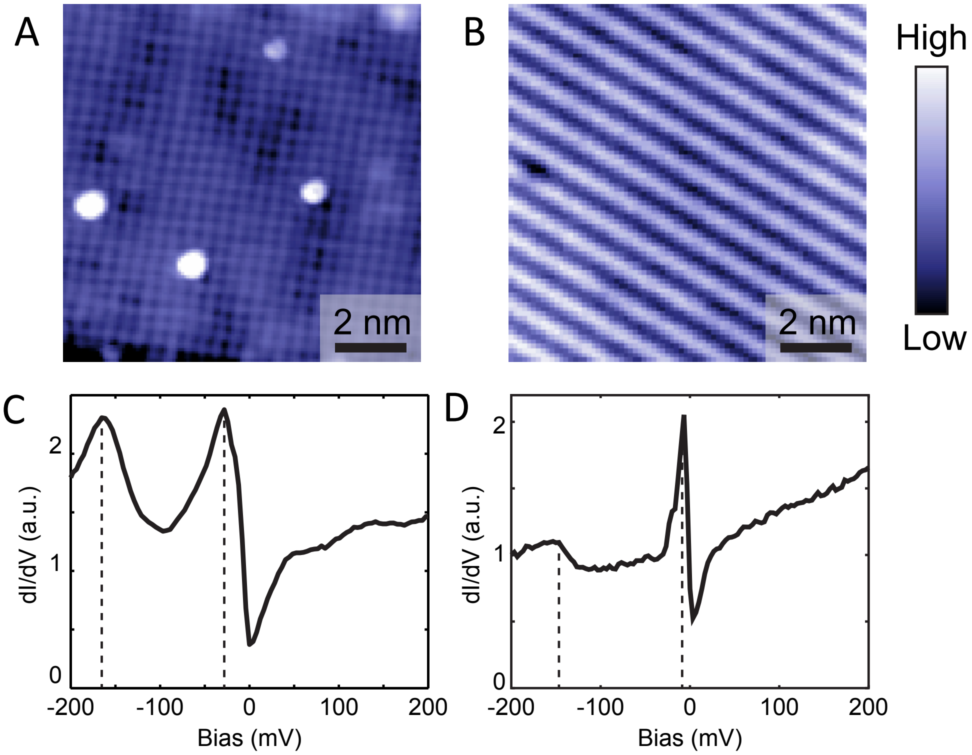

Figure 5.2: Surface morphology of SmB$_6$ and representative dI/dV. a-b Representative 10 nm × 10 nm topographic images of the two different surface morphologies. **a** 1×1 Sm termination. ($T = 9.5$ K, $V_s = -200$ mV, $R_J = 10$ GΩ.) **b** 2×1 half-Sm termination. ($T = 8.5$ K, $V_s = -100$ mV, $R_J = 5$ GΩ.) **c-d** Spatially averaged dI/dV representative of each of the surface morphologies shown in **a-b**. **c** dI/dV on the 1×1 surface. Dashed lines indicate peaks at -165 mV and -28 mV. ($T = 9$ K, $V_s = -250$ mV, $R_J = 2$ GΩ, bias excitation amplitude $V_{\mathrm{rms}} = 2.8$ mV.) **d** dI/dV on the 2×1 surface. Dashed lines indicate peaks at -155 mV and -8 mV. ($T = 8$ K, $V_s = 200$ mV, $R_J = 1$ GΩ, $V_{\mathrm{rms}} = 1.4$ mV.)

polar 1×1 surface.

We expect that the 2×1 surface is nonpolar, and may provide a better view of the bulk f bands and hybridization process. Spectra on the 2×1 surface at low T show a broad peak at around -155 mV, and a remarkably sharp feature centered at -8 mV (Figure 5.2), both more consistent with $^6H_{7/2}$ and $^6H_{5/2}$ multiplet energies observed by ARPES[87,134,60,89,143,113]. The -8 mV peak is extremely homogeneous on clean terraces of varying sizes. The -8 mV peak shows no change in a c-axis magnetic field up to 9 T, unlike the 'in-gap' state whose field-suppression was observed by NMR[19]. Some ARPES experiments have also observed a weakly dispersing state around -8 mV to -4 mV, which has been claimed as the 'in-gap' signature of a TKI[87,89]. However, a topological 'in-gap' state should continuously span the full hybridization gap, so we argue that the sharp -8 mV state is the manifestation of the $4f$-$5d$ hybridization itself, observed specifically on the 2×1 surface.

The temperature dependence of the 2×1 spectra are shown in Figure 5.3a. The prominent peak-dip features, which are the signatures of Kondo hybridization, persist from 8 K to 50 K. Our result agrees well with previous photoemission experiment showing that the Kondo hybridization gap persists up to temperature much higher than the metal-insulator transition around 50 K[29]. These results appear contradictory to our understanding of the Kondo lattice where the resistivity changes upon the onset of Kondo hybridization. Various explanations for the discrepancy between the spectroscopic studies and low temperature transport anomaly have been provided in the literature, such as coherence-decoherence transition[140], charge fluctuation[86], and collective magnetic mode[1,105].

It is well known that tunneling into a Kondo impurity – a single magnetic atom in a non-magnetic host – reflects the intrinsic impurity level and conduction band, as well as the extrinsic quantum mechanical interference between those two tunneling channels. The interference manifests as a Fano resonance – an asymmetric dip-peak feature that dominates the tunneling signal[78]. Similarly in Kondo lattice systems, the interference effect may dominate the differential tunneling conductance, giving an asymmetric dip-peak but obscuring the underlying DOS[137,80,35,130,17]. To further understand the temperature dependence of spectra, here we use the clean Kondo lattice model of Figgins *et al.*[35] to extract the hybridization amplitude and self-energy of the f electrons from the STM-measured dI/dV spectra on the 2×1 surface of SmB$_6$.

5.3 MODELLING dI/dV SPECTRA

We modeled the dI/dV spectra using the formalism of Figgins and Morr[35,11], in which dI/dV can be decomposed as the sum of three terms from the conduction band, the f band, and the interference of the two channels. In this model, t_f/t_c is the ratio of the tunneling amplitudes into the f band and the conduction band,

$$N_c = \mathrm{Im}[G_c(k,\omega)] \tag{5.1}$$

$$N_f = \mathrm{Im}[G_f(k,\omega)] \tag{5.2}$$

$$N_{cf} = \mathrm{Im}[G_{cf}(k,\omega)] \tag{5.3}$$

where N represents the DOS of the respective channel, and the hybridized Green's functions are given by

$$G_c(k,\omega) = \left[G_c^0(k,\omega)^{-1} - v^2 G_f^0(k,\omega)\right]^{-1} \tag{5.4}$$

$$G_f(k,\omega) = \left[G_f^0(k,\omega)^{-1} - v^2 G_c^0(k,\omega)\right]^{-1} \tag{5.5}$$

$$G_{cf}(k,\omega) = G_c^0(k,\omega) v G_f(k,\omega) \tag{5.6}$$

The hybridized Green's functions are expressed in terms of the hybridization amplitude v and the bare Green's functions: $G_c^0(k,\omega) = [\omega + i\gamma - E_k^c]^{-1}$ and $G_f^0(k,\omega) = [\omega + i\gamma - E_k^f]^{-1}$ where γ is the self energy and E_k^c and E_k^f are the unhybridized band structures of the conduction and f band, respectively. The hybridized bands take the form

$$E_k^{\pm} = \frac{1}{2}\left(E_k^c + E_k^f\right) \pm \sqrt{\frac{1}{2}\left(E_k^c - E_k^f\right)^2 + v^2}. \tag{5.7}$$

Because the conduction band of $\mathrm{SmB_6}$ is stiff around the Fermi level, high k-space resolution is required to compute the low energy spectrum around the Fermi surface where the hybridization gap locates. Using spatial point group symmetry, we can reduce the calculation in the 1st BZ into 1/3 of the 1st BZ, focusing on a single ellipsoid. This step reduces the computation time by a factor of 3. Afterwards, we can shift the center of the grid to the center of the ellipsoid. Once again, using the point group symmetry of the ellipsoid itself, we can reduce the grid into 1/8 of the reduced grid. By this point, we have reduced the computation time by a factor of 24.

The key approximation we are making in doing these k space reductions is that the k-space region far away from the Fermi surface plays a negligible role in the process of hybridization. As a result, one is free to move these regions wherever is preferable for the calculation. Using this approximation, we maintain the grid of calculation to be a cube.

After the reduction of grid we have made in the previous paragraphs, we can calculate a spectrum in the energy range from -80mV to 80mV in a time scale around tens of seconds. The actual computation time depends on the energy resolution and other parameters we set. This is still not ideal for the fitting procedure.

To accelerate the spectrum computational speed, we used a dimension reduction method in the calculation, which is illustrated in Figure 5.4. The basic idea here is to convert the grid from Cartesian coordinate to polar coordinate and integrate the angular components out by hand. The first step is to convert the long axis (k_z axis) to k_z' axis, such that the ellipsoid becomes a sphere in the k_x,

k_y and k'_z space. Then we can write down the band structure in polar coordinates.

$$E(k_x, k_y, k_z) \to E(k_x, k_y, k'_z) \to E(k_{radius}, \theta, \phi) \to E(k_{radius}) \quad (5.8)$$

It is clear that only the radius matters and we can integrate out the angular degrees of freedom. This results in a simple one-dimensional band structure as illustrated in Figure 5.4d. After the dimension reduction, we can calculate a spectrum in 0.2 seconds, a two orders of magnitude reduction in computation time.

We modeled the Sm $5d$ conduction band as an ellipsoid centered at the X point of the three-dimensional Brillouin zone, with semi-major k_F axes $0.401(\pi/a_0) \times 0.401(\pi/a_0) \times 0.600(\pi/a_0)$ and $E_{\text{min}} = -1.6$ eV in agreement with ARPES measurements[60]. We modeled the Sm $4f$ band as a non-dispersive flat band spanning the Brillouin zone at energy E_0^f. The parameters such as E_F, t_f/t_c and self energy γ can be obtained by minimizing a cost function. As shown in Figure 5.3a, for spectra acquired on the 2×1 surface, we found a good match to the main features of the data for $E_0^f = -3.5$ meV, $v = 90$ meV, and $t_f/t_c = -0.025$. These results are consistent with our analysis using a separate Kondo lattice model by Maltseva *et al.*[80].

The differential tunneling conductance is modeled as

$$\frac{dI}{dV}(V) = t_c^2 N_c(V) + t_f^2 N_f(V) + 2 t_c t_f N_{cf}(V) \quad (5.9)$$

where $N_c(V)$ and $N_f(V)$ represent the bare DOS, t_c and t_f are the respective tunneling amplitudes, and $N_{cf}(V)$ represents the quantum mechanical interference between the two tunneling channels[35,130,17,11]. The interference term is an extrinsic contribution to our dI/dV measurement, which is undesirable because it masks the desired bare DOS signal. The fits shown in Fig. 5.3a quantitatively reproduce the peak position, peak width including the shoulder on the low-energy side,

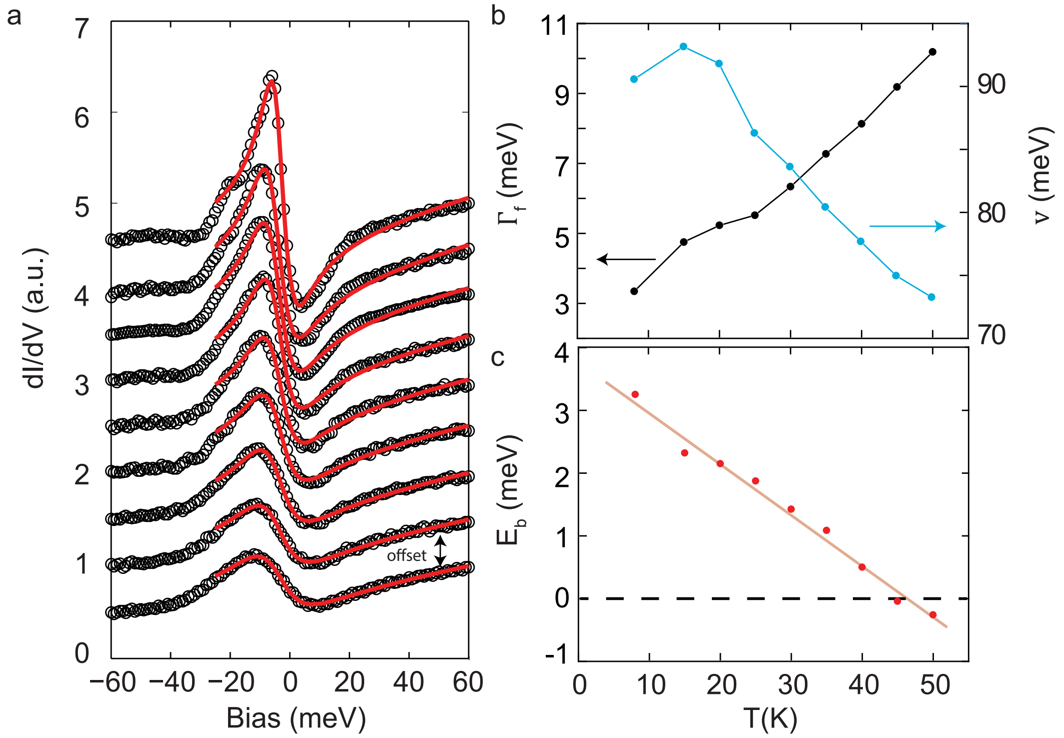

Figure 5.3: Temperature dependence of spectra on 2×1 surface. **a** Temperature dependent spectra from 8 K to 50 K. Spectra are fitted to the cotunneling model[35] from -30 mV to 100 mV. **b** Temperature dependence of f-band self-energy Γ_f (black) and hybridization amplitude v (blue). **c** The energy minimum of the upper band E_b (at the X point) is calculated from v in (b) using Eq. 5.9. The variance of E_b estimated based on different fitting energy range is less than 1meV.

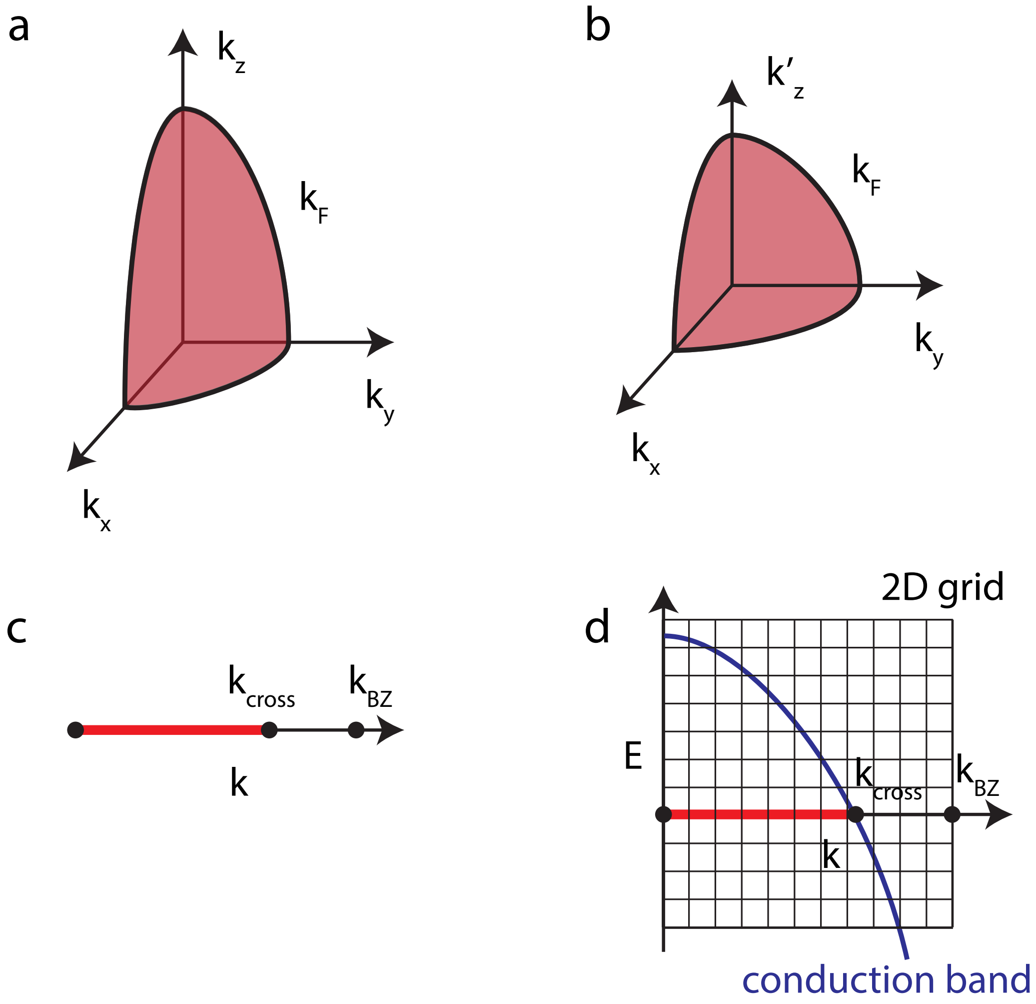

Figure 5.4: Dimension reduction of the SmB$_6$ band structure. **a** 1/8 of an ellipsoid representing the shape of the conduction band. **b** Converting the ellipsoid to a sphere by changing k_z into k'_z. **c** Integrate the angular dimension out, reducing the three dimensional band structure into a one dimensional band structure. The crossing point of the conduction band and the f band is highlighted. **d** The conduction band is plotted in the new one-dimensional k-space. The calculation is done in 2 dimensional grids (momentum and energy).

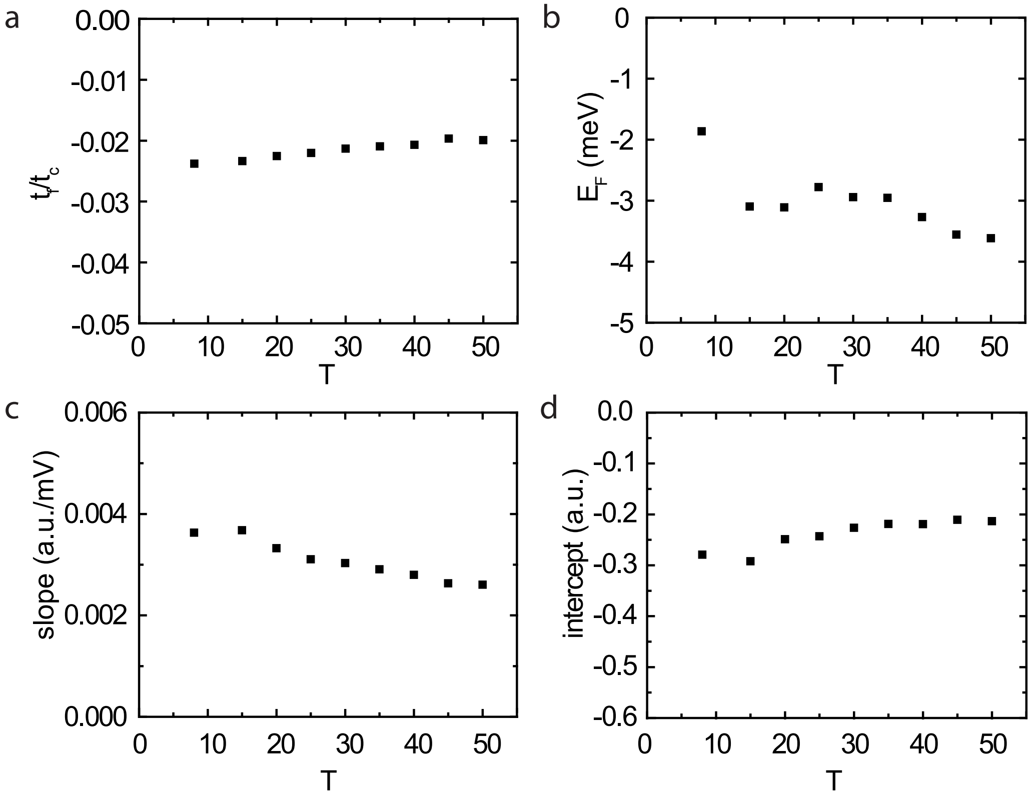

Figure 5.5: Temperature dependence of fitting parameters. **a** Temperature dependence of t_f/t_c. **b** Temperature dependence of f band energy E_F. Note that the change of E_F is also reported in[29,86]. **c-d** Slope and intercept of the linear background. The arbitrary unit used here is the same as Figure 5.3.

and gap width including positive energy kink, on the non-polar 2×1 surface. The fit is done on the spectra in the bias range from -30 mV to 100 mV to avoid the spectroscopic kink around -40 mV. The existence of the kink might be related to a magnetic mode[1] or f-band splitting which is beyond the scope of this study. The other fitting parameters are plot in Fig.

reffig:C6Fitting as a function of temperature.

The use of Eq. 5.9 allows us to take a step beyond recent PCS[140] and STM[104,105] results by providing the hybridization amplitude directly (shown in Figure 5.3b). The hybridization amplitude v drops from ~ 100 meV to ~ 75 meV which is in good agreement with ARPES measurements[86,29].

The band structure after hybridization can be calculated from the pole of the Green's function:

$$E_k^{\pm} = \frac{E_k^c + E_k^f}{2} \pm \sqrt{\left(\frac{E_k^c - E_k^f}{2}\right)^2 + v^2} \tag{5.10}$$

To resolve the discrepancy between the spectroscopic studies and the low temperature transport anomaly, we calculate the minimum energy of the upper band at the X point, E_b, using the band structure from photoemission and the hybridization amplitude as well as the f band energy we measure in this work. The result of such calculations is shown in Figure 5.3c. The minimum of the upper band drops as a result of decreasing hybridization amplitude v. It is interesting to note even though the hybridization amplitude is non-zero at temperatures around 50 K, the minimum of the upper band approaches the Fermi level at around 50 K (illustrated in Figure 5.7). Thus the hybridization gap does not span the Fermi level at intermediate temperatures above the metal-insulator transition even though the hybridization amplitude v is non-zero. The change in resistivity, magnetic susceptibility and the Hall coefficient change at $\sim$ 50 K can be easily interpreted as a consequence of the change of Fermi surface due to shrinking of hybridization amplitude. The shift of the upper band minimum has also been reported in photoemission on the 1×1 surface[86,29].

More generally, on all surfaces the STM-measured dI/dV spectra consistently show a dominant

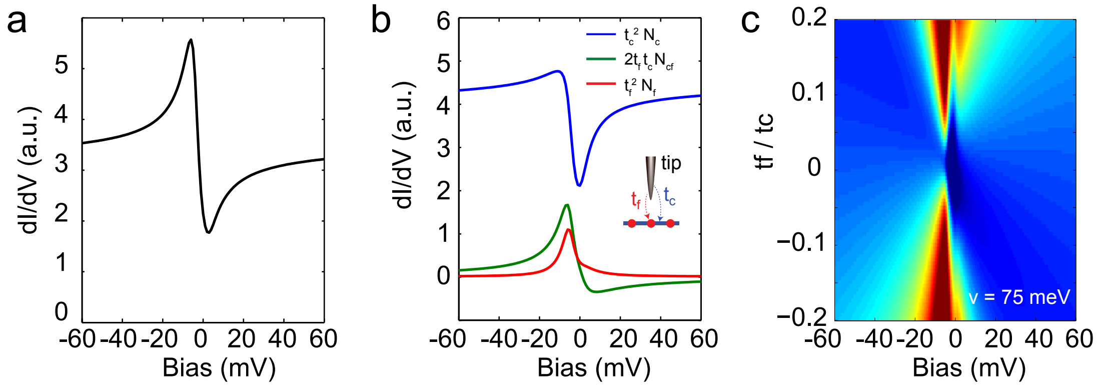

Figure 5.6: Decomposition of the measured tunneling conductance into DOS and interference channels. a Simulation of dI/dV on the 2×1 surface using a two-channel tunneling model. The conduction band was modeled as an ellipsoid centered at the X point in the three-dimensional Brillouin zone shown in the inset, and the hybridized f band was approximated as dispersionless. (hybridized f band energy $E_f = -3.5\ meV$, hybridization amplitude $v = 90\ meV$, and tunneling ratio $t_f/t_c = -0.023$. **b** Scaled contributions to dI/dV from the conduction band (blue), f band (red), and interference (green).

peak on the filled state side, in accordance with the bare hybridized DOS $N_c(V)$ and $N_f(V)$ expected for an electron-like $5d$ conduction band[76,3,87,134,60,89,38,143,113]. This contrasts with PTS/PCS measurements, which show a dominant peak in dI/dV on the empty state side[7,140]. To understand this contrast, we note that dI/dV depends on $N_c(V)$ and $N_f(V)$, which are intrinsic properties of the SmB$_6$ surface, and on the ratio t_f/t_c, which is an extrinsic property of the tunnel junction. We compute the dependence of dI/dV on t_f/t_c in Figure 5.6c, and conclude that an empty state peak in dI/dV can arise only when $t_f/t_c > 0$. For this regime we find that $N_{cf}(V)$ dominates dI/dV and masks the bare DOS by adding a positive bias peak and suppressing the DOS at the Fermi level. The Fermi level dip in PTS/PCS data[7,140] may therefore represent an energy range of extrinsic destructive interference, and not necessarily the intrinsic hybridization gap. The relative prominence of the filled state peak in all our STM measurements demonstrates the consistent dominance of the bare DOS and the significance of the STM-observed spectral gap as representative of the true hybridization gap.

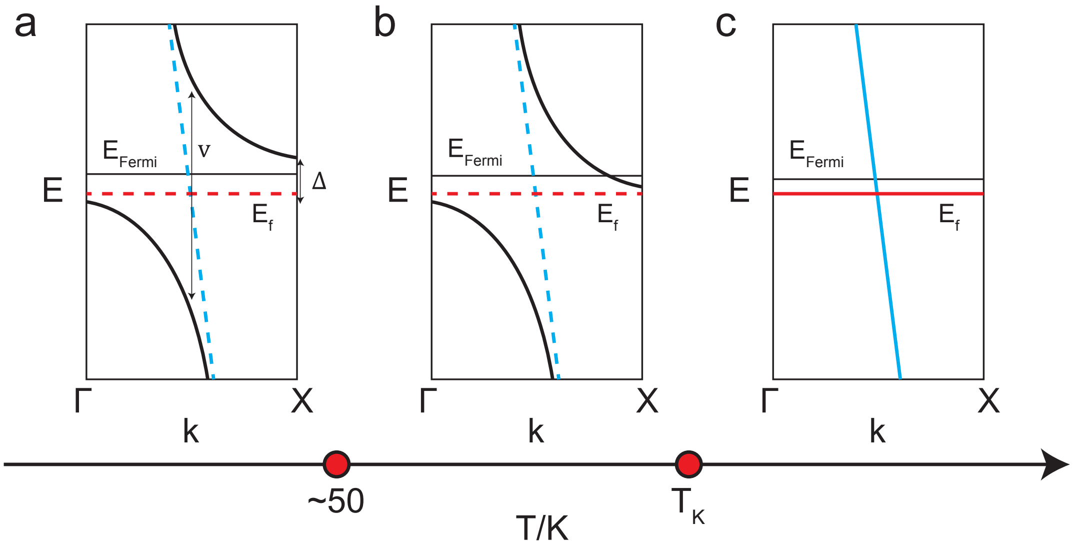

Figure 5.7: Schematic of band structure in different temperature. **a** Schematic of band structure in low temperature insulating state. The hybridization amplitude v and band gap Δ are illustrated with double arrows. The f-band and the conduction band before hybridization is shown in dash lines. **b** Schematic of band structure in low temperature conducting state, where the Fermi energy cut across the upper hybridization band. **c** Schematic of band structure without hybridization.

Our spatially resolved STM measurements of distinct electronic structure on the several surface morphologies of SmB$_6$ are consistent with existing ARPES measurements, and can reconcile some apparent discrepancies between them[87,134,60,89,113,38,143,29]. We expect that most ARPES experiments, with typical $\sim$hundred-micron spot size, will show momentum-resolved contributions from both the Sm-terminated 1×1 and 2×1 morphologies (Figs. 5.2a-b), and possibly the top few layers of the bulk, but not from the two disordered morphologies where k is a poor quantum number. Depending on the fractional composition of the cleaved surface structure, as well as the photon energy, depth probed, and detector resolution, ARPES may observe the spatial average of the -28 meV and -8 meV hybridized f bands from the two Sm-terminated surfaces as a single dispersing[29] or broadened f band at intermediate energy[134,60,143,113], or as one[38] or two[87,89] separate states. In the latter scenario, the -8 meV hybridized f band has been interpreted as an 'in-gap' state[87,89]. However, we note that a topological in-gap state would be expected to span the upper and lower hybridized bands, and thus would appear as continuous spectral weight filling the hybridization gap, rather than as a sharp peak at a specific energy. Indeed, we consistently observe broad in-gap spectral weight on all surfaces.

With these first atomically resolved spectroscopic measurements on SmB$_6$, we provide a general new paradigm for interpreting Kondo hybridization, and lay the groundwork for understanding TKIs. First, our explicit decomposition of the measured tunneling conductance into intrinsic DOS vs. extrinsic interference channels provides an intuitive way to understand tunneling measurements of Kondo hybridization in a broad class of heavy fermion materials[109,33,97,11,140]. Second, we confirm that SmB$_6$ is a Kondo insulator, by using this decomposition to reveal the full f band hybridization gap, spanning the Fermi level, on all four observed surface morphologies. Finally, our temperature dependent spectroscopy on the nonpolar 2×1 surface points to the hybridization gap first crossing the Fermi level around $T^* \sim 50$ K, in agreement with previous bulk measurements.

Our observation of the hybridized f band shifts between polar and non-polar cleaved surfaces of

SmB_6 reveals the dramatically different electronic environments in which the predicted topological surface state must exist. Theoretical modeling of bulk band shifts, surface states, and hybridization for different surface terminations is urgently needed. Our work provides the nanoscale spectroscopic details necessary for understanding the first strongly correlated topological insulator.

5.4 Possible Quasiparticle interference in SmB_6

Multiple theoretical predictions have been made on quasiparticle interference in SmB_6 [138,15]. Most of these theoretical predictions have been made on the 1×1 surface of Sm or B. However, there are no reports of QPI in SmB_6, regardless of surface termination. One of the reasons, as discussed in the previous section, might be the absence of large flat 1×1 surface. On the other hand, a topologically trivial surface state has been reported in SmB_6 [143]. The existence of this type of surface states is polarity-driven.

In Figure 5.8, we show multiple energy layers of the dI/dV map on the 1×2 surface of nominally SmB_6 with a surface density of 0.4% defects. We choose the $1{\times}2$ surface for the reason that it is non-polar. We do not expect any polarity driven surface states on this surface. However, the 1×2 surface reconstruction complicates the 2D band structure and makes it difficult to interpret the observed QPI.

Dispersive features are observed in the $g(\vec{q}, E)$ maps shown in 5.8. The dispersive features are highlighted with red arrows. Several key features of these dispersive peaks are worth noticing. Firstly, the dispersive peaks are located in the same direction as the 1×2 structure peaks. We cannot observe obvious QPI-like features in other direction. Secondly, we have discovered that the dispersive feature between the central peak and the 1×2 structural peaks exists only at energies close to the Fermi level or the Kondo resonance peak (Figure 5.9). These facts strongly indicates that the dispersive feature we observed is related to Kondo hybridization and the Kondo gap.

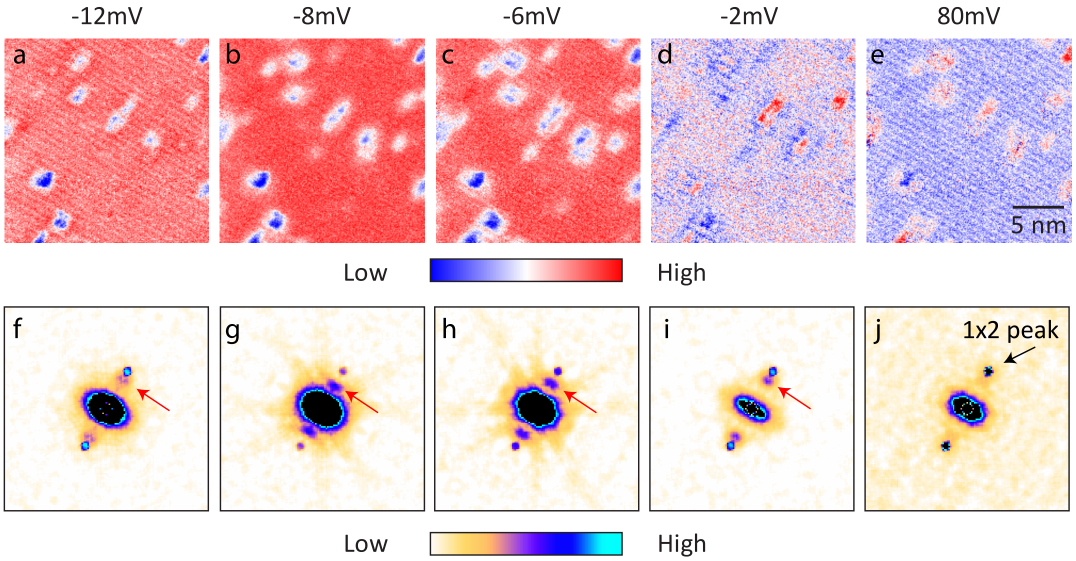

Figure 5.8: Energy dependence of possible QPI patterns in pristine SmB$_6$. **a-e** 20 nm by 20 nm real space dI/dV map in five different energies. Note that Kondo resonance peak locates at -8mV. **f-j** Fourier transform of the dI/dV maps in **a-e**. The 1×2 structural peak is highlighted with a black arrow in **j**. The dispersive feature is highlighted with red arrows.

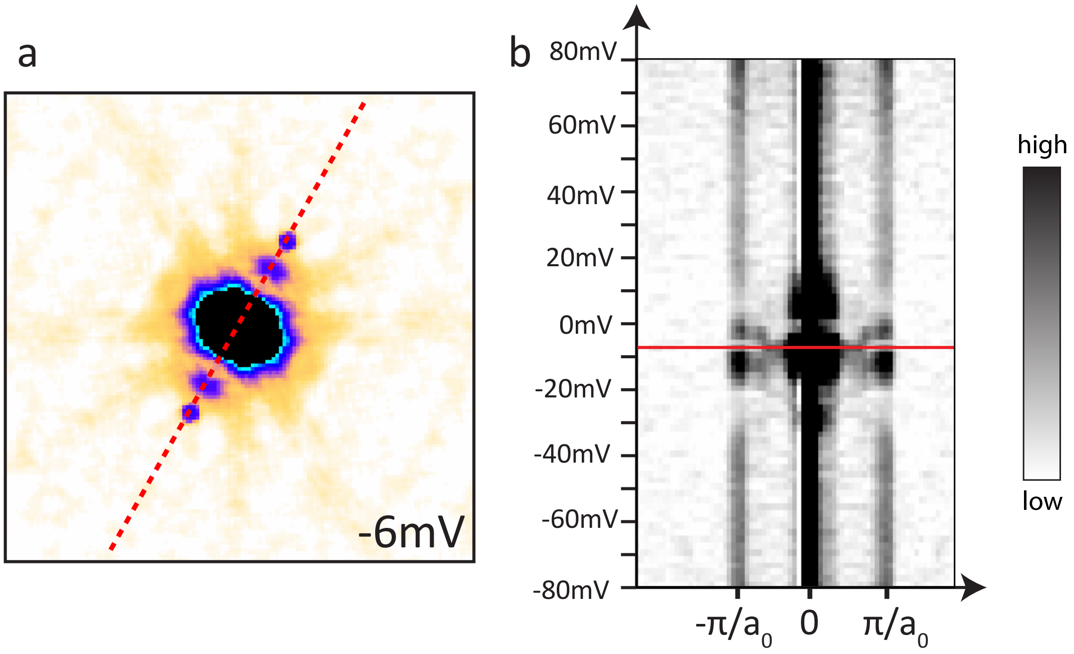

Figure 5.9: Linecut of QPI patterns in SmB$_6$. a QPI pattern in SmB$_6$ at -6mV. The red dashed line illustrates the linecut we make in **b**. **b** Linecut of the $g(q, E)$ in the direction of the 1×2 peaks. The linecut covers the range from -80 to 80 mV.

We also performed STM experiments on magnetic Gd-doped SmB_6. It has been reported that the magnetic Gd dopant would break time reversal symmetry and eliminate the topologically protected surface state[66]. The FT-STM experiment results are shown in Figure 5.10. It is surprising that we observe the dispersive features in the Gd-doped sample as well. There are different explanations that need to be tested before reaching a definitive conclusion. One of the possibilities is that the dispersive feature does not come from the topological surface state. As a result, one would not expect the feature to disappear when the Gd dopant are introduced in the system. The other explanation might be that Gd dopants form clusters in the sample. It is possible that our STM experiment is performed in a region with few Gd dopant where the topological surface state survives. The observed dopant concentration of our Gd-doped sample is around 0.5%, which is lower than the nominal doping level (3%). This explanation is supported by the fact that the spectra observed on Gd-SmB_6 and pristine SmB_6 are identical.

The energy dispersion of the QPI peaks is highlighted in the high resolution $g(\vec{q}, E)$ linecut in Figure 5.10. The dispersive QPI peaks span across the Fermi level and the Kondo hybridization gap that we discussed in the previous section. The slope of the feature (black dashed line in Figure 5.10) is small (7.6 meV·Å) indicating a slow band regardless of the details of the scattering process. However, most of the surface bands observed by ARPES experiments on 1×1 surface have a stiff energy dispersion relation. The reason for the fast surface band observed on the 1×1 surface might be related to surface Kondo breakdown as suggested in the a recent paper by Alexandrow *et al.*[2].

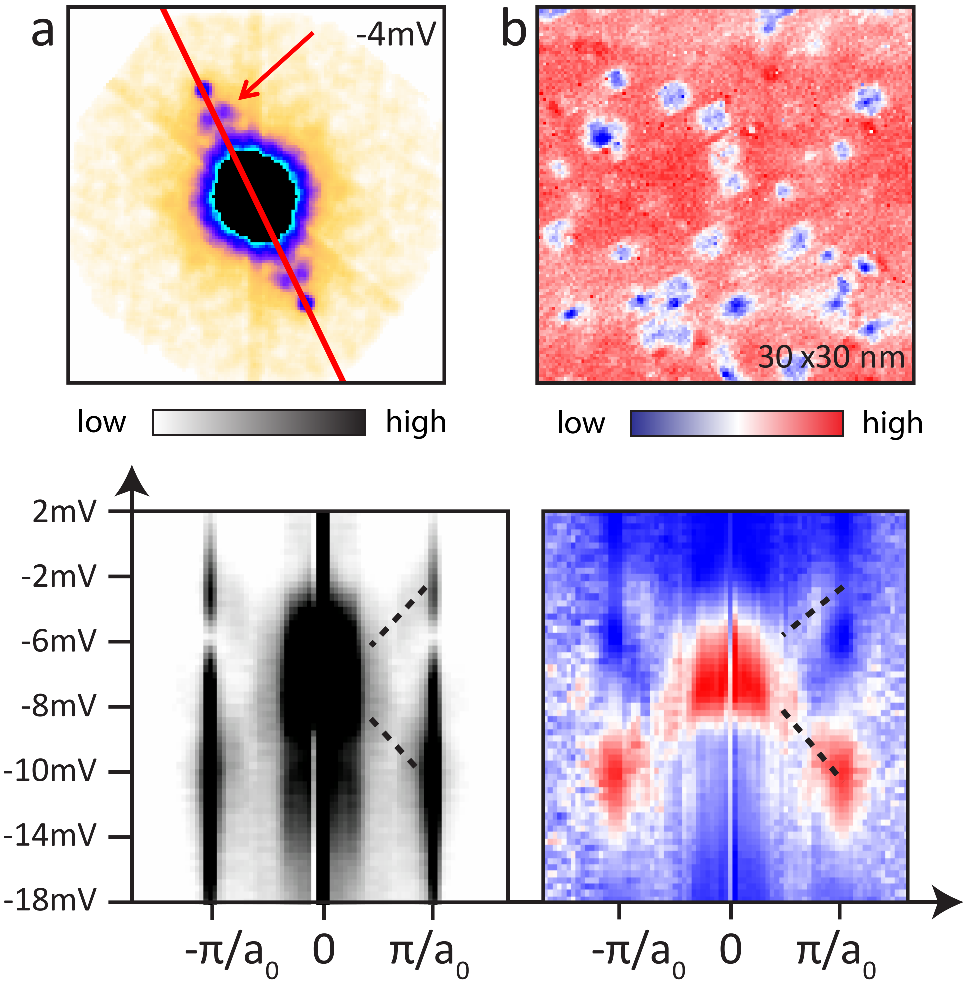

Figure 5.10: Energy dependence of possible QPI patterns in Gd doped SmB$_6$. **a** $g(q, E)$ at -4mV inside the Kondo insulating gap. **b** dI/dV map $g(r, E)$ on the 1×2 surface of Gd doped SmB$_6$ sample in a 30 by 30 nm area at -4 mV. **c**. Linecut of $g(q, E)$ in the direction of the 1×2 structural modulation. The dispersive peak is marked using black dashed lines. **d** The same plot as **c** except for normalizing each column to a constant to emphasize the dispersive feature. The QPI peaks are marked with black dash lines.

References

[1] Alekseev, P., Mignot, J.-M., Rossat-Mignod, J., Lazukov, V., & Sadikov, I. (1993). Magnetic excitations in SmB_6 single crystals. *Physica B*, 186-188, 384–386.

[2] Alexandrov, V., Coleman, P., & Erten, O. (2015). Kondo breakdown in topological kondo insulators. *Phys. Rev. Lett.*, 114, 177202.

[3] Alexandrov, V., Dzero, M., & Coleman, P. (2013). Cubic topological Kondo insulators. *Physical Review Letters*, 111, 226403.

[4] Allais, A., Chowdhury, D., & Sachdev, S. (2014). Connecting high-field quantum oscillations to the pseudogap in the underdoped cuprates. *Nature communications*, 5(5771).

[5] Alldredge, J. W., Lee, J., McElroy, K., Wang, M., Fujita, K., Kohsaka, Y., Taylor, C., Eisaki, H., Uchida, S., Hirschfeld, P. J., & Davis, J. C. (2008). Evolution of the electronic excitation spectrum with strongly diminishing hole density in superconducting $Bi_2Sr_2CaCu_2O_{8+\delta}$. *Nature Physics*, 4(4), 319–326.

[6] Allen, J., Batlogg, B., & Wachter, P. (1979). Large low-temperature Hall effect and resistivity in mixed-valent SmB_6. *Physical Review B*, 20(12), 4807–4813.

[7] Amsler, B., Fisk, Z., Sarrao, J., von Molnar, S., Meisel, M., & Sharifi, F. (1998). Electron-tunneling studies of the hexaboride materials SmB_6, EuB_6, CeB_6, and SrB_6. *Physical Review B*, 57(15), 8747–8750.

[8] Ando, Y. (2013). Topological insulator materials. *Journal of the Physical Society of Japan*, 82, 102001.

[9] Ando, Y., Hanaki, Y., Ono, S., Murayama, T., Segawa, K., Miyamoto, N., & Komiya, S. (2000). Carrier concentrations in $Bi_2Sr_{2-z}La_zCuO_{6+\delta}$ single crystals and their relation to Hall coefficient and thermopower. *Physical Review B*, 61(22), 4.

[10] Aono, M., Nishitani, R., Oshima, C., Tanaka, T., Bannai, E., & Kawai, S. (1979). LaB_6 and SmB_6(001) surfaces studied by angle-resolved XPS, LEED and ISS. *Surface Science*, 86, 631–637.

[11] Aynajian, P., da Silva Neto, E. H., Gyenis, A., Baumbach, R. E., Thompson, J. D., Fisk, Z., Bauer, E. D., & Yazdani, A. (2012). Visualizing heavy fermions emerging in a quantum critical Kondo lattice. *Nature*, 486(7402), 201–6.

[12] Balakirev, F. F., Betts, J. B., Migliori, A., Ono, S., Ando, Y., & Boebinger, G. S. (2003). Signature of optimal doping in Hall-effect measurements on a high-temperature superconductor. *Nature*, 424(August), 912–915.

[13] Bardeen, J. (1961). Tunnelling from a many-particle point of view. *Physical Review Letters*, 6(2), 57–59.

[14] Bardeen, J., Cooper, L. N., & Schrieffer, J. R. (1957). *Phys. Rev.*, 108.

[15] Baruselli, P. P. & Vojta, M. (2014). Scanning tunneling spectroscopy and surface quasiparticle interference in models for the strongly correlated topological insulators smb$_6$ and pub$_6$. *Phys. Rev. B*, 90, 201106.

[16] Bednorz, J. & Muller, K. (1986). Possible high t$_c$ superconductivity in the ba–la–cu–o system. *Zeitschrift fur Physik B Condensed Matter*, 64(2), 189–193.

[17] Benlagra, A., Pruschke, T., & Vojta, M. (2011). Finite-temperature spectra and quasiparticle interference in Kondo lattices: From light electrons to coherent heavy quasiparticles. *Physical Review B*, 84(19), 195141.

[18] Boyer, M. C., Wise, W. D., Chatterjee, K., Yi, M., Kondo, T., Takeuchi, T., Ikuta, H., & Hudson, E. W. (2007). Imaging the two gaps of the high-temperature superconductor $Bi_2Sr_2CuO_{6+x}$. *Nature Physics*, 3(11), 802–806.

[19] Caldwell, T., Reyes, A., Moulton, W., Kuhns, P., Hoch, M., Schlottmann, P., & Fisk, Z. (2007). High-field suppression of in-gap states in the Kondo insulator SmB$_6$. *Physical Review B*, 75(7), 075106.

[20] Chang, J., Blackburn, E., Holmes, A. T., Christensen, N. B., Larsen, J., Mesot, J., Liang, R., Bonn, D. A., Hardy, W. N., Watenphul, A., Zimmermann, M. v., Forgan, E. M., & Hayden, S. M. (2012a). Direct observation of competition between superconductivity and charge density wave order in YBa2Cu3O6.67.

[21] Chang, J., Blackburn, E., Holmes, A. T., Christensen, N. B., Larsen, J., Mesot, J., Liang, R., Bonn, D. a., Hardy, W. N., Watenphul, A., Zimmermann, M. V., Forgan, E. M., & Hayden, S. M. (2012b). Direct observation of competition between superconductivity and charge density wave order in YBa2Cu3O6.67. *Nature Physics*, 8(12), 871–876.

[22] Chatterjee, U., Shi, M., Kaminski, a., Kanigel, a., Fretwell, H., Terashima, K., Takahashi, T., Rosenkranz, S., Li, Z., Raffy, H., Santander-Syro, a., Kadowaki, K., Norman, M., Randeria,

M., & Campuzano, J. (2006). Nondispersive Fermi Arcs and the Absence of Charge Ordering in the Pseudogap Phase of $Bi_2Sr_2CaCu_2O_{8+\delta}$. *Physical Review Letters*, 96(10), 107006.

[23] Coleman, P. (2007). Heavy fermions: Electrons at the edge of magnetism. *Handbook of Magnetism and Advanced Magnetic Materials*.

[24] Comin, R., Frano, A., Yee, M. M., Yoshida, Y., Eisaki, H., Schierle, E., Weschke, E., Sutarto, R., He, F., Soumyanarayanan, A., He, Y., Le Tacon, M., Elfimov, I. S., Hoffman, J. E., Sawatzky, G. A., Keimer, B., & Damascelli, A. (2014a). Charge order driven by fermi-arc instability in bi2sr2−xlaxcuo6+δ. *Science*, 343(6169), 390–392.

[25] Comin, R., Sutarto, R., He, F., da Silva Neto, E., Chauviere, L., Frano, A., Liang, R., Hardy, W. N., Bonn, D., Yoshida, Y., Eisaki, H., Hoffman, J. E., Keimer, B., Sawatzky, G. A., & Damascelli, A. (2014b). The symmetry of charge order in cuprates. *arXiv*, 1402(1402), 5415.

[26] Cooley, J., Aronson, M., Fisk, Z., & Canfield, P. (1995). SmB_6: Kondo insulator or exotic metal? *Physical Review Letters*, 74(9), 1629–1632.

[27] da Silva Neto, E. H., Aynajian, P., Frano, A., Comin, R., Schierle, E., Weschke, E., Gyenis, A., Wen, J., Schneeloch, J., Xu, Z., Ono, S., Gu, G., Le Tacon, M., & Yazdani, A. (2014). Ubiquitous interplay between charge ordering and high-temperature superconductivity in cuprates. *Science*, 343(6169), 393–396.

[28] Davis, J. C. S. & Lee, D.-H. (2013). Concepts relating magnetic interactions, intertwined electronic orders, and strongly correlated superconductivity. *Proceedings of the National Academy of Sciences*, 110(44), 17623–17630.

[29] Denlinger, J. D., Allen, J. W., Kang, J. S., Sun, K., Kim, J. W., Shim, J. H., Min, B. I., Kim, D.-J., & Fisk, Z. (2013). Temperature dependence of linked gap and surface state evolution in the mixed valent topological insulator SmB_6. *Arxiv Preprint*, (pp. 1312.6637).

[30] Doiron-Leyraud, N., Proust, C., LeBoeuf, D., Levallois, J., Bonnemaison, J.-B., Liang, R., Bonn, D. A., Hardy, W. N., & Taillefer, L. (2007). Quantum oscillations and the Fermi surface in an underdoped high-Tc superconductor. *Nature*, 447(7144), 565–8.

[31] Dzero, M., Sun, K., Galitski, V., & Coleman, P. (2010). Topological Kondo insulators. *Physical Review Letters*, 104(10), 106408.

[32] Efetov, K. B., Meier, H., & Pépin, C. (2013). Pseudogap state near a quantum critical point. *Nature Physics*, 9(7), 442–446.

[33] Ernst, S., Kirchner, S., Krellner, C., Geibel, C., Zwicknagl, G., Steglich, F., & Wirth, S. (2011). Emerging local Kondo screening and spatial coherence in the heavy-fermion metal $YbRh_2Si_2$. *Nature*, 474(7351), 362–6.

[34] Feng, D. L., Lu, D. H., Shen, K. M., Kim, C., Eisaki, H., Damascelli, A., Yoshizaki, R., Shimoyama, J. i., Kishio, K., Gu, G. D., Oh, S., Andrus, A., O'Donnell, J., Eckstein, J. N., & Shen, Z. X. (2000). Signature of Superfluid Density in the Single-Particle Excitation Spectrum of $Bi_2Sr_2CaCu_2O_{8+delta}$. *Science*, 289(5477), 14.

[35] Figgins, J. & Morr, D. K. (2010). Differential conductance and quantum interference in Kondo systems. *Physical Review Letters*, 104(18), 187202.

[36] Flachbart, K., Gloos, K., Konovalova, E., Paderno, Y., Reiffers, M., Samuely, P., & Švec, P. (2001). Energy gap of intermediate-valent $\mathrm{SmB_6}$ studied by point-contact spectroscopy. *Physical Review B*, 64(8), 085104.

[37] Fradkin, E. & Kivelson, S. a. (2012). High-temperature superconductivity: Ineluctable complexity. *Nature Physics*, 8(12), 864–866.

[38] Frantzeskakis, E., de Jong, N., Zwartsenberg, B., Huang, Y., Pan, Y., Zhang, X., Zhang, J., Zhang, F., Bao, L., Tegus, O., Varykhalov, A., de Visser, A., & Golden, M. (2013). Kondo hybridization and the origin of metallic states at the (001) surface of $\mathrm{SmB_6}$. *Physical Review X*, 3, 041024.

[39] Fu, L., Kane, C., & Mele, E. (2007). Topological insulators in three dimensions. *Physical Review Letters*, 98(10), 106803.

[40] Fujita, K., Hamidian, M. H., Edkins, S. D., Kim, C. K., Kohsaka, Y., Azuma, M., Takano, M., Takagi, H., Eisaki, H., Uchida, S.-i., Allais, A., Lawler, M. J., Kim, E.-A., Sachdev, S., & Davis, J. C. S. (2014a). Direct phase-sensitive identification of a d-form factor density wave in underdoped cuprates. *Proceedings of the National Academy of Sciences*, 111(30), E3026–E3032.

[41] Fujita, K., Kim, C. K., Lee, I., Lee, J., Hamidian, M. H., Firmo, I. A., Mukhopadhyay, S., Eisaki, H., Uchida, S., Lawler, M. J., Kim, E.-A., & Davis, J. C. (2014b). Simultaneous transitions in cuprate momentum-space topology and electronic symmetry breaking. *Science*, 344(6184), 612–616.

[42] Gao, M., Ma, F., Lu, Z.-Y., & Xiang, T. (2010). Surface structures of ternary iron arsenides $A\mathrm{Fe_2As_2}$ (A=Ba, Sr, or Ca). *Physical Review B*, 81(19), 193409.

[43] Ghiringhelli, G., Le Tacon, M., Minola, M., Blanco-Canosa, S., Mazzoli, C., Brookes, N. B., De Luca, G. M., Frano, A., Hawthorn, D. G., He, F., Loew, T., Sala, M. M., Peets, D. C., Salluzzo, M., Schierle, E., Sutarto, R., Sawatzky, G. A., Weschke, E., Keimer, B., & Braicovich, L. (2012). Long-range incommensurate charge fluctuations in (y,nd)ba2cu3o6+x. *Science*, 337(6096), 821–825.

[44] Giaever, I. (1960). Energy gap in superconductors measured by electron tunneling. *Phys. Rev. Lett.*, 5, 147–148.

[45] Gorshunov, B., Sluchanko, N., Volkov, A., Dressel, M., Knebel, G., Loidl, A., & Kunii, S. (1999). Low-energy electrodynamics of SmB_6. *Physical Review B*, 59(3), 1808–1814.

[46] Güntherodt, G., Thompson, W., Holtzberg, F., & Fisk, Z. (1982). Electron tunneling into intermediate-valence materials. *Physical Review Letters*, 49, 1030–1033.

[47] Hanaguri, T., Kohsaka, Y., Davis, J. C., Lupien, C., Yamada, I., Azuma, M., Takano, M., Ohishi, K., Ono, M., & Takagi, H. (2007). Quasiparticle interference and superconducting gap in Ca2−xNaxCuO2Cl2. *Nature Physics*, 3(12), 865–871.

[48] Hanaguri, T., Kohsaka, Y., Ono, M., Maltseva, M., Coleman, P., Yamada, I., Azuma, M., Takano, M., Ohishi, K., & Takagi, H. (2009). Coherence factors in a high-tc cuprate probed by quasi-particle scattering off vortices. *Science (New York, N.Y.)*, 323(5916), 923–926.

[49] Harrison, N. & Sebastian, S. E. (2012). Fermi surface reconstruction from bilayer charge ordering in the underdoped high temperature superconductor yba 2 cu 3 o 6+ x. *New Journal of Physics*, 14(9), 095023.

[50] Harrison, N. & Sebastian, S. E. (2014). On the relationship between charge ordering and the Fermi arcs observed in underdoped high Tc superconductors. *Arxiv Preprint*, (pp. 1401.6590).

[51] Hasan, M. Z. & Kane, C. L. (2010). *Colloquium* : Topological insulators. *Rev. Mod. Phys.*, 82, 3045–3067.

[52] Hasan, M. Z. & Moore, J. E. (2011). Three-dimensional topological insulators. *Annual Review of Condensed Matter Physics*, 2(1), 55–78.

[53] Hashimoto, M., Nowadnick, E. a., He, R.-h., Vishik, I. M., Moritz, B., He, Y., Tanaka, K., Moore, R. G., Lu, D., Yoshida, Y., Ishikado, M., Sasagawa, T., Fujita, K., Ishida, S., Uchida, S., Eisaki, H., Hussain, Z., Devereaux, T. P., & Shen, Z.-X. (2014). Direct spectroscopic evidence for phase competition between the pseudogap and superconductivity in $Bi_2Sr_2CaCuO_{6+\delta}$. *Nature Materials*, 14(January), 37.

[54] He, R.-h., Hashimoto, M., Karapetyan, H., Koralek, J. D., Hinton, J. P., Testaud, J. P., Nathan, V., Yoshida, Y., Yao, H., Tanaka, K., Meevasana, W., Moore, R. G., Lu, D. H., Mo, S.-K., Ishikado, M., Eisaki, H., Hussain, Z., Devereaux, T. P., Kivelson, S. A., Orenstein, J., Kapitulnik, A., & Shen, Z.-X. (2011). From a single-band metal to a high-temperature superconductor via two thermal phase transitions. *Science (New York, N.Y.)*, 331(6024), 1579–83.

[55] He, Y., Yin, Y., Zech, M., Soumyanarayanan, A., Yee, M. M., Williams, T., Boyer, M. C., Chatterjee, K., Wise, W. D., Zeljkovic, I., Kondo, T., Takeuchi, T., Ikuta, H., Mistark, P., Markiewicz, R. S., Bansil, A., Sachdev, S., Hudson, E. W., & Hoffman, J. E. (2014). Fermi surface and pseudogap evolution in a cuprate superconductor. *Science*, 344(6184), 608–611.

[56] Hoffman, J. E., Hudson, E. W., Lang, K. M., Madhavan, V., Eisaki, H., Uchida, S., & Davis, J. C. (2002). A four unit cell periodic pattern of quasi-particle states surrounding vortex cores in $Bi_2Sr_2CaCu_2O_{8+delta}$. *Science (New York, N.Y.)*, 295(5554), 466–469.

[57] Howald, C., Eisaki, H., Kaneko, N., & Kapitulnik, A. (2003). Coexistence of periodic modulation of quasiparticle states and superconductivity in Bi2Sr2CaCu2O8+d. *Proceedings of the National Academy of Sciences of the United States of America*, 100(17), 9705–9.

[58] Hsieh, D., Xia, Y., Qian, D., Wray, L., Dil, J. H., Meier, F., Osterwalder, J., Patthey, L., Checkelsky, J. G., Ong, N. P., Fedorov, A. V., Lin, H., Bansil, A., Grauer, D., Hor, Y. S., Cava, R. J., & Hasan, M. Z. (2009). A tunable topological insulator in the spin helical Dirac transport regime. *Nature*, 460(August), 1101–1105.

[59] Jia, X., Goswami, P., & Chakravarty, S. (2009). Resolution of two apparent paradoxes concerning quantum oscillations in underdoped high-Tc superconductors. *Physical Review B*, 80(13), 134503.

[60] Jiang, J., Li, S., Zhang, T., Sun, Z., Chen, F., Ye, Z. R., Xu, M., Ge, Q. Q., Tan, S. Y., Niu, X. H., Xia, M., Xie, B. P., Li, Y. F., Chen, X. H., Wen, H. H., & Feng, D. L. (2013). Observation of possible topological in-gap surface states in the Kondo insulator SmB_6 by photoemission. *Nature Communications*, 4, 3010.

[61] Kaminski, A., Rosenkranz, S., Fretwell, H. M., Campuzano, J. C., Li, Z., Raffy, H., Cullen, W. G., You, H., Olson, C. G., Varma, C. M., & Höchst, H. (2002). Spontaneous breaking of time-reversal symmetry in the pseudogap state of a high-Tc superconductor. *Nature*, 416(April), 610–613.

[62] Kane, C. L. & Mele, E. J. (2005). Quantum spin hall effect in graphene. *Phys. Rev. Lett.*, 95, 226801.

[63] Kerimer, B., Kivelson, S. A., Norman, M. R., Uchida, S., & Zaanen, J. (2015). *nature*, 518.

[64] Kim, D. J., Thomas, S., Grant, T., Botimer, J., Fisk, Z., & Xia, J. (2013). Surface Hall effect and nonlocal transport in SmB_6: Evidence for surface conduction. *Scientific reports*, 3, 3150.

[65] Kim, D. J., Xia, J., & Fisk, Z. (2014a). Topological surface state in the Kondo insulator samarium hexaboride. *Nature Materials*.

[66] Kim, D. J., Xia, J., & Fisk, Z. (2014b). Topological surface state in the Kondo insulator samarium hexaboride. *Nature materials*, 13(5), 466–70.

[67] Kohsaka, Y., Taylor, C., Wahl, P., Schmidt, a., Lee, J., Fujita, K., Alldredge, J. W., McElroy, K., Lee, J., Eisaki, H., Uchida, S., Lee, D.-H., & Davis, J. C. (2008). How Cooper pairs vanish approaching the Mott insulator in Bi2Sr2CaCu2O8+delta. *Nature*, 454(7208), 1072–8.

[68] Kondo, T., Hamaya, Y., Palczewski, A. D., Takeuchi, T., Wen, J. S., Xu, Z. J., Gu, G., Schmalian, J., & Kaminski, A. (2010). Disentangling Cooper-pair formation above Tc from the pseudogap state in the cuprates. *Nature Physics*, 7(1), 9.

[69] Kondo, T., Khasanov, R., Takeuchi, T., Schmalian, J., & Kaminski, A. (2009). Competition between the pseudogap and superconductivity in the high-T(c) copper oxides. *Nature*, 457(7227), 296–300.

[70] Laliberte, F., Doiron-leyraud, N., Daou, R., Chang, J., Leboeuf, D., Cyr-choinie, O., Ramshaw, B. J., Liang, R., Bonn, D. a., Hardy, W. N., & Taillefer, L. (2010). Broken rotational symmetry in the pseudogap phase of a high-T c superconductor. *Nature*, 463(January), 519–522.

[71] Lawler, M., Fujita, K., Lee, J., Schmidt, A. R., Kohsaka, Y., Kim, C. K., Eisaki, H., Uchida, S., Davis, J. C., Sethna, J. P., & Kim, E.-A. (2010a). Intra-unit-cell electronic nematicity of the high-T(c) copper-oxide pseudogap states. *Nature*, 466(7304), 347–51.

[72] Lawler, M. J., Fujita, K., Lee, J., Schmidt, A. R., Kohsaka, Y., Kim, C. K., Eisaki, H., Uchida, S., Davis, J. C., Sethna, J. P., & Kim, E.-A. (2010b). Intra-unit-cell electronic nematicity of the high-T(c) copper-oxide pseudogap states. *Nature*, 466(7304), 347–351.

[73] LeBoeuf, D., Doiron-Leyraud, N., Vignolle, B., Sutherland, M., Ramshaw, B. J., Levallois, J., Daou, R., Laliberté, F., Cyr-Choinière, O., Chang, J., Jo, Y. J., Balicas, L., Liang, R., Bonn, D. A., Hardy, W. N., Proust, C., & Taillefer, L. (2011). Lifshitz critical point in the cuprate superconductor YBa_{2}Cu_{3}O_{y} from high-field Hall effect measurements. *Physical Review B*, 83(5), 054506.

[74] Li, G., Xiang, Z., Yu, F., Asaba, T., Lawson, B., Cai, P., Tinsman, C., Berkley, A., Wolgast, S., Eo, Y. S. S., Kim, D.-J., Kurdak, C., Allen, J. W. W., Sun, K., Chen, X. H. H., Wang, Y. Y. Y., Fisk, Z., & Li, L. (2014). Two-dimensional Fermi surfaces in Kondo insulator SmB_6. *Science*, 346, 1208.

[75] Li, Y., Balédent, V., Barisić, N., Cho, Y., Fauqué, B., Sidis, Y., Yu, G., Zhao, X., Bourges, P., & Greven, M. (2008). Unusual magnetic order in the pseudogap region of the superconductor $HgBa_2CuO_{4+\delta}$. *Nature*, 455(7211), 372–5.

[76] Lu, F., Zhao, J., Weng, H., Fang, Z., & Dai, X. (2013). Correlated topological insulators with mixed valence. *Physical Review Letters*, 110(9), 096401.

[77] Ma, J. H., Pan, Z. H., Niestemski, F. C., Neupane, M., Xu, Y. M., Richard, P., Nakayama, K., Sato, T., Takahashi, T., Luo, H. Q., Fang, L., Wen, H. H., Wang, Z., Ding, H., & Madhavan, V. (2008). Coexistence of competing orders with two energy gaps in real and momentum space in the high temperature superconductor $Bi_2Sr_{2-x}La_xCuO_{6+\delta}$. *Physical Review Letters*, 101(20), 207002.

[78] Madhavan, V., Chen, W., Jamneala, T., Crommie, M. F., & Wingreen, N. S. (1998). Tunneling into a single magnetic atom: Spectroscopic evidence of the Kondo resonance. *Science*, 280(5363), 567–569.

[79] Maeda, H., Tanaka, Y., Fukutomi, M., & Asano, T. (1988). A new high- t c oxide superconductor without a rare earth element. *Japanese Journal of Applied Physics*, 27(2A), L209.

[80] Maltseva, M., Dzero, M., & Coleman, P. (2009). Electron cotunneling into a Kondo lattice. *Physical Review Letters*, 103(20), 206402.

[81] McElroy, K., Gweon, G.-H., Zhou, S., Graf, J., Uchida, S., Eisaki, H., Takagi, H., Sasagawa, T., Lee, D.-H., & Lanzara, a. (2006). Elastic Scattering Susceptibility of the High Temperature Superconductor $Bi_2Sr_2CaCu_2O_{8+\delta}$: A Comparison between Real and Momentum Space Photoemission Spectroscopies. *Physical Review Letters*, 96(6), 067005.

[82] McElroy, K., Simmonds, R. W., Hoffman, J. E., Lee, D.-H., Orenstein, J., Eisaki, H., Uchida, S., & Davis, J. C. (2003a). Relating atomic-scale electronic phenomena to wave-like quasiparticle states in superconducting Bi2Sr2CaCu2O8+delta. *Nature*, 422(6932), 592–6.

[83] McElroy, K., Simmonds, R. W., Hoffman, J. E., Lee, D.-H., Orenstein, J., Eisaki, H., Uchida, S., & Davis, J. C. (2003b). Relating atomic-scale electronic phenomena to wave-like quasiparticle states in superconducting Bi2Sr2CaCu2O8+delta. *Nature*, 422(6932), 592–6.

[84] Menth, A., Buehler, E., & Geballe, T. (1969). Magnetic and semiconducting properties of SmB_6. *Physical Review Letters*, 22(7), 295–297.

[85] Mesaros, A., Fujita, K., Eisaki, H., Uchida, S., Davis, J. C., Sachdev, S., Zaanen, J., Lawler, M. J., & Kim, E.-A. (2011). Topological defects coupling smectic modulations to intra–unit-cell nematicity in cuprates. *Science*, 333(6041), 426–430.

[86] Min, C.-H., Lutz, P., Fiedler, S., Kang, B. Y., Cho, B. K., Kim, H.-D., Bentmann, H., & Reinert, F. (2014). Importance of charge fluctuations for the topological phase in SmB_6. *Physical Review Letters*, 112, 226402.

[87] Miyazaki, H., Hajiri, T., Ito, T., Kunii, S., & Kimura, S.-i. (2012). Momentum-dependent hybridization gap and dispersive in-gap state of the Kondo semiconductor SmB_6. *Physical Review B*, 86(7), 075105.

[88] Nakagawa, N., Hwang, H. Y., & Muller, D. A. (2006). Why some interfaces cannot be sharp. *Nature Materials*, 5(3), 204–209.

[89] Neupane, M., Alidoust, N., Xu, S.-Y., Kondo, T., Ishida, Y., Kim, D. J., Liu, C., Belopolski, I., Jo, Y. J., Chang, T.-R., Jeng, H.-T., Durakiewicz, T., Balicas, L., Lin, H., Bansil, A., Shin, S., Fisk, Z., & Hasan, M. Z. (2013). Surface electronic structure of the topological Kondo-insulator candidate correlated electron system SmB_6. *Nature communications*, 4, 2991.

[90] Nie, L., Tarjus, G., & Kivelson, S. A. (2013). Quenched disorder and vestigial nematicity in the pseudo-gap regime of the cuprates. (pp.39).

[91] Nie, L., Tarjus, G., & Kivelson, S. A. (2014). Quenched disorder and vestigial nematicity in the pseudogap regime of the cuprates. *Proceedings of the National Academy of Sciences*, 111(22), 7980–7985.

[92] Norman, M. R. (2010a). Fermi-surface reconstruction and the origin of high-temperature superconductivity. *Physics*, 3, 86.

[93] Norman, M. R. (2010b). Fermi-surface reconstruction and the origin of high-temperature superconductivity. *Physics*, 3, 86.

[94] Norman, M. R., Kanigel, A., Randeria, M., Chatterjee, U., & Campuzano, J. C. (2007). Modeling the fermi arc in underdoped cuprates. *Phys. Rev. B*, 76, 174501.

[95] Nyhus, P., Cooper, S., Fisk, Z., & Sarrao, J. (1995). Light scattering from gap excitations and bound states in SmB_6. *Physical Review B*, 52(20), R14308–R14311.

[96] Ozcomert, J. S. & Trenary, M. (1992). Atomically resolved surface structure of LaB_6(100). *Surface Science*, 265(1-3), L227–L232.

[97] Park, W. K., Tobash, P. H., Ronning, F., Bauer, E. D., Sarrao, J. L., Thompson, J. D., & Greene, L. H. (2012). Observation of the hybridization gap and Fano resonance in the Kondo lattice $\mathrm{URu}_2\mathrm{Si}_2$. *Physical Review Letters*, 108(24), 246403.

[98] Parker, C. V., Aynajian, P., Eduardo, H., Neto, S., Pushp, A., Ono, S., Wen, J., Xu, Z., Gu, G., & Yazdani, A. (2010a). Fluctuating stripes at the onset of the pseudogap in the high-Tc superconductor $Bi_2Sr_2CaCu_2O_{8+x}$. *Nature*, 468(7324), 677–680.

[99] Parker, C. V., Aynajian, P., Eduardo, H., Neto, S., Pushp, A., Ono, S., Wen, J., Xu, Z., Gu, G., & Yazdani, A. (2010b). Fluctuating stripes at the onset of the pseudogap in the high-Tc superconductor Bi2Sr2CaCu2O8+x. *Nature*, 468(7324), 677–680.

[100] Pereg-Barnea, T. & Franz, M. (2008). Magnetic-field dependence of quasiparticle interference peaks in a d-wave superconductor with weak disorder. *Physical Review B*, 78(2), 020509.

[101] Platé, M., Mottershead, J. D. F., Elfimov, I. S., Peets, D. C., Liang, R., Bonn, D. A., Hardy, W. N., Chiuzbaian, S., Falub, M., Shi, M., Patthey, L., & Damascelli, A. (2005). Fermi surface and quasiparticle excitations of overdoped $\mathrm{Tl}_2\mathrm{Ba}_2\mathrm{CuO}_{6+\delta}$. *Phys. Rev. Lett.*, 95, 077001.

[102] Punk, M. & Sachdev, S. (2012). Fermi surface reconstruction in hole-doped t-J models without long-range antiferromagnetic order. *Physical Review B*, 85(19), 195123.

[103] Qi, X.-L. & Zhang, S.-C. (2011). Topological insulators and superconductors. *Reviews of Modern Physics*, 83(4), 1057–1110.

[104] Röß ler, S., Jang, T.-h., Kim, D.-J., Tjeng, L. H., Fisk, Z., Steglich, F., & Wirth, S. (2014). Hybridization gap and Fano resonance in SmB_6. *Proceedings of the National Academy of Sciences of the United States of America*, 111, 4798–802.

[105] Ruan, W., Ye, C., Guo, M., Chen, F., Chen, X., Zhang, G.-M., & Wang, Y. (2014). Emergence of a coherent in-gap state in the SmB_6 Kondo insulator revealed by scanning tunneling spectroscopy. *Physical Review Letters*, 112, 136401.

[106] Sacépé, B., Dubouchet, T., Chapelier, C., Sanquer, M., Ovadia, M., Shahar, D., Feigel'man, M., & Ioffe, L. (2011). Localization of preformed Cooper pairs in disordered superconductors. *Nature Physics*, 7(3), 239–244.

[107] Sachdev, S. & La Placa, R. (2013). Bond Order in Two-Dimensional Metals with Antiferromagnetic Exchange Interactions. *Physical Review Letters*, 111(2), 027202.

[108] Sachdev, S. & La Placa, R. (2013). Bond order in two-dimensional metals with antiferromagnetic exchange interactions. *Phys. Rev. Lett.*, 111, 027202.

[109] Schmidt, A. R., Hamidian, M. H., Wahl, P., Meier, F., Balatsky, A. V., Garrett, J. D., Williams, T. J., Luke, G. M., & Davis, J. C. (2010). Imaging the Fano lattice to 'hidden order' transition in $\mathrm{URu}_2\mathrm{Si}_2$. *Nature*, 465(7298), 570–6.

[110] Sebastian, S. E., Harrison, N., Altarawneh, M. M., Mielke, C. H., Liang, R., Bonn, D. a., Hardy, W. N., & Lonzarich, G. G. (2010). Metal-insulator quantum critical point beneath the high Tc superconducting dome. *Proceedings of the National Academy of Sciences of the United States of America*, 107(14), 6175–9.

[111] Sebastian, S. E., Harrison, N., & Lonzarich, G. G. (2012). Towards resolution of the Fermi surface in underdoped high-Tc superconductors. *Reports on Progress in Physics*, 75(10), 102501.

[112] Shen, K. M., Ronning, F., Lu, D. H., Baumberger, F., Ingle, N. J. C., Lee, W. S., Meevasana, W., Kohsaka, Y., Azuma, M., Takano, M., Takagi, H., & Shen, Z.-X. (2005). Nodal quasiparticles and antinodal charge ordering in ca2-xnaxcuo2cl2. *Science*, 307(5711), 901–904.

[113] Suga, S., Sakamoto, K., Okuda, T., Miyamoto, K., Kuroda, K., Sekiyama, A., Yamaguchi, J., Fujiwara, H., Irizawa, A., Ito, T., Kimura, S., Balashov, T., Wulfhekel, W., Yeo, S., Iga, F., & Imada, S. (2014). Spin-polarized angle-resolved photoelectron spectroscopy of the so-predicted Kondo topological insulator SmB_6. *Journal of the Physical Society of Japan*, 83, 014705.

[114] Tabis, W., Li, Y., Le Tacon, M., Braicovich, L., Kreyssig, A., Minola, M., Dellea, G., Weschke, E., Veit, M., Ramazanoglu, M., Goldman, A., Schmitt, T., Ghiringhelli, G., Barisic, N., Chan, M. K., Dorow, C. J., Yu, G., Zhao, X., Keimer, B., & Greven, M. (2014). Charge order and its

connection with Fermi-liquid charge transport in a pristine high- T. *Nature communications*, 5, 5875.

[115] Takimoto, T. (2011). $\mathrm{SmB_6}$: A promising candidate for a topological insulator. *Journal of the Physical Society of Japan*, 80(12), 123710.

[116] Tallon, J., Loram, J., Williams, G., Cooper, J., Fisher, I., Johnson, J., Staines, M., & Bernhard, C. (1999). Critical Doping in Overdoped High-Tc Superconductors: a Quantum Critical Point? *physica status solidi (b)*, 215(1), 531–540.

[117] Tanaka, K., Lee, W. S., Lu, D. H., Fujimori, a., Fujii, T., Risdiana, Terasaki, I., Scalapino, D. J., Devereaux, T. P., Hussain, Z., & Shen, Z.-X. (2006). Distinct Fermi-momentum-dependent energy gaps in deeply underdoped Bi2212. *Science (New York, N.Y.)*, 314(5807), 1910–3.

[118] Thomas, S., Kim, D. J., Chung, S. B., Grant, T., Fisk, Z., & Xia, J. (2013). Weak antilocalization and linear magnetoresistance in the surface state of $\mathrm{SmB_6}$. *Arxiv Preprint*, (pp. 1307.4133).

[119] Thouless, D. J., Kohmoto, M., Nightingale, M. P., & den Nijs, M. (1982). Quantized hall conductance in a two-dimensional periodic potential. *Phys. Rev. Lett.*, 49, 405–408.

[120] Timusk, T. & Statt, B. (1999). The pseudogap in high-temperature superconductors: an experimental survey. *Reports on Progress in Physics*, 62(1), 61.

[121] Tranquada, J., Sternlieb, B., Axe, J., Nakamura, Y., & Uchida, S. (1995a). Evidence for stripe correlations of spins and holes in copper oxide superconductors. *Nature*, 375, 561.

[122] Tranquada, J. M., Sternlieb, B. J., Axe, J. D., Nakamura, Y., & Uchida, S. (1995b). Evidence for stripe correlations of spins and holes in copper oxide superconductors. *Nature*, 375(6532), 561–563.

[123] Travaglini, G. & Wachter, P. (1984). Intermediate-valent $\mathrm{SmB_6}$ and the hybridization model: An optical study. *Physical Review B*, 29(2), 893–898.

[124] Vignolle, B., Carrington, A., Cooper, R. A., French, M. M. J., Mackenzie, A. P., Jaudet, C., Vignolles, D., Proust, C., & Hussey, N. E. (2008). Quantum oscillations in an overdoped high-Tc superconductor. *Nature*, 455(7215), 952–955.

[125] Vishik, I. M., Hashimoto, M., He, R.-H., Lee, W.-S., Schmitt, F., Lu, D., Moore, R. G., Zhang, C., Meevasana, W., Sasagawa, T., Uchida, S., Fujita, K., Ishida, S., Ishikado, M., Yoshida, Y., Eisaki, H., Hussain, Z., Devereaux, T. P., & Shen, Z.-X. (2012a). Phase competition in trisected superconducting dome. *Proceedings of the National Academy of Sciences of the United States of America*, 109(45), 18332–7.

[126] Vishik, I. M., Hashimoto, M., He, R.-H., Lee, W.-S., Schmitt, F., Lu, D., Moore, R. G., Zhang, C., Meevasana, W., Sasagawa, T., Uchida, S., Fujita, K., Ishida, S., Ishikado, M., Yoshida, Y., Eisaki, H., Hussain, Z., Devereaux, T. P., & Shen, Z.-X. (2012b). Phase competition in trisected superconducting dome. *Proceedings of the National Academy of Sciences*, 109(45), 18332–18337.

[127] Vishik, I. M., Moritz, B., Nowadnick, E. A., Lee, W. S., Tanaka, K., Sasagawa, T., Fujii, T., Devereaux, T. P., & Shen, Z. X. (2009). A momentum-dependent perspective on quasiparticle interference in $Bi_2Sr_2CaCu_2O_{8+delta}$. *Nature Physics*, 5(10), 718–721.

[128] Wise, W. D., Boyer, M. C., Chatterjee, K., Kondo, T., Takeuchi, T., Ikuta, H., Wang, Y., & Hudson, E. W. (2008a). Charge density wave origin of cuprate checkerboard visualized by scanning tunneling microscopy. 4(September), 5.

[129] Wise, W. D., Boyer, M. C., Chatterjee, K., Kondo, T., Takeuchi, T., Ikuta, H., Wang, Y., & Hudson, E. W. (2008b). Charge-density-wave origin of cuprate checkerboard visualized by scanning tunnelling microscopy. *Nature Physics*, 4(9), 696–699.

[130] Wölfle, P., Dubi, Y., & Balatsky, A. V. (2010). Tunneling into clean heavy fermion compounds: Origin of the Fano line shape. *Physical Review Letters*, 105(24), 246401.

[131] Wolgast, S., Kurdak, c., Sun, K., Allen, J. W., Kim, D.-J., & Fisk, Z. (2013). Low-temperature surface conduction in the Kondo insulator SmB_6. *Physical Review B*, 88, 180405.

[132] Wu, T., Mayaffre, H., Krämer, S., Horvatić, M., Berthier, C., Hardy, W., Liang, R., Bonn, D., & Julien, M.-H. (2015). Incipient charge order observed by NMR in the normal state of YBa2Cu3Oy. *Nature Communications*, 6(96), 6438.

[133] Xia, J., Schemm, E., Deutscher, G., Kivelson, S. a., Bonn, D. a., Hardy, W. N., Liang, R., Siemons, W., Koster, G., Fejer, M. M., & Kapitulnik, a. (2008). Polar Kerr-Effect Measurements of the High-Temperature $YBa_2Cu_3O_{6+x}$ Superconductor: Evidence for Broken Symmetry near the Pseudogap Temperature. *Physical Review Letters*, 100(12), 3–6.

[134] Xu, N., Shi, X., Biswas, P. K., Matt, C. E., Dhaka, R. S., Huang, Y., Plumb, N. C., Radović, M., Dil, J. H., Pomjakushina, E., Conder, K., Amato, A., Salman, Z., Paul, D. M., Mesot, J., Ding, H., & Shi, M. (2013). Surface and bulk electronic structure of the strongly correlated system SmB_6 and implications for a topological Kondo insulator. *Physical Review B*, 88, 121102.

[135] Yang, H.-B., Rameau, J. D., Pan, Z.-H., Gu, G. D., Johnson, P. D., Claus, H., Hinks, D. G., & Kidd, T. E. (2011). Reconstructed Fermi Surface of Underdoped $Bi_2Sr_2CaCu_2O_{8+delta}$ Cuprate Superconductors. *Physical review letters*, 107(4), 047003.

[136] Yang, K.-y., Rice, T. M., & Zhang, F.-c. (2006). Phenomenological theory of the pseudogap state. *Physical Review B*, 73(17), 174501.

[137] Yang, Y.-f. (2009). Fano effect in the point contact spectroscopy of heavy-electron materials. *Physical Review B*, 79(24), 241107.

[138] Yu, R., Weng, H., Hu, X., Fang, Z., & Dai, X. (2015). Model hamiltonian for topological kondo insulator smb 6. *New Journal of Physics*, 17(2), 023012.

[139] Zeljkovic, I., Main, E. J., Williams, T. L., Boyer, M. C., Chatterjee, K., Wise, W. D., Yin, Y., Zech, M., Pivonka, A., Kondo, T., Takeuchi, T., Ikuta, H., Wen, J., Xu, Z., Gu, G. D., Hudson, E. W., & Hoffman, J. E. (2012). Scanning tunnelling microscopy imaging of symmetry-breaking structural distortion in the bismuth-based cuprate superconductors. *Nature materials*, 11(7), 585–9.

[140] Zhang, X., Butch, N. P., Syers, P., Ziemak, S., Greene, R. L., & Paglione, J. (2013). Hybridization, inter-ion correlation, and surface states in the Kondo insulator SmB_6. *Physical Review X*, 3(1), 011011.

[141] Zheng, G.-q., Kuhns, P., Reyes, a., Liang, B., & Lin, C. (2005a). Critical Point and the Nature of the Pseudogap of Single-Layered Copper-Oxide $Bi_2Sr_{2-x}La_xCuO_{6+\delta}$ Superconductors. *Physical Review Letters*, 94(4), 047006.

[142] Zheng, G.-q., Kuhns, P. L., Reyes, A. P., Liang, B., & Lin, C. T. (2005b). Critical point and the nature of the pseudogap of single-layered copper-oxide $bi_2sr_2cacuo_{6+\delta}$ superconductors. *Phys. Rev. Lett.*, 94, 047006.

[143] Zhu, Z.-H., Nicolaou, A., Levy, G., Butch, N. P., Syers, P., Wang, X. F., Paglione, J., Sawatzky, G. A., Elfimov, I. S., & Damascelli, A. (2013). Polarity-driven surface metallicity in SmB_6. *Physical Review Letters*, 111, 216402.